DETECTION OF PROTEIN AND SMALL MOLECULE INTERACTIONS WITH LIPID MEMBRANES USING SECOND HARMONIC GENERATION AND ULTRAVIOLET-VISIBLE SUM-FREQUENCY GENERATION

by

Trang Thao Nguyen

A dissertation submitted to the faculty of
The University of Utah
in partial fulfillment of the requirements for the degree of

Doctor of Philosophy

Department of Chemistry

The University of Utah

December 2011

Copyright © Trang Thao Nguyen 2011

All Rights Reserved

The University of Utah Graduate School

STATEMENT OF DISSERTATION APPROVAL

The dissertation of **Trang Thao Nguyen**

has been approved by the following supervisory committee members:

John C. Conboy	, Chair	**07/08/2011** Date Approved
Joel M. Harris	, Member	**07/08/2011** Date Approved
Michael D. Morse	, Member	**07/08/2011** Date Approved
Michael H. Bartl	, Member	**07/08/2011** Date Approved
James N. Herron	, Member	**07/08/2011** Date Approved

and by **Henry S. White**, Chair of the Department of **Chemistry**

and by Charles A. Wight, Dean of The Graduate School.

ABSTRACT

This work describes the use of second harmonic generation (SHG) and ultraviolet-visible sum-frequency generation (UV-Vis SFG) to directly detect ligand-protein recognitions and drug-membrane associations. First, SHG spectroscopy was employed to detect protein-ligand binding for several model systems: avidin, streptavidin, neutrAvidin^{TM} and anti-biotin antibody binding to biotin. The equilibrium binding affinities of these model systems were measured and compared with those values reported in literature to validate the ability of SHG to detect protein-ligand interactions without any chemical modification. Furthermore, the energetics of the protein-ligand binding and the protein nonspecific adsorption were evaluated to provide useful information about these protein-ligand pairs which are commonly used in many bioanalytical applications.

Next, UV-Vis SFG spectroscopy was developed and utilized to detect drug-lipid membrane association for four drugs: ibuprofen, azithromycin, tetracaine, and tolnaftate. Drug association was measured on planar supported lipid bilayers composed of 1,2-dioleoyl-*sn*-glycero-3-phosphocholine. The drugs' equilibrium association constants were obtained and correlated with the drugs' partition coefficients in the membrane-water system. Furthermore, the drug surface excess in the lipid membrane was quantitatively determined using the combination of the UV-Vis SFG and the bulk partition coefficient.

It was shown that UV-Vis SFG is a powerful and novel technique to directly measure the association of drugs to a lipid membrane without chemical modification.

Finally, SHG imaging was employed in the label-free detection of the interactions between tetracaine and a multicomponent planar supported lipid bilayer array (MLBA). The MLBAs allowed the effects of lipid phase and cholesterol content on tetracaine binding to be examined simultaneously. Additionally, tetracaine binding at different charge states and the effect of the charged lipids were investigated. The maximum surface excess of tetracaine in the lipid bilayers was also determined. This demonstrates that SHG imaging is a sensitive technique which can directly image and quantitatively measure the association of tetracaine in a high-throughput manner.

This work has demonstrated that SHG and UV-Vis SFG are valuable alternatives in detection of biomolecular interactions at a lipid bilayer surface. The use of SHG or UV-Vis SFG imaging in combination with the MLBAs offer potential applications in high-throughput screenings of proteins and small molecules.

CONTENTS

LIST OF TABLES

ACKNOWLEDGEMENTS

I would like to acknowledge all those who have assisted and supported me during my graduate career at the University of Utah. Without their help and encouragement, this dissertation would not have been possible.

First, I would like to acknowledge Prof. John Conboy for his valuable guidance on my research project, willingness to help when needed, and his enthusiasm for research which truly motivated me. I appreciate the freedom provided by Prof. Conboy allowing me to try new ideas and troubleshoot the instruments in the lab which greatly supplemented my understanding.

I would also like to express my appreciation to my advisory committee members, Profs. Harris, Morse, Bartl and Herron, for their valuable critiques and reviews of my research.

I am grateful to all my colleagues for their help, support and friendship. In particular, Krystal Brown deserves my thanks for her suggestions and for proof-reading my manuscripts and dissertation. I am thankful to Krystal Sly, who teamed up with me on the protein project. We went through difficulties, frustration and finally excitement when the project had finished. Krystal Sly, thank you for your great effort, for taking the night shift for months and for being a good friend. I thank Kathryn Smith for assisting me with the use of the microspotter and for interesting discussions about the lipid microarray. My

thanks also go to Drs. Jin Liu and Julie Rollins for showing me everything I needed to know when I first started to work in the lab.

I would like to thank the professional staff in the Chemistry Department for their help, especially, Ms. Margaret Beebe, our group secretary, who has always been helpful and supportive.

Last but not least is my deepest appreciation to my big family for their love and support. Mom and Dad, I thank you for your love, encouragement and sacrifice to make sure that I have always had the best things in my life. I am proud to be your daughter. Thanks to my sister, Thao, for being supportive and a good listener. I must mention the support from my brothers, Thanh and Son. My thanks to my parents-in-law for loving me as their own daughter. Thanks to Hieu, my brother-in-law, for his kindness and watchfulness. Special thanks go to my husband, Lam, for always being there for me. His love, support and companionship has made my life's journey more joyful and interesting.

CHAPTER 1

INTRODUCTION

Biomolecular interactions are the basis of all activities in living systems. For example, complex signal pathways for hormones and neurotransmitters are regularly initiated by the interactions between G protein coupled receptors (GPCRs) and ligands;[1] immune responses are mediated by antibody-antigen interactions;[2,3] cell recognition and adhesion are related to protein-carbohydrate interactions;[4-7] and pharmacological activities are often induced by drug-protein/drug-cell membrane interactions.[8-10] The investigation and characterization of such biomolecular interactions would enhance our understanding of the mechanisms and functions of many biological activities. Consequently, there has been a significant effort to develop techniques which can more efficiently and accurately detect biomolecular interactions. Such detailed information would enable advancements in biosensing applications, such as more efficient medical diagnostic tools and pharmaceuticals. Biosensors are normally designed to detect a specific binding event between a ligand immobilized on a sensor surface and a biomolecule in solution. Development of these types of applications requires techniques capable of detecting biomolecular interactions at surfaces.

Currently, biomolecular interactions are most commonly investigated by fluorescence where the biomolecule of interest is detected via a fluorescent probe.[2,11-14] Surface specific total internal reflection fluorescence (TIRF) is an extremely sensitive

technique that can detect interactions at the molecular level.[15,16] However, the major drawback of fluorescence is that attaching a fluorescent probe can alter the native conformation and/or charge of the biomolecule and subsequently alter its binding properties.[17] Even when the biomolecule has intrinsic fluorescence, photobleaching or self-quenching of the fluorophore is common and would also alter the observed binding.[18,19] To circumvent these issues, label-free techniques such as surface plasmon resonance (SPR) and quartz crystal microbalance (QCM) have been utilized. SPR, an optical technique that quantifies the binding of biomolecules by detecting the corresponding change in mass, has been used to detect drug-liposome interactions[20,21] and ligand-protein interactions.[22-24] Similarly, QCM detects binding events through mass changes and has been used to detect proteins binding to a ligand immobilized on a sensor surface.[25-27] Although SPR and QCM offer the advantage of label-free detection, these mass based techniques lack the chemical sensitivity of spectroscopic methods and are therefore limited in their applications. Raman scattering incorporated with confocal microscopy, another label-free technique, has been used in detection of drug-liposome interactions.[28] The confocal microscopy allows Raman scattering from individual lipid vesicles to be detected, eliminating the contribution from the lipid matrix. As the Raman scattering signal is intrinsically weak, the technique requires a high laser power and long integration time.[29] Additionally, the Raman signal is often saturated by fluorescence from the samples.[29] Therefore, the limitation of these techniques makes it essential to develop surface specific and label-free methods which also possess high spectroscopic sensitivity.

Recently, the nonlinear optical spectroscopic techniques sum-frequency generation vibrational spectroscopy (SFVS) and second harmonic generation (SHG) have been used for biomolecular interactions at interfaces.[30-41] Specifically, SFVS has been used to investigate structure and orientation of membrane protein/peptide associated in lipid membrane,[30,34] and interactions between fibrinogen or blood coagulation factor and polymer surfaces.[32,42] SHG has been applied to monitor protein adsorption at a solid/liquid interface,[35,36] and peptide association to a lipid bilayer.[37,38] It has also been successfully applied to image biological tissue,[39] living cells,[40] protein crystals, and chiral molecules adsorbed to lipid bilayer arrays.[43] As coherent scattering processes that are independent of a direct electronic excitation or emission, SFG and SHG do not significantly suffer from photobleaching or phototoxicity as fluorescence does.[40] Furthermore, SFG and SHG possess the surface specificity, high sensitivity and spectroscopic selectivity (infrared for SFG and ultraviolet-visible for SHG) making them as attractive and powerful techniques to study biomolecular interactions.

In this dissertation, the study of biomolecular interactions at lipid bilayer surfaces by SHG and SFG is presented. The general principles of SHG are discussed in Chapter 2 with a focus on the counter-propagating geometry. Next, the application of SHG spectroscopy in detecting biomolecular interactions is presented in Chapter 3. In particular, protein-ligand interactions are investigated using avidin, streptavidin, neutrAvidin^{TM} and anti-biotin antibody binding to biotin ligand doped in a lipid bilayer. These protein-biotin complexes have been used as models for studying protein-ligand interactions which are normally investigated by fluorescence[16,44,45] or SPR.[24] The use of these particular protein-biotin models allow for a comparison between the results

obtained by SHG and previously published data to evaluate the utility of SHG as a method to study protein-ligand interactions. In addition to being used as the protein-ligand models, avidin, streptavidin, neutrAvidin™ and anti-biotin antibody-biotin complexes are often used as linkers to capture biomolecules in biosensing applications.[46-58] Despite the fact that these complexes are used interchangeably, very little work to date has compared the specific and nonspecific affinities of avidin, streptavidin, neutrAvidin™, and anti-biotin antibody to biotin at surfaces. The direct comparison presented in Chapter 3 offers new and useful information about the binding properties of complexes commonly used in a wide variety of bioanalytical applications.

To further demonstrate the ability of nonlinear optical spectroscopies in detection of biomolecular interactions, ultraviolet-visible (UV-Vis) SFG is implemented and used as an ultrasensitive technique in studying biomolecular interactions. In Chapter 4, the background of SFG is presented along with a discussion of UV-Vis SFG. UV-Vis SFG is able to probe electronic transitions in the deep UV region ($\pi \rightarrow \pi^*$ and $n \rightarrow \pi^*$ transitions). This enables the detection of a variety of biological species including aromatic amino acids, peptides, proteins and aromatic/double bond containing drugs. Since most drugs on the market target proteins embedded within cell membranes,[59] any interaction between the drug and lipids surrounding the targeted proteins may influence the drug's pharmacological activities.[60,61] This makes the detection of drug-lipid membrane interactions of great interest. Conventionally, drug-membrane interactions have been studied using the equilibrium of the drug between water and 1-octanol, a molecule which mimics the lipid membrane.[62-64] However, the thermodynamics of a lipid membrane, a roughly 50 Å thick bilayer composed of various phospholipids, proteins and

cholesterol, cannot be effectively characterized by the bulk thermodynamic properties of a homogenous liquid phase. While liposome based assays have been developed to more accurately model and study drug-membrane association,[65-68] the use of planar supported lipid bilayers (PSLBs) offers the advantage of no separation step required as compared to the liposome based assays. In order to effectively and accurately study drug-lipid membrane interactions, a method with both great sensitivity and surface specificity is required. This combination would allow the direct detection of analytes with such low molecular weights without any chemical modification at the interfacial level without interference from solution phase species. It is shown in Chapter 5 that the UV-Vis SFG spectroscopy can be used to detect drug-lipid membrane interactions. The association constants of four different drugs including ibuprofen, azithromycin, tetracaine and tolnaftate into a lipid bilayer were measured. Furthermore, the surface excess of each drug in the lipid bilayers was accessible using the UV-Vis SFG measurements in combination with the partition coefficients of the drugs. Knowledge of the surface excess of the drug in the membrane is crucial as it determines the bioavailability of the drug to its target protein. The work presented in Chapter 5 demonstrates the ability of UV-Vis SFG to be used as a new powerful technique in detection of small molecules (drugs) association into a lipid bilayer.

There has been a significant effort to develop high-throughput screening methods for rapid and efficient detection of biomolecular interactions. High-throughput screening using microarray based assays for DNA[69-71] and proteins[67,68] allow multiple binding events to be detected in a single assay. Such microarray assays have been successfully employed for the detection of DNA sequencing and antibody-antigen interactions. In

order to take advantage of the ability of microarray based assays to detect multiple binding events, in Chapter 6, a high-throughput detection method was developed to measure drug association into multicomponent lipid bilayer microarrays. The lipid bilayer microarray, created by a continuous flow microspotter, allowed the effects of lipid physical state and cholesterol content on the local anesthetic tetracaine binding to be examined simultaneously by second harmonic generation imaging. Additionally, the interactions between tetracaine and the lipid bilayer arrays at different charge states (protonated and neutral) of the drug and the effect of charged lipids were examined. The results illustrate that SHG imaging in combination with a lipid bilayer array has potential applications for high-throughput screening.

The problems associated with labeling a biomolecule with a fluorescent probe have been the major driving force for the development of label-free methods. Surface specific SPR and QCM have received great attention because as mass-based techniques they can detect biomolecular interactions without chemical modification; however, the lack of spectroscopic sensitivity limits their applications. The nonlinear optical spectroscopic techniques, SHG and UV-Vis SFG possess surface specificity, spectroscopic sensitivity and the ability to be coupled with a lipid microarray to enable the direct detection of biomolecular interactions, i.e., protein-ligand and small molecule-lipid membrane, in a high-throughput fashion. Furthermore, the SHG imaging provides a direct visualization of drug association into lipid membranes without chemical modification as required by the conventional fluorescence technique. The work presented in this dissertation demonstrates the potential use of SHG and UV-Vis SFG spectroscopy/imaging in protein and drug screening.

1.1 References

(1) Krall, J. A.; Beyer, E. M.; MacBeath, G. *PLoS One* **2011**, *6*, e15945.

(2) Pisarchick, M. L.; Thompson, N. L. *Biophys. J.* **1990**, *58*, 1235-1249.

(3) Thompson, N. L.; Poglitsch, C. L.; Timbs, M. M.; Pisarchick, M. L. *Acc. Chem. Res.* **1993**, *26*, 567-573.

(4) Varki, A. *Glycobiology* **1993**, *3*, 97-130.

(5) Karlsson, K. A. *Biochem. Soc. Trans.* **1999**, *27*, 471-474.

(6) Ofek, I.; Hasty, D. L.; Doyle, R. J. *Bacterial Adhension to Animal Cells and Tissues*; ASM Press: Washington DC, 2003.

(7) Taylor, M. E.; Drickamer, K. *Introduction to Glycobiology*; 2nd ed.; Oxford University Press: New York, 2006.

(8) Swinney David, C. *Nat. Rev. Drug Discovery* **2004**, *3*, 801-808.

(9) Mason, R. P. *Biochem. Pharmacol.* **1993**, *45*, 2173-2183.

(10) Bovill, J. G. *Pharmacol. Anaesthesiol.* **2005**, 1-18.

(11) Barghouthi, S.; Eftink, M. R. *Proc. SPIE-Int. Soc. Opt. Eng.* **1992**, *1640*, 632-636.

(12) Moran-Mirabal, J. M.; Edel, J. B.; Meyer, G. D.; Throckmorton, D.; Singh, A. K.; Craighead, H. G. *Biophys. J.* **2005**, *89*, 296-305.

(13) Yang, T.; Baryshnikova, O. K.; Mao, H.; Holden, M. A.; Cremer, P. S. *J. Am. Chem. Soc.* **2003**, *125*, 4779-4784.

(14) Shi, J.; Yang, T.; Kataoka, S.; Zhang, Y.; Diaz, A. J.; Cremer, P. S. *J. Am. Chem. Soc.* **2007**, *129*, 5954-5961.

(15) Osborne, M. A. *J. Phys. Chem. B* **2005**, *109*, 18153-18161.

(16) Wayment, J. R.; Harris, J. M. *Anal. Chem. (Washington, DC, U. S.)* **2009**, *81*, 336-342.

(17) Sun, Y. S.; Landry, J. P.; Fei, Y. Y.; Zhu, X. D.; Luo, J. T.; Wang, X. B.; Lam, K. S. *Langmuir* **2008**, *24*, 13399-13405.

(18) Lakowicz, J. R. *Principles of Fluorescence Spectroscopy*; 2nd ed.; Kluwer Academic/Plenum Plublishers: NY, 1999.

(19) Yu, X.; Xu, D.; Cheng, Q. *Proteomics* **2006**, *6*, 5493-5503.

(20) Nussio Matthew, R.; Sykes Matthew, J.; Miners John, O.; Shapter Joseph, G. *Chem. Med. Chem.* **2007**, *2*, 366-373.

(21) Abdiche, Y. N.; Myszka, D. G. *Anal. Biochem.* **2004**, *328*, 233-243.

(22) Kuziemko, G. M.; Stroh, M.; Stevens, R. C. *Biochemistry* **1996**, *35*, 6375-6384.

(23) Mann, D. A.; Kanai, M.; Maly, D. J.; Kiessling, L. L. *J. Am. Chem. Soc.* **1998**, *120*, 10575-10582.

(24) Tang, Y.; Mernaugh, R.; Zeng, X. *Anal. Chem.* **2006**, *78*, 1841-1848.

(25) Janshoff, A.; Steinem, C.; Sieber, M.; el Baya, A.; Schmidt, M. A.; Galla, H. J. *Eur. Biophys. J.* **1997**, *26*, 261-270.

(26) Patel, A. R.; Frank, C. W. *Langmuir* **2006**, *22*, 7587-7599.

(27) Wolny, P. M.; Spatz, J. P.; Richter, R. P. *Langmuir* **2010**, *26*, 1029-1034.

(28) Fox, C. B.; Harris, J. M. *J. Raman Spectrosc.* **2010**, *41*, 498-507.

(29) Pawley, J. B. *Handbook of Biological Confocal Microscopy*; 3rd ed.; Spinger Science + Business Media, LCC: New York, 2006.

(30) Ye, S.; Nguyen, K. T.; Chen, Z. *J. Phys. Chem. B* **2010**, *114*, 3334-3340.

(31) Wang, J.; Paszti, Z.; Clarke, M. L.; Chen, X.; Chen, Z. *J. Phys. Chem. B* **2007**, *111*, 6088-6095.

(32) Clarke, M. L.; Wang, J.; Chen, Z. *J. Phys. Chem. B* **2005**, *109*, 22027-22035.

(33) Jung, S.-Y.; Lim, S.-M.; Albertorio, F.; Kim, G.; Gurau, M. C.; Yang, R. D.; Holden, M. A.; Cremer, P. S. *J. Am. Chem. Soc.* **2003**, *125*, 12782-12786.

(34) Kim, G.; Gurau, M. C.; Lim, S.-M.; Cremer, P. S. *J. Phys. Chem. B* **2003**, *107*, 1403-1409.

(35) Salafsky, J. S.; Eisenthal, K. B. *J. Phys. Chem. B* **2000**, *104*, 7752-7755.

(36) Salafsky, J. S. *J. Chem. Phys.* **2006**, *125*, 074701/074701-074701/074707.

(37) Conboy, J. C.; Kriech, M. A. *Anal. Chim. Acta* **2003**, *496*, 143-153.

(38) Kriech, M. A.; Conboy, J. C. *J. Am. Chem. Soc.* **2003**, *125*, 1148-1149.

(39) Chen, W.-L.; Li, T.-H.; Su, P.-J.; Chou, C.-K.; Fwu, P. T.; Lin, S.-J.; Kim, D.; So, P. T. C.; Dong, C.-Y. *Appl. Phys. Lett.* **2009**, *94*, 183902/183901-183902/183903.

(40) Campagnola, P. J.; Clark, H. A.; Mohler, W. A.; Lewis, A.; Loew, L. M. *J. Biomed. Opt.* **2001**, *6*, 277-286.

(41) Wampler, R. D.; Kissick, D. J.; Dehen, C. J.; Gualtieri, E. J.; Grey, J. L.; Wang, H.-F.; Thompson, D. H.; Cheng, J.-X.; Simpson, G. J. *J. Am. Chem. Soc.* **2008**, *130*, 14076-14077.

(42) Chen, X.; Wang, J.; Paszti, Z.; Wang, F.; Schrauben, J. N.; Tarabara, V. V.; Schmaier, A. H.; Chen, Z. *Anal. Bioanal. Chem.* **2007**, *388*, 65-72.

(43) Kriech, M. A.; Conboy, J. C. *J. Am. Chem. Soc.* **2005**, *127*, 2834-2835.

(44) Zhao, S.; Reichert, W. M. *Langmuir* **1992**, *8*, 2785-2791.

(45) Zhao, S.; Walker, D. S.; Reichert, W. M. *Langmuir* **1993**, *9*, 3166-3173.

(46) Cooper, M. A. *Nat. Rev. Drug Dis.***2002**, *1*, 515-528.

(47) Zhavnerko, G. K.; Yi, S. J.; Chung, S. H.; Yuk, J. S.; Ha, K. S. *NATO Sci. Ser., II* **2004**, *152*, 95-108.

(48) Garifallou, G. Z.; Tsekenis, G.; Davis, F.; Higson, S. P. J.; Millner, P. A.; Pinacho, D. G.; Sanchez-Baeza, F.; Marco, M. P.; Gibson, T. D. *Anal. Lett.* **2007**, *40*, 1412-1422.

(49) Barton, A. C.; Davis, F.; Higson, S. P. J. *Anal. Chem.* **2008**, *80*, 9411-9416.

(50) Ladd, J.; Boozer, C.; Yu, Q.; Chen, S.; Homola, J.; Jiang, S. *Langmuir* **2004**, *20*, 8090-8095.

(51) Hall, W. P.; Ngatia, S. N.; Van Duyne, R. P. *J. Phys. Chem. C* **2011**, *115*, 1410-1414.

(52) Litos, I. K.; Ioannou, P. C.; Christopoulos, T. K.; Traeger-Synodinos, J.; Kanavakis, E. *Biosens. Bioelectron.* **2009**, *24*, 3135-3139.

(53) Bai, S.; Zhao, J.; Zhang, Y.; Huang, W.; Xu, S.; Chen, H.; Fan, L.-M.; Chen, Y.; Deng, X. W. *Appl. Microbiol. Biotechnol.* **2010**, *86*, 983-990.

(54) Esseghaier, C.; Helali, S.; Ben Fredj, H.; Tlili, A.; Abdelghani, A. *Sens. Actuators, B* **2008**, *B131*, 584-589.

(55) Sun, H.; Choy, T. S.; Zhu, D. R.; Yam, W. C.; Fung, Y. S. *Biosens. Bioelectron.* **2009**, *24*, 1405-1410.

(56) Xu, F.; Zhen, G.; Yu, F.; Kuennemann, E.; Textor, M.; Knoll, W. *J. Am. Chem. Soc.* **2005**, *127*, 13084-13085.

(57) Bashir, R.; Gomez, R.; Sarikaya, A.; Ladisch, M. R.; Sturgis, J.; Robinson, J. P. *Biotechnol. Bioeng.* **2001**, *73*, 324-328.

(58) Lazcka, O.; Del Campo, F. J.; Munoz, F. X. *Biosens. Bioelectron.* **2007**, *22*, 1205-1217.

(59) Overington, J. P. A.-L., B.; Hopkins, A. L., *Nature Rev. Drug Dis.* **2006**, *5*, 993-996.

(60) Seydel, J. K. *Methods and Principles in Medicinal Chemistry* **2002**, *15*, 217-289.

(61) Triggle, D. J. *Drug-Membrane Interactions. Analysis, Drug Distribution, Modeling. Methods and Principles in Medicinal Chemistry, Volume 15, by J. K. Seydel and M. Wiese* **2003**, *Vol.46*.

(62) Bouchard, G.; Galland, A.; Carrupt, P.-A.; Gulaboski, R.; Mirceski, V.; Scholz, F.; Girault, H. H. *Phys. Chem. Chem. Phys.* **2003**, *5*, 3748-3751.

(63) Avdeef, A. *J. Pharm. Sci.* **1993**, *82*, 183-190.

(64) Boudeville, P.; Bona, M.; Burgot, J.-L. *J. Pharm. Sci.* **1996**, *85*, 990-998.

(65) Liu, X. Y.; Yang, Q.; Kamo, N.; Miyake, J. *J. Chromatogr., A* **2001**, *913*, 123-131.

(66) Pauletti, G. M.; Wunderli-Allenspach, H. *Eur. J. Pharm. Sci.* **1994**, *1*, 273-282.

(67) Choi, Y. W.; Rogers, J. A. *Pharm. Res.* **1990**, *7*, 508-512.

(68) Vazquez, J. L.; Montero, M. T.; Trias, J.; Hernandez-Borrell, J. *Int. J. Pharm.* **1998**, *171*, 75-86.

(69) Shumaker-Parry, J. S.; Aebersold, R.; Campbell, C. T. *Anal. Chem.* **2004**, *76*, 2071-2082.

(70) Shumaker-Parry, J. S.; Zareie, M. H.; Aebersold, R.; Campbell, C. T. *Anal. Chem.* **2004**, *76*, 918-929.

(71) Hassibi, A.; Vikalo, H.; Riechmann, J. L.; Hassibi, B. *Nucleic Acids Res.* **2009**, *37*, e132/131-e132/112.

CHAPTER 2

GENERAL PRINCIPLES OF SECOND HARMONIC GENERATION

Second harmonic generation (SHG) is a coherent second-order nonlinear optical process in which two photons at the same frequency ω are combined to generate a third photon at the frequency twice of the input frequency, 2ω. The process is only allowed in a noncentrosymmetric medium or at the interface between two centrosymmetric media. As the theory of second harmonic generation (SHG) have been previously described in depth,[1,2] only the general principles of SHG will be presented in this chapter with a focus on the counter-propagating geometry which will be employed in the studies presented in Chapter 3 and 6.

2.1 General Principles of SHG

SHG is the nonlinear conversion of two photons of frequency ω to a new photon of frequency 2ω. The SHG process is governed by an induced nonlinear polarization at 2ω, $P(2\omega)$, generated when the input photons, ω, spatially and temporally overlap at a surface. $P(2\omega)$, is given as:

$$P(2\omega) = \chi^{(2)}_{ijk} E_j(\omega) E_k(\omega) \,, \tag{2.1}$$

where $\chi^{(2)}_{ijk}$ is a third rank tensor which describes the macroscopic response of the system to the applied electric fields $E_j(\omega)$ and $E_k(\omega)$. The indices represent the output SHG (i)

and input fields (j,k) which can assume any of the three Cartesian coordinates (x,y,z). As a result, $\chi^{(2)}_{ijk}$ is composed of 27 elements, but it is reduced to 18 elements since $E_j(\omega)$ and $E_k(\omega)$ are interchangeable. The induced polarization $P(2\omega)$ can be mathematically expressed as:

$$\begin{bmatrix} P_x(2\omega) \\ P_y(2\omega) \\ P_z(2\omega) \end{bmatrix} = \begin{bmatrix} \chi_{xxx} & \chi_{xyy} & \chi_{xzz} & \chi_{xxz} & \chi_{xxy} & \chi_{xyz} \\ \chi_{yxx} & \chi_{yyy} & \chi_{yzz} & \chi_{yxz} & \chi_{yxy} & \chi_{yyz} \\ \chi_{zxx} & \chi_{zyy} & \chi_{zzz} & \chi_{zxz} & \chi_{zxy} & \chi_{zyz} \end{bmatrix} \times \begin{bmatrix} E_x(\omega)\ E_x(\omega) \\ E_y(\omega)\ E_y(\omega) \\ E_z(\omega)\ E_z(\omega) \\ 2E_x(\omega)\ E_z(\omega) \\ 2E_x(\omega)\ E_y(\omega) \\ 2E_y(\omega)\ E_z(\omega) \end{bmatrix}. \quad (2.2)$$

The second-order susceptibility, $\chi^{(2)}_{ijk}$, is dependent on the symmetry of the system. Specifically, in the presence of inversion symmetry, i.e., bulk solution or isotropic media, the susceptibility tensor $\chi^{(2)}_{ijk}$ vanishes under the electric-dipole approximation, and thus the SHG process is disallowed. However, inversion symmetry is broken at the interface between two isotropic media. The interface between the two isotropic media possesses $C_{\infty v}$ symmetry as it is symmetric about the surface normal. This results in three nonzero independent $\chi^{(2)}_{ijk}$ tensor elements, χ_{zzz}, χ_{zii} and χ_{izi} (i = x or y). The symmetry of the surface further reduces to C_{∞} when a chiral molecule present at the surface which gives rise for an additional nonzero $\chi^{(2)}_{ijk}$ tensor element, χ_{xyz}. These symmetry constraints on the susceptibility tensor make SHG a surface specific technique.

Taking into account the non-vanishing tensor elements, the components of the induced polarization in the Cartesian coordinate system (x,y,z) of the achiral surface can be written as:

$$P_x(2\omega) = \chi_{xzx} E_{x_1}(\omega) E_{z_2}(\omega) + \chi_{xzx} E_{z_1}(\omega) E_{x_2}(\omega) \,, \tag{2.3a}$$

$$P_y(2\omega) = \chi_{xzx} E_{y_1}(\omega) E_{z_2}(\omega) + \chi_{xzx} E_{z_1}(\omega) E_{y_2}(\omega) \,, \tag{2.3b}$$

$$P_z(2\omega) = \chi_{zxx} \left[E_{x_1}(\omega) E_{x_2}(\omega) + E_{y_1}(\omega) E_{y_2}(\omega) \right] + \chi_{zzz} E_{z_1}(\omega) E_{z_1}(\omega) \,, \tag{2.3c}$$

where E_x, E_y and E_z are the applied electric field vectors in the Cartesian coordinate system (x,y,z) for each of the input beams (1 and 2). These electric field vectors in the Cartesian coordinate system can be converted to the interfacial coordinate system, shown in Figure 2.1, through the following transformations:

$$E_x(\omega) = E f_x \cos(\theta) \cos(\gamma) \,, \tag{2.4a}$$

$$E_y(\omega) = E f_y \sin(\gamma) \,, \tag{2.4b}$$

$$E_z(\omega) = E f_z \sin(\theta) \cos(\gamma) \,, \tag{2.4c}$$

where E is the amplitude of the applied electric field, which is equal to the square-root of the intensity of the input beam I, f is the transmitted linear Fresnel coefficient as the transmitted electric field components propagate through the interface. θ is the incident angle with respect to the surface normal and γ is the polarization angle relative to the plane of the incidence. The polarization angle of the input beam is defined as γ = 0° or 180° is *p*-polarized, γ = 90° is *s*-polarized and γ = 45° is *mixed*-polarized. The interfacial

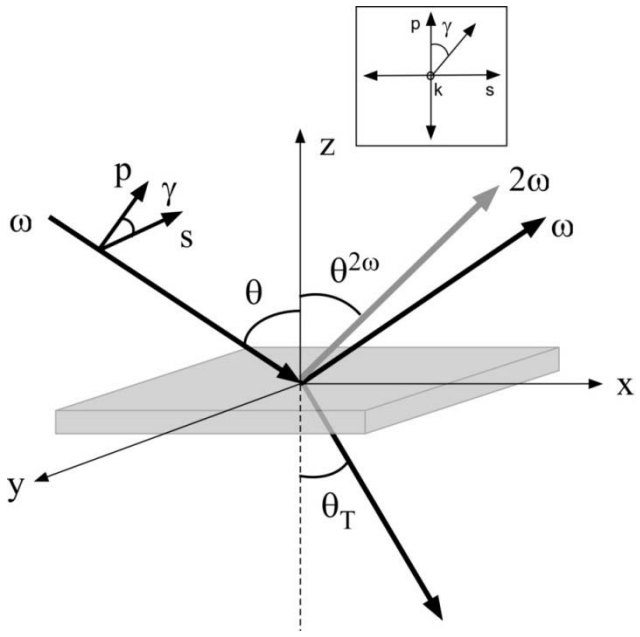

Figure 2.1 Schematic of the Cartesian and interfacial coordinate systems. The plane of incidence is the *xz* plane and the surface normal lies along the *z*-axis. θ is the angle of incidence relative to the surface normal and γ is the polarization with respect to the plane of incidence.

coordinate system is defined so that the plane of the incidence lies in the *xz* plane and the surface normal is along the *z*-axis as shown in Figure 2.1.

The expressions for the transmitted linear Fresnel coefficients *f* in the interfacial coordinate system are:

$$f_x(\omega) = \frac{2\cos\theta_I^{\omega}\sin\theta_T^{\omega}\cos\theta_T^{\omega}}{\sin(\theta_I^{\omega} + \theta_T^{\omega})\cos(\theta_I^{\omega} - \theta_T^{\omega})} \ , \tag{2.5a}$$

$$f_y(\omega) = \frac{2\cos\theta_I^{\omega}\sin\theta_T^{\omega}}{\sin(\theta_I^{\omega} + \theta_T^{\omega})} \ , \tag{2.5b}$$

$$f_z(\omega) = \frac{2\cos\theta_I^{\omega}(\sin\theta_T^{\omega})^2}{\sin(\theta_I^{\omega} + \theta_T^{\omega})\cos(\theta_I^{\omega} - \theta_T^{\omega})} \ , \tag{2.5c}$$

where θ_I is the incident angle of the fundamental beam and θ_T is the angle of the transmitted beam (Figure 2.1).

For a co-propagating geometry where the two incident beams originate from the same direction, the induced polarization can then be rewritten as:

$$P_x(2\omega) = 2\sqrt{I}\sin\theta\cos\theta\cos^2\gamma f_x f_z \chi_{xzx} \ , \tag{2.6a}$$

$$P_y(2\omega) = 2\sqrt{I}\sin\theta\sin\gamma\cos\gamma f_y f_z \chi_{xzx} \ , \tag{2.6b}$$

$$P_z(2\omega) = \sqrt{I}\left[(\cos^2\theta\cos^2\gamma f_x f_x + \sin^2\gamma f_y f_y)\chi_{zxx} + \sin^2\theta\cos^2\gamma f_z f_z \chi_{zzz}\right] . \tag{2.6c}$$

The SHG intensities polarized parallel (*p*) and perpendicular (*s*) to the plane of incidence can be expressed in terms of the induced polarization and a nonlinear Fresnel coefficient $\tilde{f}$ as shown below:

$$I_p = \left|\tilde{f}_x P_x(2\omega) + \tilde{f}_z P_z(2\omega)\right|^2 , \tag{2.7a}$$

$$I_s = \left|\tilde{f}_y P_y(2\omega)\right|^2 . \tag{2.7b}$$

The nonlinear Fresnel coefficient $\tilde{f}$ describes the refraction of the SFG output beam associated with the induced polarization $P(\omega_3)$ into the reflection and transmission media.[2] The expressions for $\tilde{f}$ derived by Bloembergen and Pershan[2] and modified by Dick *et al*.[3] for a nonlinear wave propagating in a thin nonlinear material between two linear media, are given by:

$$\tilde{f}_x^{\,R} = \frac{-8\,\pi\, d\,\omega\, \sin\theta_T^{2\omega}\cos\theta_T^{2\omega}}{c\, n_R^{2\omega}\, \sin(\theta_R^{2\omega} + \theta_T^{2\omega})\, \cos(\theta_T^{2\omega} - \theta_R^{2\omega})} , \tag{2.8a}$$

$$\tilde{f}_y^{\,R} = \frac{8\,\pi\, d\,\omega\, \sin\theta_T^{2\omega}}{c\, n_R^{2\omega}\, \sin(\theta_R^{2\omega} + \theta_T^{2\omega})} , \tag{2.8b}$$

$$\tilde{f}_z^{\,R} = \left(\frac{n_T^{2\omega}}{n_M^{2\omega}}\right)^2 \frac{8\,\pi\, d\,\omega\, (\sin\theta_T^{2\omega})^2}{c\, n_R^{2\omega}\, \sin(\theta_R^{2\omega} + \theta_T^{2\omega})\, \cos(\theta_T^{2\omega} - \theta_R^{2\omega})} , \tag{2.8c}$$

$$\tilde{f}_x^{\,T} = \frac{8\,\pi\, d\,\omega\, \sin\theta_T^{2\omega}\cos\theta_T^{2\omega}}{c\, n_R^{2\omega}\sin(\theta_R^{2\omega} + \theta_T^{2\omega})\, \cos(\theta_T^{2\omega} - \theta_R^{2\omega})} , \tag{2.9a}$$

$$\tilde{f}_y^{\,T} = \frac{8\,\pi\, d\,\omega\, \sin\theta_T^{2\omega}}{c\, n_R^{2\omega}\, \sin(\theta_R^{2\omega} + \theta_T^{2\omega})} , \tag{2.9b}$$

$$\tilde{f}_z^{\,T} = \left(\frac{n_R^{2\omega}}{n_M^{2\omega}}\right)^2 \frac{8\,\pi\, d\,\omega\, \sin\theta_T^{2\omega}\, \sin\theta_R^{2\omega}}{c\, n_R^{2\omega}\, \sin(\theta_R^{2\omega} + \theta_T^{2\omega})\, \cos(\theta_T^{2\omega} - \theta_R^{2\omega})} , \tag{2.9c}$$

where $\tilde{f}^{\,R}$ and $\tilde{f}^{\,T}$ are the reflected and transmitted nonlinear Fresnel coefficients, respectively, d is the thickness of the nonlinear medium, and c is the speed of light. $\theta_R^{2\omega}$

and $\theta_T^{2\omega}$ are the reflected and transmitted angles of the sum frequency beam, respectively. $n_R^{2\omega}$ and $n_T^{2\omega}$ are the refractive indices for the SHG beam in the reflected and transmitted media, and $n_M^{2\omega}$ is the refractive index of the SHG in the nonlinear medium. The presence of n_M in the nonlinear Fresnel coefficient $\tilde{f}_z$, which is a multiplicative factor of $P_z(2\omega)$ in the expression for I_p (equation 2.7a), can be eliminated by introducing an effective $\chi^{(2)}$ (χ^{eff}) as described by Dick *et al.*[3] The corresponding tensor elements χ_{zzz} and χ_{zxx} appeared in $P_z(\omega_3)$ can then be expressed in terms of χ^{eff} according to:

$$\chi_{zzz}^{eff} = \frac{d\,\chi_{zzz}}{(n_M^{\omega_3})^2}; \text{ and } \chi_{zxx}^{eff} = \frac{d\,\chi_{zxx}}{(n_M^{\omega_3})^2} \quad . \tag{2.10}$$

It should be noted that because n_M is not present in $\tilde{f}_x$ and $\tilde{f}_y$, the corresponding χ_{xzx} element can simply be rewritten as:

$$\chi_{xzx}^{eff} = d\,\chi_{xzx} \, . \tag{2.11}$$

The expressions for the nonlinear Fresnel coefficient $\tilde{f}$ in equations 2.8a-c and 2.9a-c no longer contain the refractive index, n_M, and thickness, d, of the nonlinear medium as these two parameters are accounted for in the effective χ^{eff}.

It has been shown previously by Kriech and Conboy that a counter-propagating geometry where the two incident beams originate from opposite directions (Figure 2.2) results in SHG emission along the surface normal, or the z-axis.[20] Relative to the conventional co-propagating geometry where both input beams approach from the same direction (Figure 2.1), counter-propagating geometry allows for a significant separation between the SHG and input beams, making SHG detection much easier.[20] In the counter-

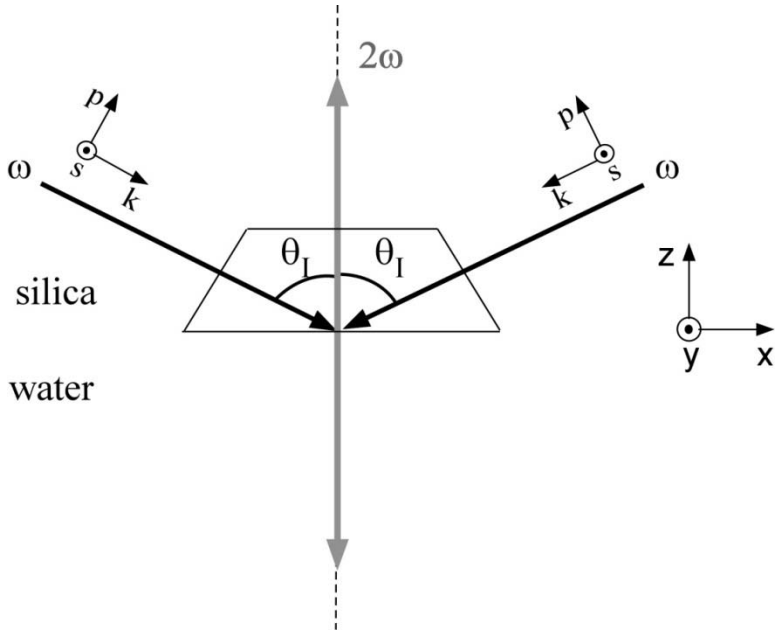

Figure 2.2 Schematic of a counter-propagating SHG. Two fundamental beams at the same frequency ω approach the silica/water interface from opposite directions with the incident angle θ_I. The second harmonic beam is generated at 2ω along the surface normal (z-axis).

propagating geometry, the incident beam approaches the surface under total internal reflection and the reflected beam is steered back upon itself. This results in the two identical beams arriving at the surface from opposite directions. The *x* component of the electric field vector of the second input beam has the opposite sign of the first input beam while the *y* and *z* components are unchanged. Therefore, the induced nonlinear polarization in *x* direction, $P_x(2\omega)$, becomes zero as $E_{x_1}(\omega) = - E_{x_2}(\omega)$ (see equation 2.3a). Additionally, the induced nonlinear polarization $P_z(2\omega)$ in the *z* direction vanishes since the SHG output is emitted along the *z*-axis. The induced polarization $P(2\omega)$ now only has one nonzero component propagating in *y* direction, which is given by:

$$P_y(2\omega) = I \sin\theta_I \sin\gamma \cos\gamma f_y f_z \chi_{xzx} K \ , \tag{2.12}$$

where *K* is the correction for differences of the linear Fresnel coefficients for *s*- and *p*-polarized inputs (f_s^r and f_p^r) upon reflection as described by Kriech and Conboy:[20]

$$K = f_s^r - f_p^r \ . \tag{2.13}$$

The expressions for the linear Fresnel coefficients f_s^r and f_p^r are given as:

$$f_s^r = \frac{\cos\theta_I - \sqrt{(n_T/n_R)^2 - \sin^2\theta_I}}{\cos\theta_I + \sqrt{(n_T/n_R)^2 - \sin^2\theta_I}} \ , \tag{2.14a}$$

$$f_p^r = \frac{-(n_T/n_R)^2 \cos\theta_I + \sqrt{(n_T/n_R)^2 - \sin^2\theta_I}}{(n_T/n_R)^2 \cos\theta_I + \sqrt{(n_T/n_R)^2 - \sin^2\theta_I}} \ . \tag{2.14b}$$

The SHG intensity in *y*-polarization is expressed as:

$$I_y(2\omega) = \left| P_y(2\omega)\tilde{f}_y \right|^2 , \tag{2.15}$$

where the nonlinear Fresnel coefficient $\tilde{f}_y$ is determined using equation 2.8b for reflection or equation 2.9b for transmission. For the counter-propagating geometry used here, $\tilde{f}_y$ is reduced to:

$$\tilde{f}_y^{\,R} = \tilde{f}_y^{\,T} = \frac{8\,\pi\,\omega}{c\,n_R^{2\omega}} . \tag{2.16}$$

Substitution of equation 2.12 for the $P_y(2\omega)$ and equation 2.16 for the $\tilde{f}_y$ into equation 2.15, the reflected and transmitted SHG intensity in *y* polarization can be rewritten as:

$$I_y^R(2\omega) = I_y^T(2\omega) = \frac{64\,\pi^2\,(\sin\theta_i)^2\,(\sin\gamma)^2\,(\cos\gamma)^2\,f_y^2\,f_z^2\,\chi_{xzx}^2\,K^2}{c^2\,(n_R^{2\omega})^2} . \tag{2.17}$$

As previously described, SHG is allowed at an interface between two isotropic media but prohibited in centrosymmetric bulk material due to the symmetry constraint of $\chi^{(2)}$. As a result, $\chi^{(2)}$, and subsequently the SHG intensity, are sensitive only to the molecules present at the interface making SHG a highly surface specific process. $\chi^{(2)}$ is comprised of two components: a nonresonant portion, $\chi_{NR}^{(2)}$ and a resonant portion, $\chi_R^{(2)}$:

$$\chi^{(2)} = \chi_{NR}^{(2)} + \chi_R^{(2)} . \tag{2.18}$$

The resonant portion $\chi_R^{(2)}$ can be given as:

$$\chi_R^{(2)} = N \sum_{a,b,c} \frac{\langle a|\mu_i|c\rangle\langle a|\mu_j|b\rangle\langle b|\mu_k|c\rangle}{(2\hbar\omega - E_{ca} - i\Gamma_{ca})(\hbar\omega - E_{ab} - i\Gamma_{ab})} , \tag{2.19}$$

where N is the surface density of molecules, h is Planck's constant, μ is the Cartesian coordinate dipole operator, Γ represents the linewidth of the transition, and *a, b* and *c* represent the initial, intermediate and final states, respectively (see Figure 2.3).[1]

Examination of equation 2.19 shows that the denominator will approach zero when the fundamental frequency, ω, or the SHG frequency, 2ω, approaches the frequency of an allowed dipole moment transitions at surfaces/interfaces. This causes an increase in the overall $\chi^{(2)}$ accompanied by an enhancement in the SFG intensity according to the relationship described in equations 2.17. This resonant enhancement in SHG has been utilized to investigate protein adsorption at a solid/liquid interface,[21,22] as well as peptide[23,24] and chiral molecule[20,23] association to a lipid bilayer.

2.2 Summary

In this chapter, the general principles of the nonlinear optical spectroscopy SHG were discussed. Due to the symmetry constraints, SHG is only allowed at surfaces or interfaces making the technique extremely surface sensitive. Additionally, the SHG intensity can be significantly enhanced when the fundamental or the nonlinear field's frequency is in resonance with electronic transitions of molecules presenting at surfaces/interfaces. This feature can be used as a sensitive and intrinsic probe to detect biomolecular interactions at a surface. The application of SHG in studying protein-ligand and drug-lipid membrane interactions will be presented in the following chapters.

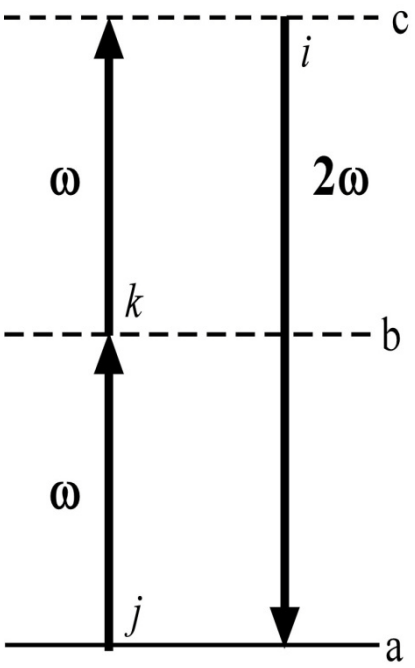

Figure 2.3 Energy level diagram of second harmonic generation process.

2.3 References

(1) Shen, Y. R. *The Principles of Nonlinear Optics*; Wiley: New York, 1984.

(2) Bloembergen, N.; Pershan, P. S. *Physical Review* **1962**, *128*, 606-622.

(3) Dick, B.; Gierulski, A.; Marowsky, G.; Reider, G. A. *Appl. Phys. B* **1985**, *B38*, 107-116.

(4) Salmeron, M.; Bluhm, H. *Surf. Rev. Lett.* **1999**, *6*, 1275-1281.

(5) Asanuma, H.; Noguchi, H.; Uosaki, K.; Yu, H.-Z. *J. Phys. Chem. C* **2009**, *113*, 21155-21161.

(6) Chen, X.; Allen, H. C. *J. Phys. Chem. B* **2010**, *114*, 14983-14988.

(7) Casford, M. T. L.; Davies, P. B.; Neivandt, D. J. *Langmuir* **2006**, *22*, 3105-3111.

(8) Hayes, P. L.; Keeley, A. R.; Geiger, F. M. *J. Phys. Chem. B* **2010**, *114*, 4495-4502.

(9) Conboy, J. C.; Messmer, M. C.; Richmond, G. L. *J. Phys. Chem. B* **1997**, *101*, 6724-6733.

(10) Conboy, J. C.; Messmer, M. C.; Richmond, G. L. *Langmuir* **1998**, *14*, 6722-6727.

(11) Chen, X.; Wang, J.; Sniadecki, J. J.; Even, M. A.; Chen, Z. *Langmuir* **2005**, *21*, 2662-2664.

(12) Wang, J.; Lee, S.-H.; Chen, Z. *J. Phys. Chem. B* **2008**, *112*, 2281-2290.

(13) Phillips, D. C.; York, R. L.; Mermut, O.; McCrea, K. R.; Ward, R. S.; Somorjai, G. A. *J. Phys. Chem. C* **2007**, *111*, 255-261.

(14) Fu, L.; Liu, J.; Yan, E. C. Y. *J. Am. Chem. Soc.* **2011**, ACS Just Accepted.

(15) Liu, J.; Conboy, J. C. *Langmuir* **2005**, *21*, 9091-9097.

(16) Kett, P. J. N.; Casford, M. T. L.; Davies, P. B. *Langmuir* **2010**, *26*, 9710-9719.

(17) Wang, T.; Li, D.; Lu, X.; Khmaladze, A.; Han, X.; Ye, S.; Yang, P.; Xue, G.; He, N.; Chen, Z. *J. Phys. Chem. C* **2011**, *115*, 7613-7620.

(18) Maeda, T.; Ishibashi, T.-A. *Appl. Spectrosc.* **2007**, *61*, 459-464.

(19) Hayashi, M.; Lin, S. H.; Raschke, M. B.; Shen, Y. R. *J. Phys. Chem. A* **2002**, *106*, 2271-2282.

(20) Kriech, M. A.; Conboy, J. C. *J. Opt. Soc. Am. B: Optical Physics* **2004**, *21*, 1013-1022.

(21) Salafsky, J. S.; Eisenthal, K. B. *J. Phys. Chem. B* **2000**, *104*, 7752-7755.

(22) Salafsky, J. S. *J. Chem. Phys.* **2006**, *125*, 074701/074701-074701/074707.

(23) Kriech, M. A.; Conboy, J. C. *J. Am. Chem. Soc.* **2005**, *127*, 2834-2835.

CHAPTER 3

INVESTIGATION OF BIOTIN BOUND PROTEIN-BIOTINYLATED LIPID INTERACTIONS WITH SECOND HARMONIC GENERATION

3.1 Introduction

As previously discussed in Chapter 2, the symmetry constraint in second harmonic generation (SHG) makes it a surface specific technique. The susceptibility tensor and subsequently the SHG intensity can be significantly increased when the fundamental or SHG frequency is in resonance with an electronic transition of a molecule of interest at a surface. This feature of SHG can be exploited as an intrinsic and sensitive probe to detect the presence of the molecule adsorbed at the surface. These characteristics make SHG an extremely attractive and sensitive technique for detecting biomolecular interactions at surfaces/interfaces. In this chapter, the application of SHG for studying protein binding to ligand immobilized at a lipid bilayer surface without using any extrinsic label is described.

Biotin bound protein complexes have been used in a wide variety of bioanalytical applications, including monitoring conformation changes in biomolecules,[1,2] fabrication of biochip sensors,[3-11] immunoassays,[12,13] and targeted drug delivery and screening.[14] In these applications, the protein-biotin complex is commonly used to tether biomolecules to a surface[1,2,15,16] or used as a linker to capture biomolecules[3-14,17] by taking advantage of the high affinity, specificity and stability of biotin bound proteins such as avidin,[10-12,16]

streptavidin,[1-3,13-15] neutravidin,[4-6] and anti-biotin antibody.[7-9] Avidin is a 66 kDa tetramer consisting of 4 identical subunits, each of which has one binding site for biotin. It has an extremely high binding affinity, $K_a \sim 10^{15}$ M^{-1} to free biotin in solution,[18] and forms a stable complex with biotin over a wide range of temperatures and pHs.[19] One major drawback to using avidin is the high degree of nonspecific adsorption caused by its basic isoelectric point (pI ~ 10).[19] At physiological pH, positively charged avidin can bind nonspecifically to negatively charged surfaces such as cell membranes[19] or silica substrates.[20] Another feature that contributes to avidin's high nonspecific adsorption is its carbohydrate groups which contain four mannose residues and three N-acetyl-glucosamine residues per subunit.[21] If the avidin-biotin complex is being used to capture a carbohydrate-binding molecule it can also bind specifically to the carbohydrate groups on avidin, limiting its use in bioassays. Both streptavidin and neutrAvidin, analogs of avidin, which also have a high affinity and specificity towards biotin[22,23] have been used as an alternative to avidin.[3-6] Streptavidin, which has a similar functional domain to avidin (~ 33% identical residues),[22] is a nonglycosylated protein expressed from Streptomyces avidinii bacteria with a slightly acidic pI of about 5-6.[19] NeutrAvidin™ is a commercially available deglycosylated form of avidin with a pI of 6.3.[24] The lower pIs and absence of the sugar groups in streptavidin and neutrAvidin™ are intended to lower the nonspecific binding relative to avidin without significantly affecting the affinity for biotin. As such streptavidin and neutrAvidin™ are commonly used in biosensing applications as an alternative to avidin as a way to reduce nonspecific binding to the sensor surfaces. Anti-biotin antibody, a 150 kDa immunoglobulin (IgG) protein that is generated by the immune cell in response to the antigen biotin, has also been used as an

alternative linker to capture biomolecules on biosensor surfaces.[7-9] Similar to streptavidin and neutrAvidin™, anti-biotin antibody has a high binding affinity for biotin (~ 10^8 M^{-1}).[25] Additionally, use of the anti-biotin antibody-biotin complex has been shown to increase biomolecular capture in biosensing applications as compared to the streptavidin-biotin complex.[7,9] Surprisingly, little work to date has compared the specific and nonspecific affinities of avidin, streptavidin, neutrAvidin™, and anti-biotin antibody to biotin at surfaces despite the use of these proteins in a broad range of biosensing applications. In this work, the binding affinities of these biotin-binding proteins to biotinylated lipid bilayers were measured as well as the energetics of the binding process and the nonspecific adsorption of all four proteins were specifically addressed.

Biosensing applications have employed the use of protein-biotin complexes to a various types of surfaces including functionalized gold surfaces,[3-5,13] polymer films,[12] glass,[1,26] silver nanoprisms,[7] as well as planar supported lipid bilayers (PSLBs) or liposomes.[15,27] Planar supported lipid bilayers were chosen as a platform for the protein binding assays in this study due to the ease of preparation as there is no need for chemical modification of the surface. Additionally, PSLBs allow the ligand density to be more precisely controlled,[28] providing better reproducibility for a comparison between experiments.

The binding affinity between protein-ligand pairs at surfaces is known to be affected by the surface density of the ligand.[29-31] Zhao and coworkers have shown that once the biotin density is high enough to bind a monolayer of avidin any additional biotin sterically hinders further avidin binding.[30] This study also showed that doubly bound avidin-biotin complex (two biotin molecules for every one avidin molecule) is more

stable than the singly bound complex.[30] This suggests that the optimal biotin density would be one that allows a monolayer of avidin to bind bivalently. In this study, the appropriate biotin density to form a doubly bound complex monolayer of the protein can be calculated using the area for avidin, 3025 $Å^2$ (55 Å × 55 Å),[19] and the areas for a lipid molecule and biotinylated lipid, 70 Å.[32] For a monolayer of avidin (3.31×10^{12} molecule/cm^2) to bivalently bind to biotin, the biotin density must be twice as large; therefore, the density of the biotinylated lipid in the lipid bilayer should be about 4.6 mol % [($2 \times 3.31 \times 10^{12}$ biotinylated lipid molecule/cm^2)/(1.43×10^{14} lipid molecule/cm^2) × 100%]. Previous studies that investigated biotin binding to neutrAvidin™ and streptavidin in PSLBs have also shown that protein binding increases with biotin density up to 4 mol % and then saturates.[33,34] At this biotin density, two biotin molecules effectively bind to every one protein to form a doubly protein-biotin complex monolayer on the lipid bilayer surface. When the biotin density is lower than 4 mol % (less than a monolayer coverage) fewer protein ligand complexes are formed but above 4 mol % steric hindrance from neighboring avidin molecules decreases binding. In order to provide useful information for bioanalytical applications, which aim to maximize the number of captured biomolecules, the optimal biotin density of 4 mol % (a monolayer coverage of bivalently bound protein) was used in the current study.

Several surface specific techniques have been utilized in studying protein-ligand interactions. Total internal reflection fluorescence (TIRF) is commonly used to detect protein-ligand interaction where the protein of interest is detected via a fluorescent probe.[23,29,35,36] Although fluorescence possesses an extremely high sensitivity, the technique however has its own disadvantages. The labeling of the protein with a foreign

fluorescent molecule can change the protein structure and/or charge and consequently alter its binding properties.[37] To circumvent these issues, label-free techniques such as surface plasmon resonance (SPR) and quartz crystal microbalance (QCM) have recently drawn great attention. SPR[38-40] and QCM[20,27,41] have been used to detect protein-ligand interactions by measuring the mass change upon the binding event. Despite the fact that SPR and QCM offer the advantage of label-free detection, these mass based techniques lack the chemical sensitivity of spectroscopic methods.

In this chapter, SHG was employed as a label-free alternate to investigate the interactions between biotin and the four biotin-bound proteins, avidin, streptavidin, neutrAvidin™ and anti-biotin antibody. SHG has also been previously used to monitor protein adsorption at a solid/liquid interface[42,43] and association of biomolecules to a lipid monolayer or bilayer.[44-48] SHG provides the surface selectivity and high sensitivity required to study protein-biotin interactions at an interface without the use of an external label.

3.2 Experimental

3.2.1 Materials

1,2-dioleoyl-*sn*-glycero-3-phosphocholine (DOPC) and 1,2-dioleoyl-*sn*-glycero-3-phosphoethanolamine-N-(Cap biotinyl) (sodium salt) (biotin-cap-DOPE) were obtained from Avanti Polar Lipids and used as received. NeutrAvidin™ was purchased from Pierce, avidin and streptavidin from Streptomyces avidinii, IgG from rabbit serum and anti-biotin antibody produced in goat were obtained from Sigma-Aldrich. All water used in the experiments was obtained from a Nanopure™ Infinity Ultrapure water system with a minimum resistivity of 18.2 MΩ-cm. Phosphate buffered saline (PBS) was made from

50 mM $Na_2HPO_4 \cdot 7H_20$ and 100 mM NaCl in water and adjusted to a pH of 7.4 using NaOH. The proteins were dissolved in PBS pH 7.4 to the desired working concentrations. The substrates used for the preparation of the PSLBs were custom manufactured full spectrum grade (IR/UV) fused silica prisms (Almaz Optics). The prisms were cleaned by immersion in a solution of 70% sulfuric acid and 30% hydrogen peroxide overnight. Prior to use, the prisms were rinsed thoroughly with water and cleaned with Ar plasma (Harrick Scientific Plasma Cleaner/Sterilizer, Ossining, NY) for 3 minutes.

3.2.2 Small Unilamellar Vesicle (SUV) Preparation

All lipids were dissolved in chloroform then evaporated under a gentle stream of $N_2(g)$ and vacuum dried over night to remove residual solvents. The SUV solutions were formed by resuspending the dried lipids in PBS to a concentration of 1 mg/mL by vortexing followed by bath sonication for 10 - 30 minutes until the solutions become clear.

The prism used as PSLB substrates was mounted in a custom built flowcell (volume of 0.4 mL). PSLBs were formed on the silica prism by vesicle fusion, which involved incubating the surface with the SUV solution for 20 minutes at room temperature. The flowcell was then flushed with PBS to remove any free lipid solution.

3.2.3 Ligand-Protein Binding Assay

PSLBs of DOPC containing 4 mol % biotin-cap-DOPE for avidin, neutrAvidin^{TM}, streptavidin and anti-biotin antibody binding were created on the prism surface by vesicle fusion as described above. To reduce nonspecific adsorption of the proteins, the PSLBs in these experiments were incubated in 1mg/mL monoclonal IgG from rabbit serum in PBS pH 7.4 for 30 minutes to block any defects that might exist on the lipid surfaces, except

for the anti-biotin antibody experiments. The PSLBs were then rinsed thoroughly with PBS to remove any free IgG remaining in solution.

Increasing concentrations of the protein solutions, from low to high, were injected into the flowcell. At each protein concentration, the SHG intensity was recorded at a 30-minute interval until a steady-state response was achieved. The SHG intensity collected with time allowed kinetic measurement to be determined. Generally, low concentrations of the proteins required up to 4 hours to reach equilibrium. During this period, fresh protein solution was injected every 30 minutes to account for the bulk depletion caused by surface adsorption of the proteins. It is important to note that protein dilutions were freshly prepared prior to each injection to further prevent the proteins from nonspecifically adsorbing to the vials and syringes. Thermodynamic measurements were made using the SHG intensity measured at equilibrium at each protein concentration.

3.2.4 SHG Measurements

Counter-propagating SHG was employed in this study. A collimated 532 nm laser beam (2^{nd} harmonic output of a Nd:YAG laser, Continuum, Surelite I, 10 Hz) with a mixed polarization state (equal amounts of *s* and *p* polarized components) was directed at the prism/water interface at an incident angle of 67° under total internal reflection. The incident laser beam with an intensity of 14 mJ/pulse and a diameter of 3 mm was used. The reflected beam was steered back to overlap spatially and temporally with the incident beam, generating SHG at 266 nm. A schematic representing the optical rearrangement is shown in Figure 3.1. Optical filters were used to remove any scattered visible light before the reflected SHG signal was collected by a solar blind photomultiplier tube.

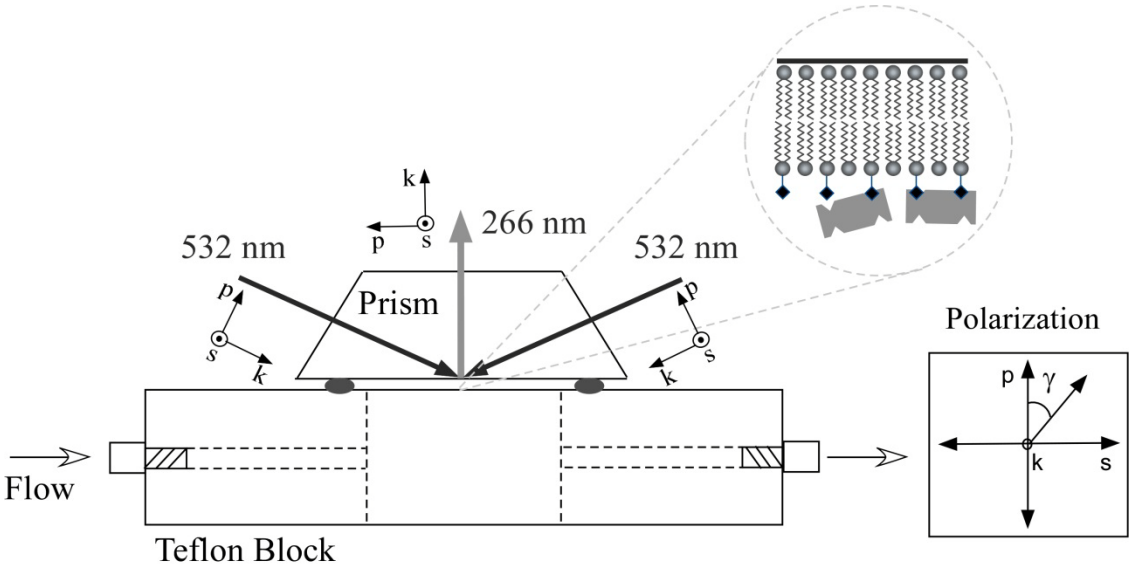

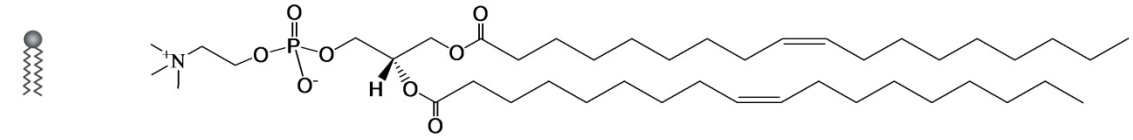

1,2 dioleoyl-*sn*-glycero-3-phosphocholine (DOPC)

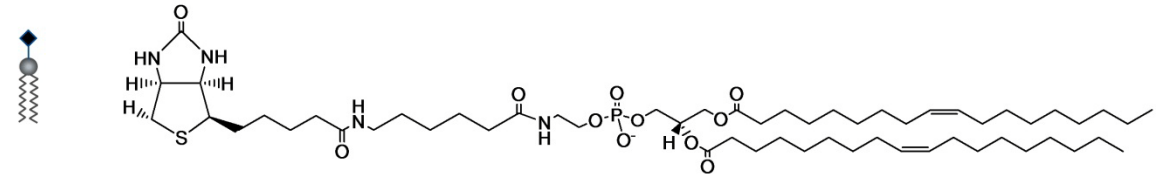

1,2 dioleoyl-*sn*-glycero-3-phosphoethanolamine-N-(Cap biotinyl)

Figure 3.1 SHG cell showing the geometric arrangement of the fundamental and SHG beams. Also shown are representation of the polarization state of the incident and output fields denoted as the angle γ with respect to the propagation direction (*k*) and the lipid structures used in the study.

As described in Chapter 2, the SHG intensity is proportional to the second-order susceptibility tensor, $\chi^{(2)}_{ijk}$ which has a nonresonant $\chi^{(2)}_{NR}$ and resonant $\chi^{(2)}_{R}$ contribution. An enhancement in $\chi^{(2)}_{R}$, and subsequently the SHG signal, will be observed when the incident, ω, or SHG, 2ω, frequency is resonant with an electronic transition of a molecule at the interface. As seen in the extinction coefficient spectra of the proteins in Figure 3.2, the SHG wavelength at 266 nm is in resonance with the $\pi \rightarrow \pi^*$ transitions of the tryptophan and tyrosine's aromatic rings of the proteins,[49] which results in the enhancement of the SHG signal when the protein is present at the lipid membrane surface. Although the electric-quadrupole response from the bulk medium can contribute to the overall SHG signal,[33,34] its contribution can be neglected if the SHG frequency is in resonance with the electric-dipole allowed transition of molecules residing at the interface.[50] As the SHG frequency used in this study is in resonant with the $\pi \rightarrow \pi^*$ transitions of the proteins adsorbed to the surface, the measured SHG intensity is predominantly dipolar in nature with little to no detectable contribution from the quadrupolar response expected.

In equation 2.33 in Chapter 2, the nonresonant susceptibility $\chi^{(2)}_{NR}$ can be assumed to be real due to lack of any electronic resonances from the lipids, water, or silica in the spectral region of interest while the resonant susceptibility $\chi^{(2)}_{R}$ is a complex number owing to the resonances with the electronic transitions in the proteins. For simplification, $\chi^{(2)}_{NR}$ and $\chi^{(2)}_{R}$ can be expressed as:

$$\chi^{(2)}_{NR} = A; \text{ and } \chi^{(2)}_{R} = B + iC. \tag{3.1}$$

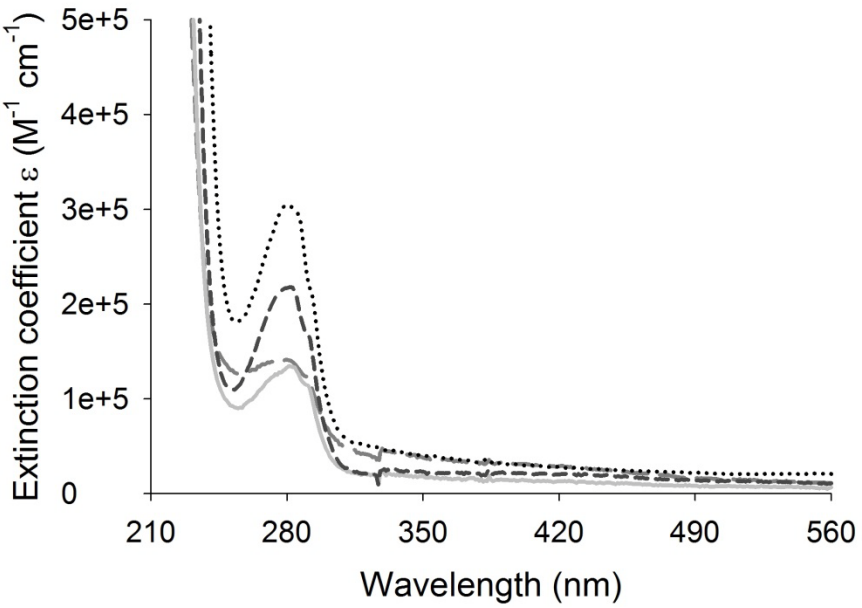

Figure 3.2 Extinction coefficient spectra of avidin (solid), neutrAvidin^{TM} (long dash), streptavidin (short dash), and anti-biotin antibody (dotted).

where A represents the nonresonant response from the background, and B and C denote the real and imaginary components of $\chi_R^{(2)}$, respectively. The SHG intensity in equation 2 can then be expressed as:

$$I_{SHG} \propto \left|\chi^{(2)}\right|^2 \propto |A + N(B + iC)|^2 \propto (A + NB)^2 + (NC)^2 \tag{3.2}$$

Assuming the surface adsorption of protein follows the Langmuir model, the surface density N in equation 3.2 is given by:

$$N = \frac{N_{max}K_o[P]}{1 + K_o[P]}, \tag{3.3}$$

where N_{max} is the maximum surface density at saturation, K_o is the equilibrium association constant and $[P]$ is the bulk protein concentration. Substitution of equation 3.3 into equation 3.2 gives:

$$\begin{aligned} I_{\mathrm{SHG}} &\propto \left|\chi^{(2)}\right|^2 \propto \left(A + B\frac{N_{max}K_o[P]}{1 + K_o[P]}\right)^2 + \left(C\frac{N_{max}K_o[P]}{1+\mathrm{K_o[P]}}\right)^2 \\ &\propto A^2 + 2AB\frac{N_{max}K_o[P]}{1 + K_o[P]} + \left(B^2 + C^2\right)\left(\frac{N_{max}K_o[P]}{1 + K_o[P]}\right)^2. \end{aligned} \tag{3.4}$$

The SHG intensity due to the nonresonant background in the absence of protein adsorption is given by:

$$I_{SHG}^{background} \propto A^2. \tag{3.5}$$

Subtracting the background contribution (3.5) from the measured SHG intensity (3.4) gives the SHG intensity rising solely from protein adsorption, which can be expressed as:

$$I_{SHG} - I_{SHG}^{background} \propto 2\sqrt{I_{SHG}^{background}}\, B\frac{\sqrt{I_{SHG}^{Max}}\,K_o[P]}{1+K_o[P]} + \left(B^2 + C^2\right)\left(\frac{\sqrt{I_{SHG}^{Max}}\,K_o[P]}{1+K_o[P]}\right)^2, \qquad (3.6)$$

where $\sqrt{I_{SHG}^{Max}}$ is the square-root of the maximum SHG intensity at surface saturation. $\sqrt{I_{SHG}^{background}} = A$ if it is assumed that the real nonresonant response (A) from the background is positive.

For avidin, a previous study has shown that protein-protein interaction can modulate the energetic of protein association to a biotinylated surface.[29] When interactions between proteins are involved, a cooperative binding model, previously described by Zhao *et al.*,[29] can be used to fit the adsorption data:

$$N = \frac{N_{max}\omega^{\left(N/N_{max}\right)}K_o[P]}{1+\omega^{\left(N/N_{max}\right)}K_o[P]}, \qquad (3.7)$$

where $\omega = \eta^4$ by assuming the distribution of the biotin-bound proteins follows a square lattice and η is the cooperativity coefficient which characterizes the protein-protein interactions between neighboring protein molecules on the surface.[29] K_o in this equation is the intrinsic binding affinity of the protein to the ligand barring any protein-protein interactions.[29] When $\eta > 1$, the binding of a protein to a ligand exhibits a positive cooperativity, demonstrating that the protein-protein interaction enhances the ligand-protein binding. When $\eta < 1$, the protein-protein interaction reduces the ligand-protein binding resulting in a negatively cooperative ligand - protein binding. The cooperativity model becomes the Langmuir model when $\eta = 1$.

The SHG intensity in terms of the cooperativity adsorption model is obtained by substituting equation 3.7 into equation 3.2:

$$I_{SHG} - I_{SHG}^{background} \propto$$

$$2B\sqrt{I_{SHG}^{background}}\frac{\sqrt{I_{SHG}^{Max}}\,\omega\left(\sqrt{I_{SHG}}\Big/\sqrt{I_{SHG}^{Max}}\right)K_o[P]}{1+\omega\left(\sqrt{I_{SHG}}\Big/\sqrt{I_{SHG}^{Max}}\right)K_o[\mathrm{P}]}+\left(B^2+C^2\right)\left(\frac{N_{max}\,\omega\left(\sqrt{I_{SHG}}\Big/\sqrt{I_{SHG}^{Max}}\right)K_o[P]}{1+\omega\left(\sqrt{I_{SHG}}\Big/\sqrt{I_{SHG}^{Max}}\right)K_o[P]}\right)^2. \qquad (3.8)$$

3.2.5 Data Normalization

To allow a direct comparison of the SHG response from the specific and nonspecific binding of the proteins, the SHG intensities were normalized with respect to each other. The normalization was performed by measuring the SHG response from 10 mM KOH solution which was injected into the flowcell after each experiment. The measured SHG intensities from the KOH solution were then used to normalize the SHG intensities from the specific and nonspecific protein binding experiments. The KOH solution was used as a reference point as it provides a constant solution composition and pH by which the SHG intensity can be normalized, allowing the comparison between the SHG intensities from the specific and nonspecific binding of the proteins to be made.

3.3 Results and Discussion

3.3.1 Binding of Avidin, Streptavidin and NeutrAvidin™ to a Biotinylated DOPC Bilayer

The binding isotherms for avidin, neutrAvidin™ and streptavidin are shown in Figures 3.3, 3.4 and 3.5, respectively. The SHG intensities increase with increasing

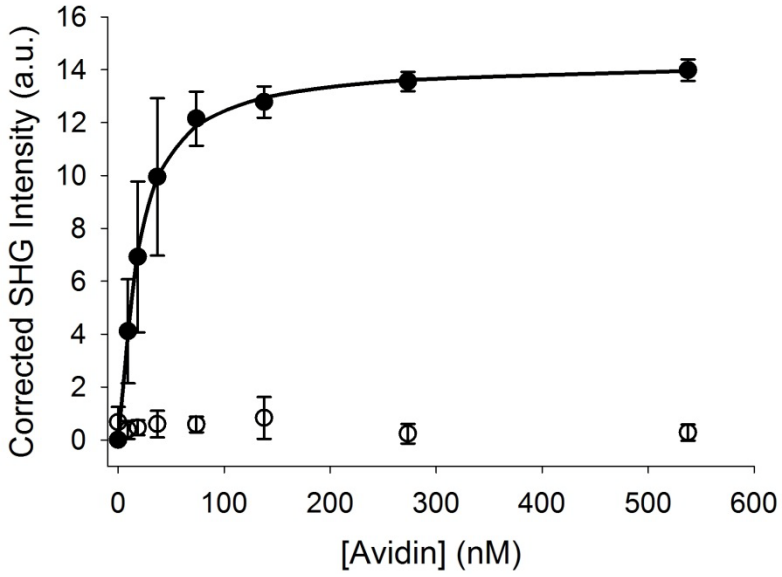

Figure 3.3 Corrected SHG intensity vs. bulk protein concentration for avidin binding to DOPC bilayers containing 4 mol % biotin-cap-DOPE (filled circles) and 0 mol % biotin-cap-DOPE (open circles). The solid line is the fit to the cooperativity binding model. The error bars represent the standard deviation from three independent experiments.

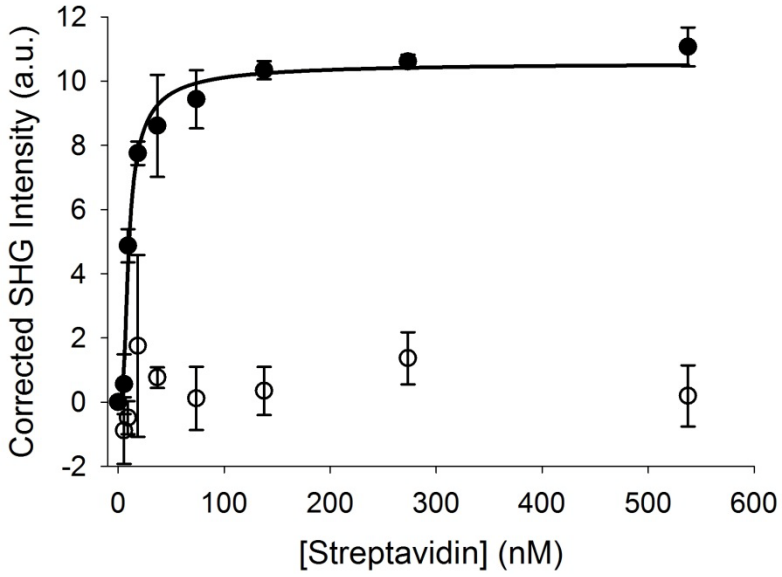

Figure 3.4 Corrected SHG intensity vs. bulk protein concentration for streptavidin binding to DOPC bilayers containing 4 mol % biotin-cap-DOPE (filled circles) and 0 mol % biotin-cap-DOPE (open circles). The solid line is the fit to the cooperativity binding model. The error bars represent the standard deviation from three independent experiments.

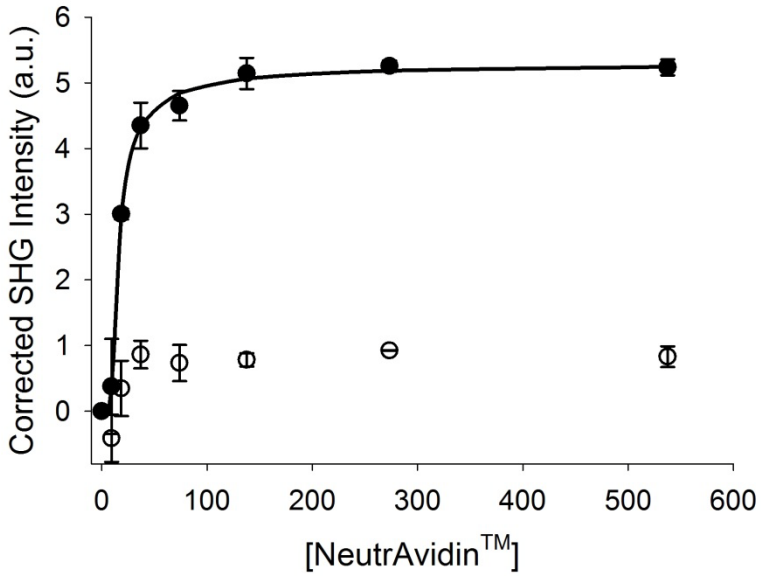

Figure 3.5 Normalized SHG intensity vs. bulk protein concentration for neutrAvidin™ binding to DOPC bilayers containing 4 mol % biotin-cap-DOPE (filled circles) and 0 mol % biotin-cap-DOPE (open circles). The solid line is the fit to the cooperativity binding model. The error bars represent the standard deviation from two independent experiments.

protein concentration until saturation coverage is achieved at concentration greater than 100 nM. The Langmuir and cooperativity models were both used to fit the binding isotherms and the *f*-test was then performed to determine the best fit for the data.

The Langmuir model (equation 3.6) was used to fit the binding data with the fitting parameters B, C, $\sqrt{I_{SHG}^{Max}}$ and K_o by performing a nonlinear least-square regression. The cross term in equation 8 is the product of the nonresonant, A, and real component, B, of the resonant susceptibility tensor which describes the interference between the background and protein adsorption responses. Assuming the nonresonant term A is real and positive, the measured SHG intensity can increase or decrease due to constructive (A and B have the same sign) or destructive (A and B have different signs) interference. In this work as seen in Figures 3.3-3.5, no initial decrease in the SHG intensity was observed at low protein concentrations where the contribution of the resonant term is presumably not much greater than the nonresonant contribution, suggesting there is constructive interference between the background and protein responses. This indicates the cross term ($2AB$) will be positive such that A and B have the same sign. Additionally, the results from the nonlinear regression indicate that the magnitude of B is approximately eight orders of magnitude smaller than magnitude of the imaginary portion of the resonant susceptibility tensor (C). Since the contribution from the cross term $\left(2B\sqrt{I_{SHG}^{background}}\right)$ in equation 8 is much smaller compared to the resonant contribution term ($B^2 + C^2$), it can be neglected. The resonant contribution term ($B^2 + C^2$), which is related to the surface density (see equation 2.19 in Chapter 2), serves as a scaling factor,

and can then be pooled into $\sqrt{I_{SHG}^{Max}}$. Using these simplifications, the final Langmuir equation used to fit the adsorption data in this study is:

$$I_{SHG} \propto \left(\frac{\sqrt{I_{SHG}^{Max}}\, K_o[P]}{1 + K_o[P]} \right)^2 . \tag{3.10}$$

The cooperativity model (equation 3.8) was also used to fit the binding data with the fitting parameters B, C, $N_{max,}$ K_o and ω. The fitting results also showed that $\left(2B\sqrt{I_{SHG}^{background}}\right)$ is seven orders of magnitude lower than (B^2 + C^2), and thus the contribution of the cross term in equation 3.8 is negligible. Therefore, the final form of the cooperativity model used to fit the data has the form:

$$I_{SHG} \propto \left(\frac{\sqrt{I_{SHG}^{Max}}\, \omega^{\left(\sqrt{I_{SHG}} \Big/ \sqrt{I_{SHG}^{Max}} \right)} K_o[P]}{1 + \omega^{\left(\sqrt{I_{SHG}} \Big/ \sqrt{I_{SHG}^{Max}} \right)} K_o[P]} \right)^2 . \tag{3.11}$$

The equations 3.10 (Langmuir model) and 3.11 (cooperativity model) were then used to fit the adsorption data of avidin and its analogs, streptavidin and neutrAvidin™ shown in Figures 3.3-3.5. It was found that the cooperativity model (equation 3.11) statistically fit the data best and the results from a nonlinear least-square regression of the data are given in Table 3.1.

The results summarized in Table 3.1 show that the binding affinities, K_o, of avidin, streptavidin, neutrAvidin™ to a biotinylated DOPC bilayer, $8.2 \pm 2.4 \times 10^7\ M^{-1}$,

Table 3.1 Measured intrinsic binding affinity and cooperativity coefficient for avidin, streptavidin, and neutrAvidin™.

Protein	$K_o \times 10^7$ (M^{-1})	η (a.u.)
Avidin	8.2 ± 2.4	1.2 ± 0.2
Streptavidin	4.3 ± 0.9	1.8 ± 0.2
NeutrAvidin™	2.6 ± 0.01	1.9 ± 0.01

$4.3 \pm 0.9 \times 10^7\ M^{-1}$ and $2.6 \pm 0.01 \times 10^7\ M^{-1}$, respectively, are quite comparable. The binding affinity of avidin to biotin obtained in this study is in good agreement with the value of $2.14 \pm 0.20 \times 10^7\ M^{-1}$ previously reported by Zhao *et al.* for fluorescently labeled avidin binding to a 0.63 mol % biotinylated lipid (a ligand density high enough to bind to a monolayer of avidin) incorporated into an arachidic acid monolayer.[29] For streptavidin, the biotin-binding affinity obtained here is slightly higher than the value of $7.3 \pm 0.2 \times 10^6\ M^{-1}$ reported by Tang and coworkers for streptavidin binding a biotin monolayer functionalized on a SPR gold chip surface.[40] The difference in the binding affinity of streptavidin between the two studies can be related to the difference in the surface density of biotin used. It is likely that the high density of biotin used in the SPR study creates steric hindrance which lowers the accessibility of an individual biotin to the protein binding sites, resulting in a lower binding affinity. For neutrAvidin™ binding to the protein binding sites, resulting in a lower binding affinity. For neutrAvidin™ binding to biotin, the K_o of $1.6 \pm 1.1 \times 10^7\ M^{-1}$ measured in this study is about 4.5 orders of magnitude smaller than an affinity of $5.5 \pm 0.2 \times 10^{11}\ M^{-1}$ reported by Wayment and Harris using single-molecule fluorescence.[23] In order to compare the result of Wayment and Harris' study with the one of the current study, we performed a similar analysis of the kinetics of protein binding which is presented in the following section. It was shown that the slower adsorption and desorption rates of biotin-neutrAvidin™ measured in this study lead to the lower binding affinity.

As previously mentioned, the cooperativity binding model was statistically the best fit to the data obtained in the present work. This indicates that protein-protein interactions are involved in the biotin-protein binding. The value of the cooperativity

coefficient η obtained from the fit is shown in Table 3.1. A value of η greater than unity was obtained for avidin, streptavidin and neutrAvidin™, illustrating that all the proteins exhibit positive cooperative binding behavior. This suggests that the binding of the proteins to biotin is increased due to protein-protein interactions. Similar cooperative binding behavior has been previously observed for avidin to a monolayer of arachidic acid containing biotinylated lipid.[29] The cooperative binding of avidin was only observed if the biotin density was adequately high to bind to a monolayer of avidin so that the distance between the biotin molecules is close enough for the adjacent biotin bound avidin to interact with an incoming avidin.[29] Additionally, biotin needs to be placed above the lipid surface, i.e., by the use of a spacer between biotin and the lipid head group, to provide more accessibility for avidin binding.[29] The use of a biotin density high enough to form a monolayer of the proteins (~ 4 mol % biotin) and the spacer between biotin and the lipid head group (biotin-cap-DOPE) in the present study allows for protein-protein interactions to occur.

Interestingly, in this study avidin was found to have a smaller η (1.2 ± 0.2) as compared to streptavidin and neutrAvidin™ (1.8 ± 0.2 and 1.9 ± 0.01) indicating that avidin exhibits less positive cooperative binding. The lower cooperativity observed for avidin could be related to the high pI (~ 10) of the protein. At the neutral pH used here, avidin is positively charged, and thus the electrostatic repulsion between the charged avidin proteins could repel the proteins from each other resulting in a reduction in avidin-avidin interactions. On the other hand, streptavidin and neutrAvidin™ have a pI close to 7. Therefore, electrostatic interaction between streptavidin and streptavidin or neutrAvidin™ and neutrAvidin™ is less pronounced as compared to that of avidin-avidin

interactions, resulting in a higher cooperativity coefficient obtained for streptavidin and neutrAvidin™.

The level of cooperative binding observed in avidin, streptavidin and neutrAvidin™ can also be evaluated in terms of the binding free energy. Without any contributions from protein-protein interaction, the free energy of protein-biotin binding, ΔG_o, can be calculated from the intrinsic binding affinity K_o:

$$\Delta G_o = - RT \ln K_o \, . \tag{3.12}$$

The calculated values of ΔG_o for the three proteins are listed in Table 3.2. When the protein-protein interaction is not included, ΔG_o of avidin binding to biotin (- 45 ± 0.2 kJ/mol) is slightly higher than that of streptavidin (- 43 ± 0.7 kJ/mol) and neutrAvidin™ (- 42 ± 0.5 kJ/mol).

The free energy ΔG_η of protein-protein interactions, previously described by Zhao *et al.*,[29] can be expressed as:

$$\Delta G_\eta = - 4RT \ln(\eta). \tag{3.13}$$

Using equation 3.13, ΔG_η was calculated from the binding isotherms in Figures 3.3 - 3.5 for avidin, streptavidin and neutrAvidin™ and the results are listed in Table 3.2. The protein-protein interactions for avidin contribute a free energy (- 1.7 ± 1.4 kJ/mol K) of about 3 times less than streptavidin and neutrAvidin™ (- 5.7 ± 1.1 and - 6.3 ± 0.04 kJ/mol K).

The total free energy of the protein-biotin binding including the contribution from the protein-protein interactions was determined using the following equation:

Table 3.2 Calculated intrinsic free energy, free energy due to protein-protein interactions, total free energy, and apparent binding affinity for avidin, streptavidin, and neutrAvidin™.

Protein	ΔG_o (kJ/mol)	ΔG_η (kJ/mol)	ΔG_{total} (kJ/mol)	$K_{app} \times 10^7$ (M^{-1})
Avidin	- 45 ± 0.8	- 1.7 ±1.4	- 47 ± 1.7	18 ± 14
Streptavidin	- 44 ± 0.5	- 5.7 ± 1.1	- 49 ± 0.6	44 ± 10
NeutrAvidin™	- 42 ± 0.01	- 6.3 ± 0.01	- 49 ± 0.05	33 ± 0.7

$$\Delta G_{total} = \Delta G_o + \Delta G_\eta \,, \tag{3.14}$$

the results of which are listed in Table 3.2. The calculated total free energy ΔG_{total} of avidin-biotin binding (- 47 ± 1.7 kJ/mol) is now lower than ΔG_{total} of streptavidin (- 49 ± 0.6 kJ/mol) and neutrAvidin™ (- 49 ± 0.05 kJ/mol) binding to biotin. Accordingly, the binding between biotin and streptavidin or biotin and neutrAvidin™ becomes more energetically favorable due to the stronger protein-protein interaction as compared to the avidin-biotin binding.

From ΔG_{total} calculated above, the apparent binding affinity K_{app} of the proteins to a biotinylated lipid bilayer was calculated and the results are given in Table 3.2. The larger calculated values for K_{app} as compared to the intrinsic binding affinity K_o reveal that the the binding affinity of the proteins toward biotin is enhanced by protein-protein interactions. When these protein-protein interactions are taken into account, avidin has the lowest biotin-binding affinity of 18 ± 14 × 10^7 M^{-1} while streptavidin and neutrAvidin™ exhibit stronger binding affinities of 44 ± 10 × 10^7 M^{-1} and 33 ± 0.3 × 10^7 M^{-1}, respectively.

3.3.2 Nonspecific Adsorption of Avidin, NeutrAvidin™ and Streptavidin to a DOPC Bilayer

The nonspecific adsorption of avidin, streptavidin and neutrAvidin™ to the IgG passivated DOPC bilayer without the biotin ligand is shown by the open circles in Figures 3.3 - 3.5. The amount of nonspecific adsorption of the proteins can be evaluated using the square-root of the SHG intensity, $\sqrt{I_{SHG}}$, which is directly proportional to the surface concentration of the protein. To compare the amount of nonspecific adsorption,

the % surface coverage in the absence of biotin at 537.6 nM (above saturation concentration) relative to the calculated monolayer coverage of adsorbed protein in the presence of biotin was calculated. Surprisingly, neutrAvidin^{TM} has the highest degree of nonspecific adsorption (~ 40%) to a pure DOPC bilayer as compared no appreciable nonspecific adsorption of avidin and streptavidin. Similar behavior has previously been reported for the nonspecific adsorption of neutrAvidin^{TM} to a silica surface where its nonspecific adsorption is about three-fold greater than that of avidin.[20] The higher degree of nonspecific adsorption of neutrAvidin^{TM} is unexpected because the deglycosylation and lower pI of neutrAvidin^{TM} are intended to decrease its nonspecific adsorption relative to avidin. It is important to mention that although streptavidin is also a nonglycosylated protein and has a similar pI to neutrAvidin^{TM}, the degree of nonspecific adsorption of streptavidin is much less. Consequently, the removal of the carbohydrate groups and the lower pI of neutrAvidin^{TM} cannot account for the greater nonspecific adsorption of the protein observed in this study.

3.3.3 Kinetics of Avidin Binding to a Biotinylated DOPC Bilayer

In addition to obtaining the binding affinity of the protein to biotin from the equilibrium thermodynamics, the binding affinity from kinetic measurements can also be determined. The comparison between the binding affinities obtained from the thermodynamic and kinetic measurements will indicate whether or not the thermodynamic study was made under steady-state equilibrium. The kinetics of protein binding to a biotinylated DOPC bilayer can be described by the Langmuir kinetic model[51] where the protein adsorption rate (k_{on}) is first-order with respect to the bulk protein concentration C_{bulk} and fraction of unbound biotin (1-θ), and the protein desorption rate

(k_{off}) is first-order with respect to the fraction of protein bound biotin (θ). The rate of change in the fraction of protein bound biotin is the difference between the adsorption rate and desorption rate as given by:

$$\frac{d\theta}{dt} = k_{on}C_{bulk}(1 - \theta) - k_{off}\theta \,. \tag{3.15}$$

θ is the ratio of the square-root SHG intensity and the square-root of the maximum SHG intensity at saturation. The Langmuir kinetic model used here assumes the bulk concentration of the protein is unchanged with time. This assumption is valid for the current study as the protein concentration was replenished during the adsorption process.

Since the SHG intensity and subsequently θ were measured with increasing the bulk protein concentration throughout the course of a single experiment, the change in θ as function of time at each bulk protein concentration can be plotted separately by setting the time t that a new C_{bulk} was introduced into the system to zero. The corresponding θ_o at $t = 0$ at each C_{bulk} is the maximum θ obtained at the previous bulk protein concentration. θ for avidin binding to a 4 mol % biotinylated DOPC bilayer as a function of time in the concentration range from 9.25 nM to 537.6 nM is plotted in Figure 3.6.

Equation 3.15 was solved with the boundary conditions such that at time $t = 0$, the initial surface coverage fraction is θ_o, and at time $t > 0$ the surface coverage fraction is θ. These boundary conditions allow the kinetics of protein binding at each bulk protein concentration to be evaluated. The solution for equation 3.15 with the above stated boundary conditions is:

$$\theta = \frac{k_{on}C_{bulk}}{k_{on}C_{bulk} + k_{off}}\left[1 - \exp(-k_{on}C_{bulk} + k_{off})t\right] + \theta_o \exp(-k_{on}C_{bulk} + k_{off})t \,, \tag{3.16}$$

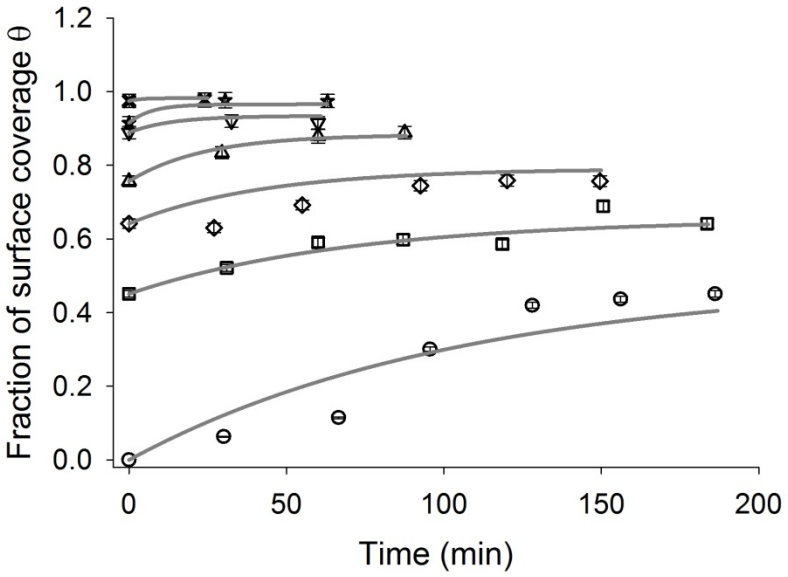

Figure 3.6 Fraction of surface coverage, θ, vs. time of avidin binding to a 4 mol % biotinylated DOPC bilayer at the following bulk avidin concentration: 9.25 nM (circles), 18.5 nM (squares), 37.0 nM (diamonds), 73.7 nM (upright triangles), 137.7 nM (inverted triangles), 273.2 nM (stars), and 537.6 nM (crosses). The lines are the global fit to equation 3.16.

θ_o in equation 3.16 is zero for the first and lowest protein concentration. When the next protein concentration is added, θ_o is the maximum fraction of surface coverage at the previous protein concentration.

Using equation 3.16 to simultaneously fit all adsorption data in Figure 3.6 gives the adsorption rate, $k_{on} = (9.8 \pm 5.3) \times 10^3$ M^{-1} s^{-1} and the desorption rate, $k_{off} = (6.0 \pm 1.8) \times 10^{-5}$ s^{-1}. From the measured k_{on} and k_{off}, the affinity of avidin binding to a 4 mol % biotinylated lipid bilayer can be calculated by $K_a = k_{on}/k_{off} = (16 \pm 10) \times 10^7$ M^{-1}. This value is consistent with the K_{app} of avidin ($(18 \pm 14) \times 10^7$ M^{-1}) obtained from steady-state equilibrium thermodynamics measurements presented in the previous section. The agreement between the binding affinity obtained from the kinetics and thermodynamics indicates that there was sufficient time for each protein concentration to reach equilibrium in the thermodynamic measurement.

As previously mentioned, there is a large discrepancy between the binding affinity measured in this work and Wayment and Harris' one. This discrepancy can be explained using the binding kinetics result obtained from the two studies as the same Langmuir kinetic model was used to analyze the data. Here the measured k_{on} is about 4.5 orders of magnitude slower than that reported by Wayment and Harris ($(2.1 \pm 0.5) \times 10^8$ M^{-1} s^{-1}).[23] The much slower adsorption rate at a high density of biotin to form a monolayer coverage of the protein suggests that the binding affinity of avidin to biotin is much weaker in this work. A speculative explanation for this behavior is that the avidin-biotin binding might involve two regimes: i) at a very low bulk protein concentration, the protein binds to biotin with a very high affinity as observed by Wayment and Harris; and ii) at a higher bulk protein concentration, the protein binds to biotin with a lower affinity as seen here.

Since a biphasic binding isotherm was not observed in this study, it is possible that the protein with the high binding affinity to biotin saturates at very low surface coverage. Using a pM range of bulk protein concentration to bind to a very small biotin density to form less than 10^{-6} of a protein monolayer, the high affinity binding regime of the protein could be detected as seen by Wayment and Harris. In contrast, with a higher bulk protein concentration (~ nM) and a large surface coverage of bound protein, the high affinity sites cannot be observed as they do not account for much of the surface density of bound protein. This explains the measured lower affinity of the protein binding to biotin in this study because the more moderate affinity sites are more prevalent. Additionally, k_{off} in this study is ~ 1.5 orders of magnitude slower than the value measured by Wayment and Harris ($(3.8 \pm 0.5) \times 10^{-4}$ s^{-1}),[18] illustrating the formation of the longer-lived doubly biotin-neutrAvidin™ complex in this work. The slower adsorption and desorption rates of avidin binding obtained here result in a smaller binding affinity relative to the high binding affinity seen in Wayment and Harris' work.

3.3.4 Binding of Anti-biotin Antibody to a Biotinylated DOPC Bilayer

The binding isotherm for anti-biotin antibody binding to a DOPC bilayer containing 4 mol % biotin-cap-DOPE is shown in Figure 3.7. The binding of anti-biotin was fit using the Langmuir model from equation 3.11. The binding affinity of anti-biotin antibody to the biotinylated lipid bilayer of $(1.0 \pm 4.0) \times 10^{8}$ M^{-1} measured here is close to the value ($(2.8 \pm 0.8) \times 10^{8}$ M^{-1}) obtained by Jung *et al.* for fluorescently labeled anti-biotin antibody binding to 5 mol % biotin-cap-PE incorporated into a lipid bilayer.[25]

A direct comparison between the binding affinities measured in this study for anti-biotin antibody, avidin, streptavidin and neutrAvidin™ can be made as they were all

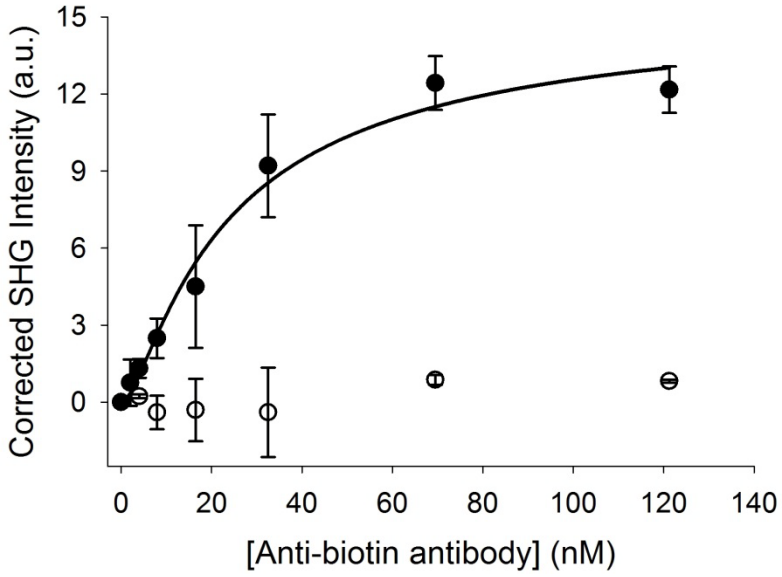

Figure 3.7 Normalized SHG intensity vs. bulk protein concentration for anti-biotin antibody binding to DOPC bilayers containing 4 mol % biotin-cap-DOPE (filled circles) and 0 mol % biotin-cap-DOPE (open circles). The solid line is the fit to the Langmuir model. The error bars represent the standard deviation from at least two independent experiments.

determined under similar experimental conditions. The apparent binding affinity of avidin, streptavidin and neutrAvidin™ were used in the comparison as it takes account into protein-protein interactions involved in the binding of these proteins. Since no protein-protein interactions were observed in anti-biotin antibody, thus the apparent binding affinity is equal to the intrinsic binding affinity. Interestingly, the binding affinity of anti-biotin antibody to a biotinylated lipid bilayer was found to have the same order of magnitude (~ 10^8 M^{-1}) as the apparent binding affinity of avidin, streptavidin and neutrAvidin™. As a result, the free energy of anti-biotin antibody binding to biotin (46 ± 1.0 kJ/mol) is also close to those of avidin, streptavidin and neutrAvidin™ (see Table 3.1).

Streptavidin and anti-biotin antibody have also been previously found to have the same affinity to biotin when biotin is attached to bovine serum albumin (BSA) via a caproic acid linker[52] even though it is well known that anti-biotin antibody binds to free biotin in solution with a much lower affinity than avidin.[52,53] This could be explained by the higher dependence of avidin's binding affinity on the biotin accessibility, i.e., lower accessibility of biotin when it is attached to a macromolecule and higher biotin accessibility when it is free in solution. The avidin's binding sites are located in a depression near the end of the β-barrels[22] which makes it more difficult to bind with biotin when biotin is bound to a macromolecule and therefore, lowers the binding affinity of avidin.[52,54] Unlike the binding sites of avidin, anti-biotin antibody's binding sites are located on the end of the Fab segments, not in the depression,[55] which makes the binding affinity of anti-biotin antibody less dependent on the accessibility of biotin.[52] Furthermore, the Fab segments of the antibody are connected by a hinge that allows the

Fab segments to move from about 0° to 180°.[56] The flexibility of the Fab segments, including the arm rotation, elbow bend and arm wagging,[57] allows the antibody to adjust the spacing and orientation of its binding sites and thus facilitates the binding of the antibody to the ligand.[55,56] Therefore, the biotin-binding of anti-biotin antibody is not significantly affected by the accessibility of biotin, whereas the lower accessibility of biotin in the biotinylated lipid bilayer causes a reduction in the binding affinity of avidin, streptavidin and neutrAvidin™ to a biotinylated lipid bilayer. This results in the same order of magnitude of the binding affinity for all four proteins to the biotinylated lipid bilayer obtained in the present study.

Another interesting feature observed here is the nonspecific adsorption of anti-biotin antibody to a pure DOPC bilayer is negligible as compared to its specific binding (see Figure 3.7). It should be noted that no IgG from rabbit serum was used to suppress the nonspecific adsorption of anti-biotin antibody in this experiment. Therefore, this feature could make the anti-biotin antibody-biotin complex a prominent tether/linker in all bioanalytical applications as the time and cost in minimizing the protein's nonspecific adsorption can be avoided.

3.4 Summary

The binding of avidin, streptavidin, neutrAvidin™, and anti-biotin antibody to a biotinylated lipid bilayer was investigated using SHG spectroscopy. The binding affinities of avidin, streptavidin, neutrAvidin™ and anti-biotin antibody to 4 mol % biotin-cap-DOPE incorporated into a DOPC lipid were determined and correlated to the values published in the literature, validating the capability of SHG in detection of protein-ligand interactions without using any extrinsic label. A positive cooperative binding

behavior was obtained for avidin and its analogs, streptavidin and neutrAvidin™, demonstrating that protein-protein interactions enhance the binding of the proteins to biotin. In fact, the binding of streptavidin and neutrAvidin™ to biotin is more energetically favorable than avidin due to the stronger protein-protein interactions. Although neutrAvidin™ is designed to lower the nonspecific adsorption, we have found that it exhibits the greatest degree of nonspecific adsorption to a DOPC bilayer as compared to avidin and streptavidin. Anti-biotin antibody was found to bind to a biotinylated lipid bilayer with a similar affinity as avidin, streptavidin and neutrAvidin™. Furthermore, anti-biotin antibody showed negligible nonspecific adsorption to a DOPC bilayer without the use of an additional agent to reduce the protein's nonspecific adsorption. The study presented in this chapter has demonstrated the utility of SHG as an attractive alternative in measuring protein-ligand interactions without the need for chemical modification. Furthermore, this study provides a deeper understanding about the binding properties of avidin, streptavidin, neutrAvidin™ and anti-biotin antibody to the ligand biotin at lipid bilayer surfaces, which can further assist in selecting an appropriate tether/linker for biosensing and other bioanalytical applications.

3.5 References

(1) Grunwell, J. R.; Glass, J. L.; Lacoste, T. D.; Deniz, A. A.; Chemla, D. S.; Schultz, P. G. *J. Am. Chem. Soc.* **2001**, *123*, 4295-4303.

(2) Wennmalm, S.; Edman, L.; Rigler, R. *Proc. Natl. Acad. Sci. U. S. A.* **1997**, *94*, 10641-10646.

(3) Ladd, J.; Boozer, C.; Yu, Q.; Chen, S.; Homola, J.; Jiang, S. *Langmuir* **2004**, *20*, 8090-8095.

(4) Esseghaier, C.; Helali, S.; Ben Fredj, H.; Tlili, A.; Abdelghani, A. *Sens. Actuators, B* **2008**, *B131*, 584-589.

(5) Xu, F.; Zhen, G.; Yu, F.; Kuennemann, E.; Textor, M.; Knoll, W. *J. Am. Chem. Soc.* **2005**, *127*, 13084-13085.

(6) Sun, H.; Choy, T. S.; Zhu, D. R.; Yam, W. C.; Fung, Y. S. *Biosens. Bioelectron.* **2009**, *24*, 1405-1410.

(7) Hall, W. P.; Ngatia, S. N.; Van Duyne, R. P. *J. Phys. Chem. C* **2011**, *115*, 1410-1414.

(8) Bai, S.; Zhao, J.; Zhang, Y.; Huang, W.; Xu, S.; Chen, H.; Fan, L.-M.; Chen, Y.; Deng, X. W. *Appl. Microbiol. Biotechnol.* **2010**, *86*, 983-990.

(9) Litos, I. K.; Ioannou, P. C.; Christopoulos, T. K.; Traeger-Synodinos, J.; Kanavakis, E. *Biosens. Bioelectron.* **2009**, *24*, 3135-3139.

(10) Bashir, R.; Gomez, R.; Sarikaya, A.; Ladisch, M. R.; Sturgis, J.; Robinson, J. P. *Biotechnol. Bioeng.* **2001**, *73*, 324-328.

(11) Lazcka, O.; Del Campo, F. J.; Munoz, F. X. *Biosens. Bioelectron.* **2007**, *22*, 1205-1217.

(12) Barton, A. C.; Davis, F.; Higson, S. P. J. *Anal. Chem. (Washington, DC, U. S.)* **2008**, *80*, 9411-9416.

(13) Zhavnerko, G. K.; Yi, S. J.; Chung, S. H.; Yuk, J. S.; Ha, K. S. *NATO Sci. Ser., II* **2004**, *152*, 95-108.

(14) Cooper, M. A. *Nat. Rev. Drug Discovery* **2002**, *1*, 515-528.

(15) Okumus, B.; Wilson, T. J.; Lilley, D. M. J.; Ha, T. *Biophys. J.* **2004**, *87*, 2798-2806.

(16) Han, N.-Y.; Hautala, J. T.; Bo, T.; Wiedmer, S. K.; Riekkola, M.-L. *Electrophoresis* **2006**, *27*, 1502-1509.

(17) Garifallou, G. Z.; Tsekenis, G.; Davis, F.; Higson, S. P. J.; Millner, P. A.; Pinacho, D. G.; Sanchez-Baeza, F.; Marco, M. P.; Gibson, T. D. *Anal. Lett.* **2007**, *40*, 1412-1422.

(18) Green, N. M. *Biochem. J.* **1963**, *89*, 585-591.

(19) Green, N. M. *Adv. Protein Chem.* **1975**, *29*, 85-133.

(20) Wolny, P. M.; Spatz, J. P.; Richter, R. P. *Langmuir* **2010**, *26*, 1029-1034.

(21) DeLange, R. J. *J. Biol. Chem.* **1970**, *245*, 907-916.

(22) Green, N. M. *Methods Enzymol.* **1990**, *184*, 51-67.

(23) Wayment, J. R.; Harris, J. M. *Anal. Chem.* **2009**, *81*, 336-342.

(24) Priece Biotechnology *Instructions for NeutrAvidin*, (prod. number 31000).

(25) Jung, H.; Yang, T.; Lasagna, M. D.; Shi, J.; Reinhart, G. D.; Cremer, P. S. *Biophys. J.* **2008**, *94*, 3094-3103.

(26) Osborne, M. A. *J. Phys. Chem. B* **2005**, *109*, 18153-18161.

(27) Patel, A. R.; Frank, C. W. *Langmuir* **2006**, *22*, 7587-7599.

(28) Sandrin, L.; Coche-Guerente, L.; Bernstein, A.; Basit, H.; Labbe, P.; Dumy, P.; Boturyn, D. *Org. Biomol. Chem.* **2010**, *8*, 1531-1534.

(29) Zhao, S.; Walker, D. S.; Reichert, W. M. *Langmuir* **1993**, *9*, 3166-3173.

(30) Zhao, S.; Reichert, W. M. *Langmuir* **1992**, *8*, 2785-2791.

(31) Shi, J.; Yang, T.; Kataoka, S.; Zhang, Y.; Diaz, A. J.; Cremer, P. S. *J. Am. Chem. Soc.* **2007**, *129*, 5954-5961.

(32) Marsh, D. *CRC Handbook of Lipid Bilayers*; CRC Press: Boca Raton, Florida, 1990.

(33) Smith, K. A.; Gale, B. K.; Conboy, J. C. *Anal. Chem.* **2008**, *80*, 7980-7987.

(34) Mao, H.; Yang, T.; Cremer, P. S. *Anal. Chem.* **2002**, *74*, 379-385.

(35) Yang, T.; Baryshnikova, O. K.; Mao, H.; Holden, M. A.; Cremer, P. S. *J. Am. Chem. Soc.* **2003**, *125*, 4779-4784.

(36) Pisarchick, M. L.; Thompson, N. L. *Biophys. J.* **1990**, *58*, 1235-1249.

(37) Sun, Y. S.; Landry, J. P.; Fei, Y. Y.; Zhu, X. D.; Luo, J. T.; Wang, X. B.; Lam, K. S. *Langmuir* **2008**, *24*, 13399-13405.

(38) Kuziemko, G. M.; Stroh, M.; Stevens, R. C. *Biochemistry* **1996**, *35*, 6375-6384.

(39) Mann, D. A.; Kanai, M.; Maly, D. J.; Kiessling, L. L. *J. Am. Chem. Soc.* **1998**, *120*, 10575-10582.

(40) Tang, Y.; Mernaugh, R.; Zeng, X. *Anal. Chem.* **2006**, *78*, 1841-1848.

(41) Janshoff, A.; Steinem, C.; Sieber, M.; el Baya, A.; Schmidt, M. A.; Galla, H. J. *Eur. Biophys. J.* **1997**, *26*, 261-270.

(42) Salafsky, J. S.; Eisenthal, K. B. *J. Phys. Chem. B* **2000**, *104*, 7752-7755.

(43) Hicks, J. M.; Petralli-Mallow, T. *Appl. Phys. B Lasers Opt.* **1999**, *68*, 589-593.

(44) Fujii, S.; Morita, T.; Kimura, S. *J. Pept. Sci.* **2008**, *14*, 1295-1302.

(45) Leray, A.; Leroy, L.; Le Grand, Y.; Odin, C.; Renault, A.; Vie, V.; Rouede, D.; Mallegol, T.; Mongin, O.; Werts, M. H. V.; Blanchard-Desce, M. *Langmuir* **2004**, *20*, 8165-8171.

(46) Conboy, J. C.; Kriech, M. A. *Anal. Chim. Acta* **2003**, *496*, 143-153.

(47) Kriech, M. A.; Conboy, J. C. *J. Am. Chem. Soc.* **2003**, *125*, 1148-1149.

(48) Mitchell, S. A. *J. Phys. Chem. B* **2009**, *113*, 10693-10707.

(49) Havel, H. A.; Chao, R. S.; Haskell, R. J.; Thamann, T. J. *Anal. Chem.* **1989**, *61*, 642-650.

(50) Guyot-Sionnest, P.; Shen, Y. R. *Phys. Rev. B Condens. Matter* **1987**, *35*, 4420-4426.

(51) Langmuir, I. *J. Am. Chem. Soc.* **1918**, *40*, 1361-1402.

(52) Vincent, P.; Samuel, D. *J. Immunol. Methods* **1993**, *165*, 177-182.

(53) Bagci, H.; Kohen, F.; Kuscuoglu, U.; Bayer, E. A.; Wilchek, M. *FEBS Lett.* **1993**, *322*, 47-50.

(54) Brigati, D. J.; Myerson, D.; Leary, J. J.; Spalholz, B.; Travis, S. Z.; Fong, C. K.; Hsiung, G. D.; Ward, D. C. *Virology* **1983**, *126*, 32-50.

(55) Tsai, C. S. *Biomacromolecules: Introduction to Structure, Function and Informatics*; John Wiley & Sons: New Jersey, 2007.

(56) Hanson, D. C.; Yguerabide, J.; Schumaker, V. N. *Biochemistry* **1981**, *20*, 6842-6852.

(57) Burton, D. R. *Mol. Immunol.* **1985**, *22*, 161-206.

CHAPTER 4

GENERAL PRINCIPLES OF ULTRAVIOLET-VISIBLE SUM-FREQUENCY GENERATION

Sum-frequency generation (SFG) is a coherent second-order nonlinear optical process in which the two input beams at frequencies ω_1 and ω_2 are combined to generate the third beam whose frequency, ω_3, is the sum of the input frequencies ($\omega_3 = \omega_1 + \omega_2$). Since a complete theory of SFG has been presented in the literature,[1,2] only the general principles of SFG will be described in this chapter. Special attention is given to the counter-propagating geometry which will be used in the study described in Chapter 5. This optical geometry allows for a better separation of the SFG beam from the incident beams. The specific case of SFG generated by the combination of ultraviolet and visible laser sources will also be discussed.

4.1 General Principles of SFG

SFG is a more general case of SHG where the frequencies of the two incident photons are not the same. SFG is governed by an induced nonlinear polarization at ω_3, $P(\omega_3)$, generated when the input photons, ω_1 and ω_2, spatially and temporally overlap at a surface. $P(\omega_3)$ is given as:

$$P(\omega_3) = \chi^{(2)}_{ijk} E_j(\omega_1) E_k(\omega_2) , \qquad (4.1)$$

where $\chi^{(2)}_{ijk}$ is a third rank tensor which describes the macroscopic response of the system to the applied electric fields $E_j(\omega_1)$ and $E_k(\omega_2)$. The indices represent the output SFG (i) and input fields (j,k) which can assume any of the three Cartesian coordinates (x,y,z). As a result, $\chi^{(2)}_{ijk}$ is composed of 27 elements, thus the induced polarization can be mathematically expressed as:

$$\begin{bmatrix} P_x(\omega_3) \\ P_y(\omega_3) \\ P_z(\omega_3) \end{bmatrix} = \begin{bmatrix} \chi_{xxx} & \chi_{xxy} & \chi_{xxz} & \chi_{xyx} & \chi_{xyy} & \chi_{xyz} & \chi_{xzx} & \chi_{xzy} & \chi_{xzz} \\ \chi_{yxx} & \chi_{yxy} & \chi_{yxz} & \chi_{yyx} & \chi_{yyy} & \chi_{yyz} & \chi_{yzx} & \chi_{yzy} & \chi_{yzz} \\ \chi_{zxx} & \chi_{zxy} & \chi_{zxz} & \chi_{zyx} & \chi_{zyy} & \chi_{zyz} & \chi_{zzx} & \chi_{zzy} & \chi_{zzz} \end{bmatrix} \times \begin{bmatrix} E_x(\omega_1)\ E_x(\omega_2) \\ E_x(\omega_1)\ E_y(\omega_2) \\ E_x(\omega_1)\ E_z(\omega_2) \\ E_y(\omega_1)\ E_x(\omega_2) \\ E_y(\omega_1)\ E_y(\omega_2) \\ E_y(\omega_1)\ E_z(\omega_2) \\ E_z(\omega_1)\ E_x(\omega_2) \\ E_z(\omega_1)\ E_y(\omega_2) \\ E_z(\omega_1)\ E_z(\omega_2) \end{bmatrix}. \tag{4.2}$$

Similar to SHG, the second order susceptibility, $\chi^{(2)}_{ijk}$, is dependent on the symmetry of the system. The $C_{\infty v}$ symmetry at the interface between the two isotropic media allows four unique $\chi^{(2)}_{ijk}$ tensor elements, χ_{zzz}, χ_{zii}, χ_{iiz} and χ_{izi} ($i = x$ or y) to persist.

The components of the induced polarization in the Cartesian coordinate system of the interface (x,y,z) can be expressed in terms of the nonzero tensor elements:

$$P_x(\omega_3) = \chi_{xxz}\, E_x(\omega_1)\, E_z(\omega_2) + \chi_{xzx}\, E_z(\omega_1)\, E_x(\omega_2)\,, \tag{4.3a}$$

$$P_y(\omega_3) = \chi_{yyz}\, E_y(\omega_1)\, E_z(\omega_2) + \chi_{yzy}\, E_z(\omega_1)\, E_y(\omega_2)\,, \tag{4.3b}$$

$$P_z(\omega_3) = \chi_{zxx}\, E_x(\omega_1)\, E_x(\omega_2) + \chi_{zyy}\, E_y(\omega_1)\, E_y(\omega_2) + \chi_{zzz}\, E_z(\omega_1)\, E_z(\omega_2)\,. \quad (4.3c)$$

The applied electric field vectors E_x, E_y and E_z in the Cartesian coordinate system (x,y,z) can be transformed into the interfacial coordinate system as shown in Chapter 2, equations 2.4a-c. The induced polarization in the interfacial coordinate system is then given as:

$$P_x(\omega_3) = \sqrt{I_1}\sqrt{I_2}\left[\cos\gamma_1 \cos\gamma_2\left(\cos\theta_1 \sin\theta_2 f_{1x} f_{2z}\, \chi_{xxz} + \sin\theta_1 \cos\theta_2 f_{1z} f_{2x} \chi_{xzx}\right)\right], \quad (4.4a)$$

$$P_y(\omega_3) = \sqrt{I_1}\sqrt{I_2}\left(\sin\theta_2 \sin\gamma_1 \cos\gamma_2 f_{1y} f_{2z}\, \chi_{xxz} + \sin\theta_1 \cos\gamma_1 \sin\gamma_2\, f_{1z} f_{2y}\, \chi_{xzx}\right), \quad (4.4b)$$

$$P_z(\omega_3) = \sqrt{I_1}\sqrt{I_2}\left[\left(\cos\theta_1\cos\theta_2 \cos\gamma_1\cos\gamma_2 f_{1x} f_{2x} + \sin\gamma_1\sin\gamma_2 f_{1y} f_{2y}\right)\chi_{zxx} + \sin\theta_1 \sin\theta_2\cos\gamma_1\cos\gamma_2 f_{1z} f_{2z}\, \chi_{zzz}\right], \quad (4.4c)$$

where I_1 and I_2 the intensities of the input beam 1 and 2, respectively. θ_1 and θ_2 are the incidence angles with respect to the surface normal, γ_1 and γ_2 are the polarization angles relative to the plane of the incidence of the input beam 1 and 2 (see Figure 2.1 in Chapter 2). The linear Fresnel coefficients fs in the transmitted direction are given in equations 2.5a-c in Chapter 2.

The p and s-polarized SFG intensities can be expressed in terms of the induced polarization and a nonlinear Fresnel coefficient $\tilde{f}$ as shown below:

$$I_p = \left|\tilde{f}_x\, P_x(\omega_3) + \tilde{f}_z\, P_z(\omega_3)\right|^2, \quad (4.5a)$$

$$I_s = \left|\tilde{f}_y\, P_y(\omega_3)\right|^2. \quad (4.5b)$$

Substitution of equations 4.4a-c into the expressions for *p*-polarized and *s*-polarized SFG intensities (equations 4.5a-b) yields:

$$I_p = I_1 I_2 \left|\tilde{f}_x\left[\cos\gamma_1 \cos\gamma_2\left(\cos\theta_1 \sin\theta_2 f_{1x} f_{2z} \chi_{xxz} + \sin\theta_1 \cos\theta_2 f_{1z} f_{2x} \chi_{xzx}\right)\right] + \right.$$
$$\tilde{f}_z\left[\left(\cos\theta_1 \cos\theta_2 \cos\gamma_1 \cos\gamma_2 f_{1x} f_{2x} + \sin\gamma_1 \sin\gamma_2 f_{1y} f_{2y}\right) \chi_{zxx} + \right.$$
$$\left.\left.\sin\theta_1 \sin\theta_2 \cos\gamma_1 \cos\gamma_2 f_{1z} f_{2z} \chi_{zzz}\right]\right|^2, \tag{4.6a}$$

$$I_s = I_1 I_2 \left|\tilde{f}_y\left(\sin\theta_2 \sin\gamma_1 \cos\gamma_2 f_{1y} f_{2z} \chi_{xxz} + \sin\theta_1 \cos\gamma_1 \sin\gamma_2 f_{1z} f_{2y} \chi_{xzx}\right)\right|^2. \tag{4.6b}$$

The nonlinear Fresnel coefficients $\tilde{f}$, which describe the propagation of the SFG beam are given in Chapter 2, equations 2.8a-c, 2.9a-c for both reflection and transmission directions. The sum-frequency angle θ^{ω_3} in equations 2.8a-c and 2.9a-c for the nonlinear Fresnel coefficients can be determined by using the momentum conservation of the wave vectors and Snell's law of refraction, such that:

$$k_x(\omega_3) = k_{x_1}(\omega_1) + k_{x_2}(\omega_2), \tag{4.7}$$

where $k_x(\omega_3)$, $k_{x_1}(\omega_1)$ and $k_{x_2}(\omega_2)$ are the wave vectors of the SFG, fundamental beam 1, and fundamental beam 2, respectively. In the case where the fundamental beams propagate through the linear medium n_R, the wave vectors $k_{x_1}(\omega_1)$ and $k_{x_2}(\omega_2)$ can be given by:

$$k_{x_1}(\omega_1) = \frac{n_R \omega_1 \sin\theta_1}{c}, \tag{4.8a}$$

$$k_{x_2}(\omega_2) = \frac{n_R \omega_2 \sin\theta_2}{c}. \tag{4.8b}$$

Substitution of equations 4.8a-b into equation 4.7 yields:

$$k_{x_3}(\omega_3) = \frac{n_R\,\omega_1 \sin\theta_1 + n_R\,\omega_2 \sin\theta_2}{c}. \tag{4.9}$$

Therefore, the reflected $\theta_R^{\omega_3}$ and transmitted $\theta_T^{\omega_3}$ angles of the sum frequency beam are given by:

$$\theta_R^{\omega_3} = \arcsin\left(\frac{n_R\,\omega_1 \sin\theta_1 + n_R\,\omega_2 \sin\theta_2}{n_R\,\omega_3}\right), \tag{4.10a}$$

$$\theta_T^{\omega_3} = \arcsin\left(\frac{n_R \sin\theta_R^{\omega_3}}{n_T\,\omega_3}\right). \tag{4.10b}$$

Similar to SHG, a resonant enhancement in SFG can be achieved by tuning the fundamental frequencies, ω_1, or ω_2, or the SFG frequency, ω_3, to approach the frequency of an optical transition (electronic/vibrational). This leads to an increase in the resonant $\chi_R^{(2)}$, as given by:

$$\chi_R^{(2)} = N\sum_{a,b,c}\frac{\langle a|\mu_i|c\rangle\langle a|\mu_j|b\rangle\langle b|\mu_k|c\rangle}{(h\omega_3 - E_{ca} - i\Gamma_{ca})(h\omega_1 - E_{ab} - i\Gamma_{ab})(h\omega_2 - E_{bc} - i\Gamma_{bc})}, \tag{4.11}$$

where N is the surface density of molecules, h is Planck's constant, μ is the Cartesian coordinate dipole operator, Γ represents the linewidth of the transition, and *a, b* and *c* represent the initial, intermediate and final states, respectively (see Figure 4.1).[1]

The vibrational resonant enhancement feature of SFG has been exploited extensively to study molecular structures at interfaces, including water,[3-5] surfactants,[6-9] proteins[10-13] and lipid structures.[14-16] The vibrational spectra of these interfacial structures are obtained with infrared-visible (IR-Vis) SFG in which the two input beams are a

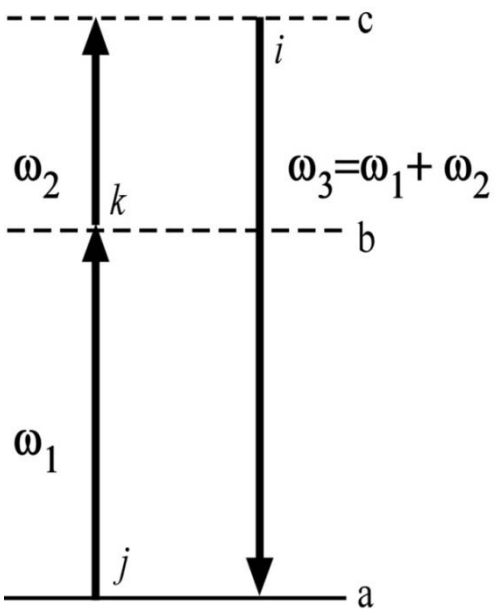

Figure 4.1 Energy level diagram of sum-frequency generation process.

visible source at a fixed frequency and a tunable IR source. When the frequency of the IR is scanned through vibrational resonances of the molecules of interest, such as the C-H stretching modes or amide I region, a sum-frequency vibrational spectrum is obtained by recording the SFG intensity as a function of the IR frequency.

In addition to probing vibrational transitions, SFG can be utilized to probe electronic transitions by using ultraviolet and visible light sources (UV-Vis SFG). UV-Vis SFG emission is in the deep UV range (194-237 nm) allowing the investigation of a variety of biological molecules that contain aromatic groups, such as amino acids, proteins and some drugs. A full description of UV-Vis SFG is presented in the following section.

4.2 Ultraviolet-Visible (UV-Vis) Sum-Frequency Generation

UV-Vis SFG involves the spatial and temporal overlap of a UV source (355 nm) and a tunable visible source (430-710 nm). The resulting SFG occurs in the deep UV wavelength range (194-237 nm). For the work presented in this dissertation, a UV source at 355 nm was used in combination with a fixed visible source at 532 nm to generate a SFG output at 213 nm.

A theoretical SFG response for both *p*- and *s*-output polarization can be calculated using the equations 4.6a-b described above. In the calculation, the 355 nm and 532 nm beams propagated through a silica medium (n_{silica}), arrived at a silica/water interface where they interacted and generated a sum-frequency beam at 213 nm, and then transmitted into a water medium (n_{H_2O}). A counter-propagating geometry was used in the calculation where the two fundamental beams approach the silica/water interface from opposite directions under total internal reflection (TIR) (Figure 4.2).

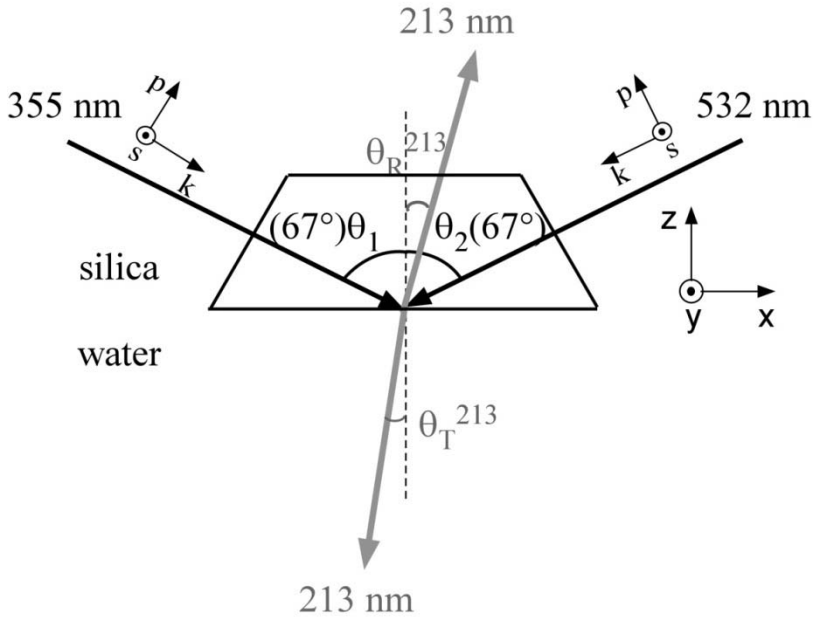

Figure 4.2 Schematic of a counter-propagating geometry used in the UV-Vis SFG calculation. The fundamental beams at 355 nm and 532 nm approach the silica/water interface from opposite direction with the incident angles θ_1 and θ_2, respectively. The sum frequency beam is generated at 213 nm in the reflection (θ_R^{213}) and transmission direction (θ_T^{213}).

In order to calculate the SFG response from equations 4.6a-b, the incident angles θ_1 and θ_2, polarization angles γ_1 and γ_2, linear and nonlinear Fresnel coefficients must be known. To satisfy the TIR condition used here, the incident angles of the 355 nm and 532 nm beams must be greater than the critical angles, which can be determined by:

$$\theta_c^{355} = \arcsin\left(\frac{n_{\mathrm{H2O}}^{355}}{n_{\mathrm{silica}}^{355}}\right), \tag{4.12a}$$

$$\theta_{\mathrm{c}}^{532} = \arcsin\left(\frac{n_{\mathrm{H2O}}^{532}}{n_{\mathrm{silica}}^{532}}\right), \tag{4.12b}$$

where n_{H2O}^{355} and n_{H2O}^{532} are the refractive indices of water for a wavelength of 355 nm and 532 nm, respectively. $n_{\mathrm{silica}}^{355}$ and $n_{\mathrm{silica}}^{532}$ are the refractive indices of silica at a wavelength of 355 nm and 532 nm, respectively. The values of n_{H2O}^{355}, n_{H2O}^{532}, $n_{\mathrm{silica}}^{355}$ and $n_{\mathrm{silica}}^{532}$ are listed in Table 4.1. The calculated critical angles for the 355 nm and 532 nm beams are 66.85° and 66.25°, respectively. Therefore, the incident angles of the fundamental beams (θ^{355} and θ^{532}) are both chosen at 67° for TIR to occur.

The reflected and transmitted angles for UV-Vis SFG, $\theta_{\mathrm{R}}^{213}$ and $\theta_{\mathrm{T}}^{213}$, can then be calculated using equations 4.10a-b as described previously:

$$\theta_{\mathrm{R}}^{213} = \arcsin\left(\frac{n_{\mathrm{silica}}^{355}\,\omega_{355}\,\sin\theta^{355} + n_{\mathrm{silica}}^{532}\,\omega_{532}\,\sin\theta^{532}}{n_{\mathrm{silica}}^{213}\,\omega_{213}}\right), \tag{4.13a}$$

$$\theta_{\mathrm{T}}^{213} = \arcsin\left(\frac{n_{\mathrm{silica}}^{355}\,\omega_{355}\,\sin\theta^{355} + n_{\mathrm{silica}}^{532}\,\omega_{532}\,\sin\theta^{532}}{n_{\mathrm{H2O}}^{213}\,\omega_{213}}\right). \tag{4.13b}$$

The calculated values for $\theta_{\mathrm{R}}^{213}$ and $\theta_{\mathrm{T}}^{213}$ are 10.47° and 11.24°, respectively. Once the reflected $\theta_{\mathrm{R}}^{213}$ and transmitted $\theta_{\mathrm{T}}^{213}$ SFG angles are known, the nonlinear Fresnel

Table 4.1 Indices of refraction of fused silica and water at different wavelengths.

Wavelength (nm)	n_{silica}	n_{water}
213	1.5352	1.4312
355	1.4761	1.3572
532	1.4607	1.3370

coefficients $\tilde{f}^R$ and $\tilde{f}^T$ given in equations 2.8a-c and 2.9a-c can be determined. The linear Fresnel coefficients can be calculated from equations 2.5a-c described in Chapter 2. In the case of TIR geometry where the incident angles of the fundamental beams (θ_I^{355} = θ_I^{532} = 67°) are greater than their critical angles (θ_c^{355} = 66.85° and θ_c^{532} = 66.25°), the sine of the transmitted angles ($\sin\theta_T^{355}$ and $\sin\theta_T^{532}$) of the fundamental beams becomes larger than one and thus, the values of θ_T^{355} and θ_T^{532} become imaginary.

Now that the incident angles of the 355 nm and 532 nm beams (θ_I^{355} and θ_I^{532}), the nonlinear Fresnel $\tilde{f}$ coefficients and the linear Fresnel coefficients f are known, the *p*-polarized and *s*-polarized SFG intensity (equations 4.6a-b) can be expressed in terms of the polarization angles of the fundamental beams, γ_1 and γ_2, and the susceptibility tensor elements. The polarization dependence of the SFG response can then be evaluated by calculating the SFG intensity as a function of γ_1 and γ_2. In this calculation, it is assumed that γ_1 is equal to γ_2 and the intensity of the 355 nm input I_1 is the same as the intensity of the 532 nm input I_2. Additionally, the calculation of the SFG response is only for an achiral surface possessing $C_{\infty v}$ symmetry. The following values for the nonvanishing achiral $\chi^{(2)}$ elements were selected according to Kriech and Conboy for achiral surfaces:[17] $\chi_{xxz} = 1 + i$, $\chi_{xzx} = 1 + i$, $\chi_{zxx} = 1 + i$, and $\chi_{zzz} = 2 + 2i$.

The theoretical reflected *p*- and *s*-polarized SFG responses as a function of γ are shown in Figures 4.3a and b, respectively. The *p*-polarized SFG response for an achiral surface has two maxima at *p* ($\gamma_1 = \gamma_2 = 0°$ and 180°) and two minima at *s* ($\gamma_1 = \gamma_2 = 90°$ and 270°) input polarizations. The *s*-polarized response exhibits four identical peaks that have maxima at *mixed* input polarization ($\gamma_1 = \gamma_2 = 45°$, 135°, 225° and 315°) and minima

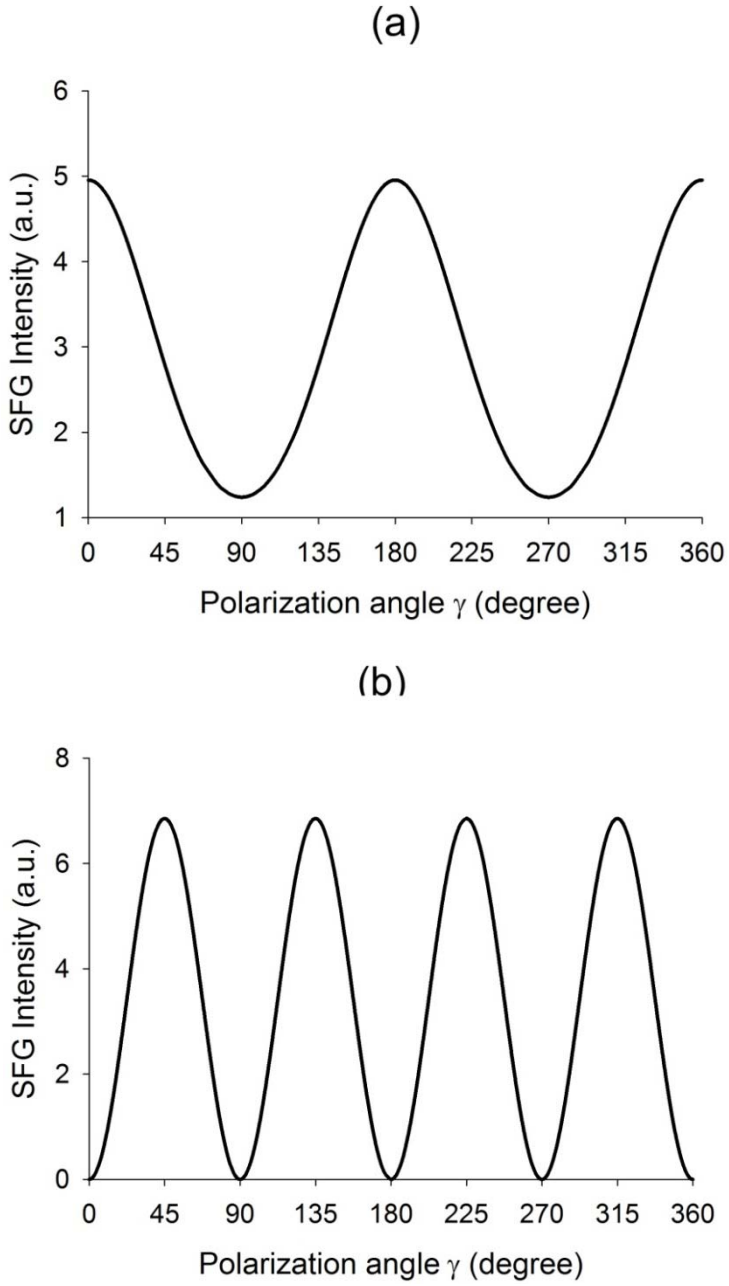

Figure 4.3 Calculated reflected UV-Vis SFG response as a function of incident polarization angle γ for (a) *p*-polarized output and (b) *s*-polarized output.

at *p* ($\gamma_1 = \gamma_2 = 0°$ and 180°) and *s* ($\gamma_1 = \gamma_2 = 90°$ and 270°) input polarizations. It should be noted that the magnitude and shape of the *p*-polarized SFG response varies according to the values of the independent tensor elements in $\chi^{(2)}$. The magnitude of the *s*-polarized SFG response also changes with the χ_{xxz} and χ_{xzx} tensor elements, however its polarization dependence response is independent of the values of the χ_{xxz} and χ_{xzx} tensor elements.

Similarly, theoretical transmitted *p*- and *s*-polarized SFG responses have the same polarization dependence as the reflected SFG responses. As *s*-polarized SFG intensity is maximized at *mixed* input polarization, and thus the intensity at the *mixed* input polarization will be utilized to monitor biomolecular interactions, which will be presented in the following chapter.

4.3 Summary

In this chapter, the general principles of the nonlinear optical spectroscopy SFG were discussed. Similar to SHG, SFG is only allowed at surfaces or interfaces, under electric-dipole approximation, making the technique highly surface specific. Additionally, the resonant enhancement in SFG can be utilized as a sensitive and intrinsic probe to detect biomolecular interactions at a surface. The development of counter-propagating UV-Vis SFG was also presented where the SFG wavelength is in the deep UV (194-237 nm) allowing the ability to detect amino acids, proteins and drugs containing aromatic rings/double bonds. In the next chapter, UV-Vis SFG will be used as a label-free and sensitive technique to study drug-lipid membrane interactions.

4.4 References

(1) Shen, Y. R. *The Principles of Nonlinear Optics*; Wiley: New York, 1984.

(2) Bloembergen, N.; Pershan, P. S. *Physical Review* **1962**, *128*, 606-622.

(3) Salmeron, M.; Bluhm, H. *Surf. Rev. Lett.* **1999**, *6*, 1275-1281.

(4) Asanuma, H.; Noguchi, H.; Uosaki, K.; Yu, H.-Z. *J. Phys. Chem. C* **2009**, *113*, 21155-21161.

(5) Chen, X.; Allen, H. C. *J. Phys. Chem. B* **2010**, *114*, 14983-14988.

(6) Casford, M. T. L.; Davies, P. B.; Neivandt, D. J. *Langmuir* **2006**, *22*, 3105-3111.

(7) Hayes, P. L.; Keeley, A. R.; Geiger, F. M. *J. Phys. Chem. B* **2010**, *114*, 4495-502.

(8) Conboy, J. C.; Messmer, M. C.; Richmond, G. L. *J. Phys. Chem. B* **1997**, *101*, 6724-6733.

(9) Conboy, J. C.; Messmer, M. C.; Richmond, G. L. *Langmuir* **1998**, *14*, 6722-6727.

(10) Chen, X.; Wang, J.; Sniadecki, J. J.; Even, M. A.; Chen, Z. *Langmuir* **2005**, *21*, 2662-2664.

(11) Wang, J.; Lee, S.-H.; Chen, Z. *J. Phys. Chem. B* **2008**, *112*, 2281-2290.

(12) Phillips, D. C.; York, R. L.; Mermut, O.; McCrea, K. R.; Ward, R. S.; Somorjai, G. A. *J. Phys. Chem. C* **2007**, *111*, 255-261.

(13) Fu, L.; Liu, J.; Yan, E. C. Y. *J. Am. Chem. Soc.* **2011**, ACS Just Accepted.

(14) Liu, J.; Conboy, J. C. *Langmuir* **2005**, *21*, 9091-9097.

(15) Kett, P. J. N.; Casford, M. T. L.; Davies, P. B. *Langmuir* **2010**, *26*, 9710-9719.

(16) Wang, T.; Li, D.; Lu, X.; Khmaladze, A.; Han, X.; Ye, S.; Yang, P.; Xue, G.; He, N.; Chen, Z. *J. Phys. Chem. C* **2011**, *115*, 7613-7620.

(17) Kriech, M. A.; Conboy, J. C. *J. Opt. Soc. Am. B: Optical Physics* **2004**, *21*, 1013-1022.

CHAPTER 5

DETECTION OF DRUG-LIPID MEMBRANE INTERACTIONS WITH UV-VIS SUM-FREQUENCY GENERATION

5.1 Introduction

In Chapter 4, the development of UV-Vis SFG was presented where the SFG wavelength is in the deep UV (194-237 nm), allowing $\pi \rightarrow \pi^*$ and $n \rightarrow \pi^*$ electronic transitions to be probed in a variety of biological species such as aromatic amino acids, peptides, proteins and aromatic/double bond containing drugs. The application of UV-Vis SFG for a direct detection of drug associations into lipid membranes is described in this chapter.

Drug-membrane interactions play a crucial role in the pharmacology and activity of drugs.[1-3] The equilibrium of a drug molecule between plasma and the cellular membrane has conventionally been characterized by bulk phase partitioning, usually between water and 1-octanol, which is used to mimic the lipid membrane.[4-7] However, the bulk thermodynamic properties of a homogenous liquid phase, i.e., 1-octanol, cannot accurately model the thermodynamics of a lipid membrane, which is comprised of an approximately 50 Å thick lipid bilayer. Additionally, the membrane, composed of various phospholipids, proteins and cholesterol, is best described as a finite interfacial region with a very high surface-to-volume ratio and a limited number of binding sites.[8,9] For this

reason, solution phase liposome based assays have been developed to more accurately model and study drug-membrane association.[10-13]

Spectroscopic methods for detecting drug-membrane interaction such as UV-Vis absorbance spectroscopy,[14,15] fluorescence,[13,16-18] IR,[19-21] Raman,[22,23] NMR[24-26] and ESR[27-29] have all been utilized to measure drug interactions with solution phase vesicles. Such techniques require large quantities of drug and lipid, and usually involve a separation step to remove unbound drug from the solution prior to analysis. These requirements are necessary due to the limited sensitivity of the spectroscopic methods employed.

The use of planar supported lipid bilayers (PSLBs) for measuring drug-membrane association has several advantages over solution phase vesicles, including the use of smaller solution volumes, elimination of the separation steps employed in liposome-based assays, and in principle, ability to integrate into a high-throughput assay. However, in order to fully exploit the potential benefits of a PSLB assay, what is needed is a detection method with high sensitivity, a low limit of detection and the capability of measuring drug-membrane interactions at the interfacial level without interference from solution phase species.

Several possible methods could be employed to measure drug-membrane interactions on surfaces. Surface enhancement vibrational techniques such as attenuated total reflection (ATR) IR[30] and surface enhanced Raman scattering (SERS)[31] are sensitive spectroscopic methods but they suffer from spectral congestion and the inability to selectively isolate the resonances of the drug molecule from the surrounding lipid matrix. Raman scattering incorporated with confocal microscopy has also been used in detection

of drug-liposome interactions.[32,33] The confocal microscopy allows Raman scattering from individual lipid vesicles to be detected, eliminating the contribution from the lipid matrix. The technique, however, requires a high laser power and long integration time as the Raman scattering signal is intrinsically weak.[34] Total internal reflection fluorescence is an extremely sensitive method, capable of single molecule detection limit. However, if the drug molecule of interest lacks any intrinsic fluorescence, an extrinsic fluorescent tag must be covalently attached to the molecule for detection.

In this chapter, the use of a novel deep UV spectroscopic method, ultraviolet-visible sum-frequency generation (UV-Vis SFG), has been implemented to directly detect drug association to lipid membranes without the need for chemical modification. As described in Chapter 4, an increase in the UV-Vis SFG signal will be observed when the incident or SFG frequency is resonant with electronic transitions of the molecules presenting at the interface. In this way UV-Vis SFG has the spectral characteristics of UV-Vis absorbance spectroscopy but with higher sensitivity and surface specificity.

To demonstrate the ability of UV-Vis SFG to detect drug association to a membrane, four drugs were examined: ibuprofen, azithromycin, tolnaftate and tetracaine. The chemical structure of these compounds and their associated UV-Vis spectra are shown in Figure 5.1 and 5.2, respectively. These drugs were chosen as they belong to four important classes of known membrane associated drug compounds:[21,35-37] non-steroidal anti-inflammatory drugs (NSAIDs), antibiotics, antifungals and anesthetics. Ibuprofen, tolnaftate and tetracaine all contain a π-conjugated ring system in their structures, resulting in strong electronic transitions in the UV as shown in Figure 5.2. Azithromycin was chosen as it possesses only a single carbonyl bond, giving rise to a

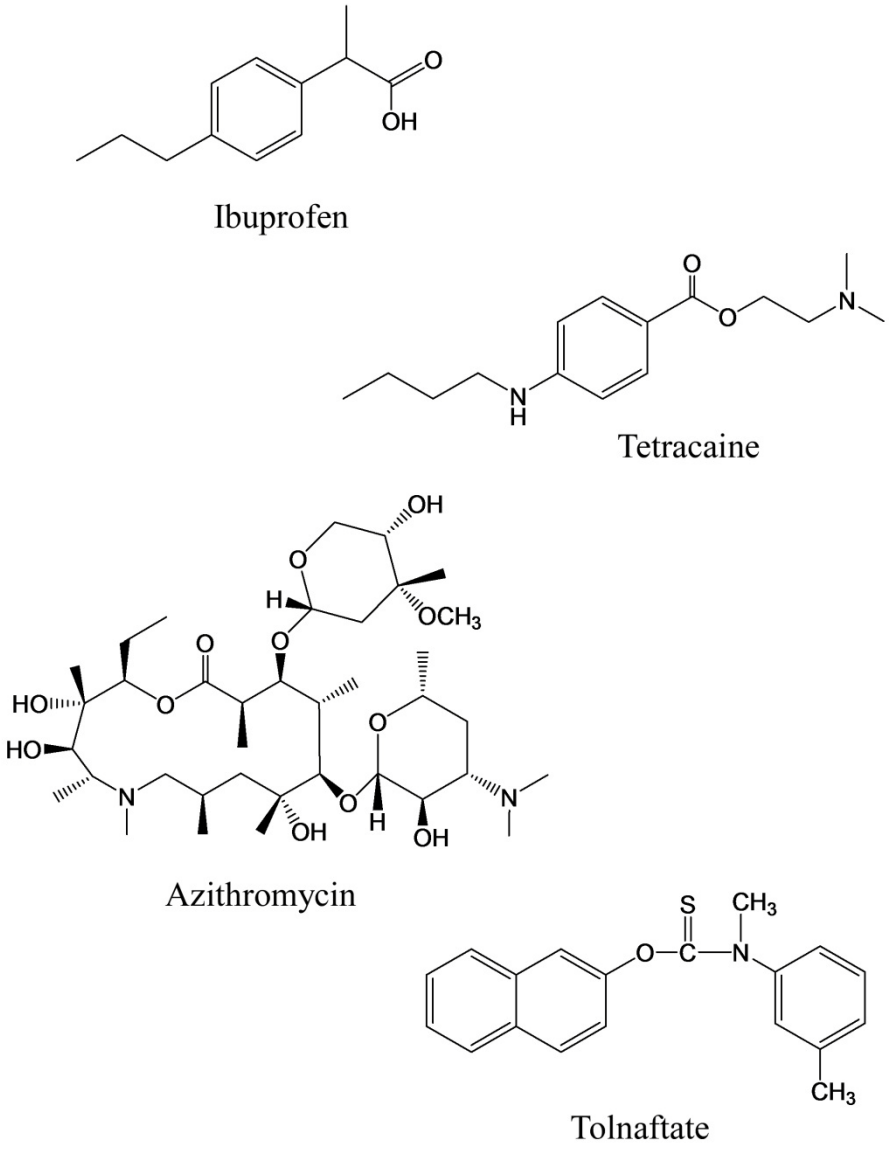

Figure 5.1 Molecular structures of ibuprofen, tetracaine, azithromycin and tolnaftate.

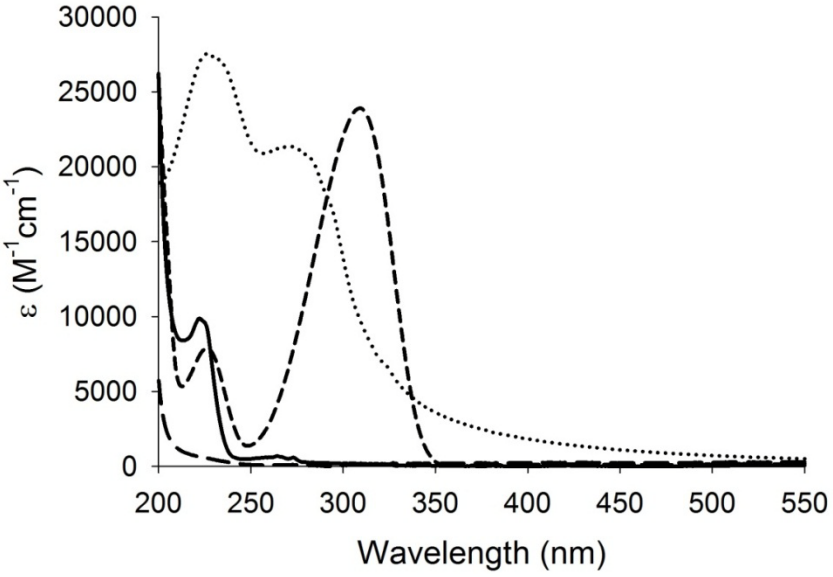

Figure 5.2 Extinction coefficient spectra of ibuprofen (solid), tetracaine (short dash), azithromycin (long dash) and tolnaftate (dotted).

small absorbance at the deep UV (< 220 nm), which makes it a significantly weaker absorber compared to the other drugs examined.

5.2 Experimental

5.2.1 Materials

1,2-dioleoyl-*sn*-glycero-3-phosphocholine (DOPC) was obtained from Avanti Lipids and was used as received. Ibuprofen, tetracaine, azithromycin and tolnaftate were purchased from Sigma Aldrich. All water used in the experiments was obtained from Nanopure^{TM} Infinity Ultrapure water system with a minimum resistivity of 18.2 MΩ-cm. Phosphate buffered saline (PBS) was made from $Na_2HPO_4 \cdot 7H_20$ and NaCl at a concentration of 50 mM and 100 mM, respectively, in water. The PBS buffer was adjusted to a pH of 7.5 using NaOH. The drugs were dissolved in PBS pH 7.5 to the desired working concentration.

The substrates used for the preparation of the PSLBs and the UV-Vis SFG experiments consisted of custom manufactured full spectrum grade (IR/UV) fused silica prisms (Almaz Optics). The prism was mounted onto a custom built Teflon flowcell. The prisms were cleaned by immersion in a solution of 70 % sulfuric acid and 30 % hydrogen peroxide overnight. Prior to use, the prisms were rinsed with water and cleaned with an Ar plasma (Harrick Scientific Plasma Cleaner/Sterilizer) for 3 minutes. Following the plasma cleaning procedure, the prisms were rinsed thoroughly with Nanopure water.

5.2.2 Small Unilamellar Vesicle (SUV) Preparation

A 1 mg/ml solution of DOPC in chloroform was evaporated under a stream of $N_2(g)$ and vacuum dried overnight to remove residual chloroform. The dried lipids were suspended in PBS pH 7.5 to a concentration of 0.5 mg/mL by vortexing followed by bath

sonication for 10 - 30 minutes to clarify. The prism used as PSLBs substrate was mounted on a flowcell (described in the following section). PSLBs were formed on the silica prism by vesicle fusion, which involved incubating the surface with the SUV solution for 30 minutes. The flowcell was then flushed with PBS pH 7.5 to remove any free lipid solution.

5.2.3 UV-Vis SFG Setup

The 532 nm (2^{nd} harmonic) and 355 nm (3^{rd} harmonic) beams from a Nd:YAG laser (Continuum, Surelite II, 20 Hz) with a diameter of 3 mm and energies of 12 and 14 mJ/pulse, respectively, were used for the UV-Vis SFG experiments. The Vis and UV beams (both at *mixed* polarization, $\gamma = 45^{o}$) were incident on the surface in a counter-propagating geometry, with each beam striking the silica/water interface at an angle slightly greater than the critical angle, which is approximately 67^{o}. The UV and Vis were spatially and temporally combined at PSLBs of DOPC which was deposited on a fused silica trapezoidal prism, to generate a SFG beam at 213 nm. A schematic of the optical arrangement is shown in Figure 5.3. Optical filters were placed in the path of the emitted SFG light to remove any scattered UV and Vis light. Spectroscopic detection was accomplished with a photomultiplier tube and the signal processed with a boxcar integrator.

5.2.4 Equilibrium Binding of Drugs to PSLBs

The SHG intensity was measured at various bulk concentrations of drugs, increasing from low to high. At each concentration, the SFG was recorded until a steady-state response was achieved. The SFG intensity was plotted versus the bulk drug concentration.

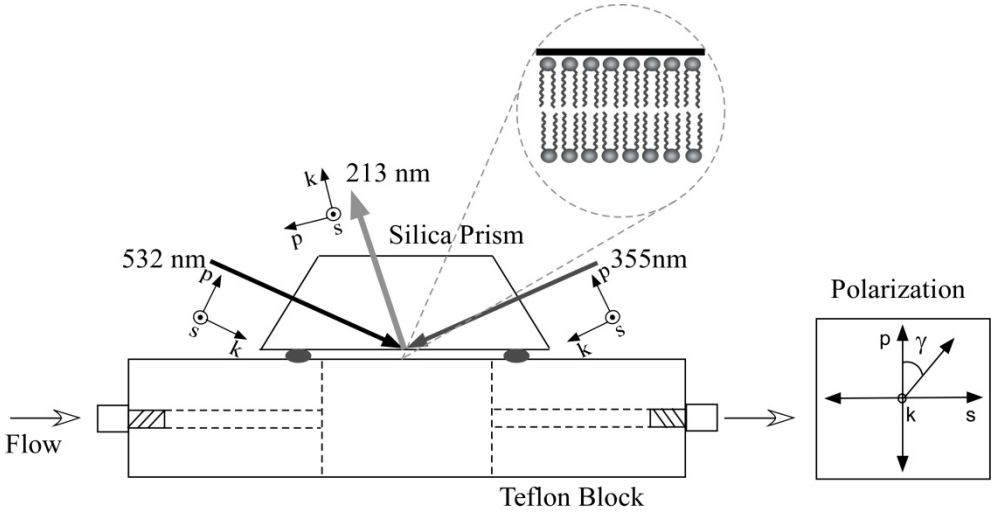

Figure 5.3 UV-Vis SFG cell showing the geometric arrangement of the UV, Vis and SFG beams. Also shown is representation of the polarization state of the incident and output fields denoted as the angle γ with respect to the propagation direction (*k*).

As described in equations 4.6a-b and 4.11 in Chapter 4, the SFG intensity (I_{SFG}) is proportional to N^2 which is the surface density squared; therefore, the Langmuir isotherm used to fit the SFG intensity is expressed as:

$$\frac{I_{SFG}}{I_{SFG}^{Max}} = \left(\frac{KaC}{1 + KaC}\right)^2, \tag{5.1}$$

where I_{SFG} is the measured SFG intensity as a function of the bulk tetracaine concentration C, K_a is the equilibrium association constant and I_{SFG}^{Max} is the maximum SFG intensity at surface saturation.

The Frumkin model takes account into the electrostatic interaction between charged molecules, which is given by:

$$\frac{I_{SFG}}{I_{SFG}^{Max}} = \left(\frac{K_a C \exp\left(2g\sqrt{I_{\mathrm{SFG}}}/RT\right)}{1 + K_a C \exp\left(2g\sqrt{I_{\mathrm{SFG}}}/RT\right)}\right)^2, \tag{5.2}$$

when $g > 0$, the interaction between the adsorbed molecules is attractive while a repulsive interaction is represented by $g < 0$. When $g = 0$, the Frumkin model becomes the Langmuir model. A statistical evaluation (F-test) was performed using SigmaPlot with a confidence level of 95% to determine the most appropriate model to be applied to the data.

5.2.5 Extrapolation of Partition Coefficients of Azithromycin and Tolnaftate for Liposome Membrane-Water System

The partition coefficients of charged azithromycin and neutral tolnaftate for the liposome membrane-water system are not available in the literature. Thus, these values were obtained by extrapolating the known partition coefficients of several drugs (see

Tables 5.1, 5.2 and Figures 5.4, 5.5) which were available in the literature[7] in both the octanol-water and liposome membrane-water systems. Using a value of $\log P^{i}_{oct} = 0.23$ for azithromycin and a value of $\log P^{N}_{oct} = 5.40$ for tolnaftate,[38] the extrapolated $\log P^{i}_{mem}$ and $\log P^{N}_{mem}$ were calculated as 2.12 and 5.17. These values are those which appear in Table 5.4 in the results and discussion section.

5.3 Results and Discussion

5.3.1 Association of Drugs into a DOPC Bilayer

The adsorption isotherms for ibuprofen, tetracaine, azithromycin and tolnaftate are presented in Figures 5.6, 5.7, 5.8 and 5.9. The results from a nonlinear least-square regression of the data in Figures 5.6-5.9, to equation 5.1 (Langmuir isotherm) or 5.2 (Frumkin isotherm), are listed in Table 5.3. It was found that the Langmuir isotherm fit best to ibuprofen ($F = 2.15$, $P = 0.22$) and tolnafate ($F = 2.07$, $P = 0.21$) binding data whereas the Frumkin isotherm provides a better fit to tetracaine ($F = 545$, $P = 0.00$) and azithromycin ($F = 8.39$, $P = 0.04$) binding data.

The affinity constants, K_a, for the drugs examined here were found to increase in the order ibuprofen < tetracaine < azithromycin < tolnaftate. The order in the affinity constants measured by the UV-Vis SFG agrees with the order of the partition coefficient of the studied drugs in the liposome-water system (P^{i}_{mem}) listed in Table 5.4. In particular, a positive correlation was observed between the free energy of adsorption ($\Delta G_{ads} = -RTlnK_a$) and the free energy of transfer from water to liposome-membrane ($\Delta G_{trans} = -RTlnP^{i}_{mem}$) for each drug (see Table 5.4). This observation is not surprising as the main driving force for drug-membrane association and partitioning between water and

Table 5.1 Logarithm of partition coefficients of six ionized drugs in octanol-water and liposome membrane-water systems.

Drug	$\log P^{i}_{oct}$	$\log P^{i}_{mem}$
Ibuprofen	- 0.05	1.81
Dichlofenac	0.69	2.64
Warfarin	- 0.46	1.38
Lidocaine	- 0.53	1.22
Tetracaine	0.22	2.11
Procaine	- 0.81	0.76

Table 5.2 Logarithm of partition coefficients of five neutral drugs in octanol-water and liposome membrane-water systems.

Drug	$\log P^{N}_{oct}$	$\log P^{N}_{mem}$
Ibuprofen	3.97	3.80
Dichlofenac	4.51	4.45
Metoprolol[38]	1.95	2.00
Lidocaine	2.45	2.39
Tetracaine	3.51	3.23

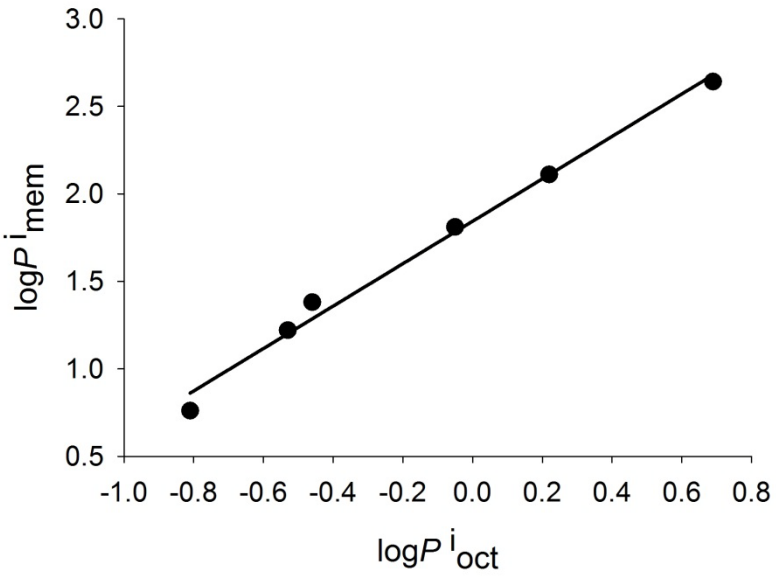

Figure 5.4 Correlation between $\log P^{i}_{mem}$ and $\log P^{i}_{oct}$ for six different drugs, listed in Table 5.1.

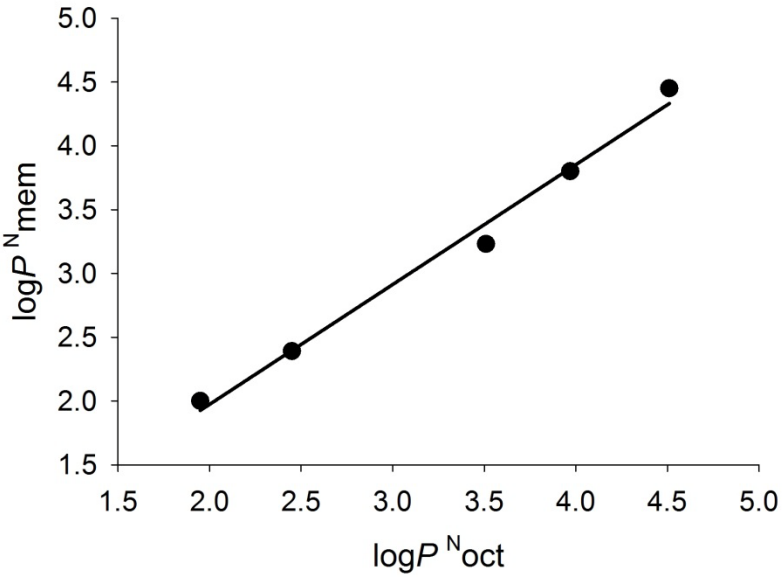

Figure 5.5 Correlation between $\log P^{N}_{mem}$ and $\log P^{N}_{oct}$ for five different drugs, listed in Table 5.2.

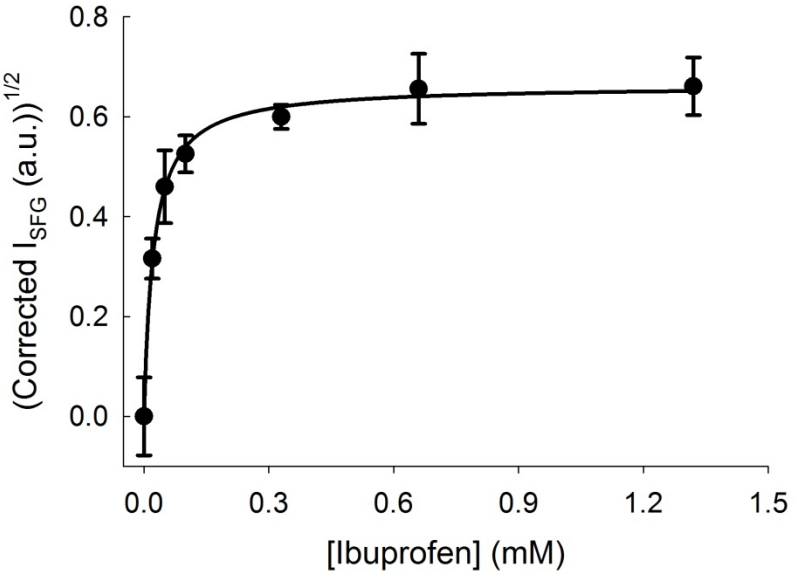

Figure 5.6 Corrected square-root of UV-Vis SFG intensity vs. bulk ibuprofen concentration. The solid line is the fit to the Langmuir isotherm. The error bars represent the standard deviation from three independent experiments.

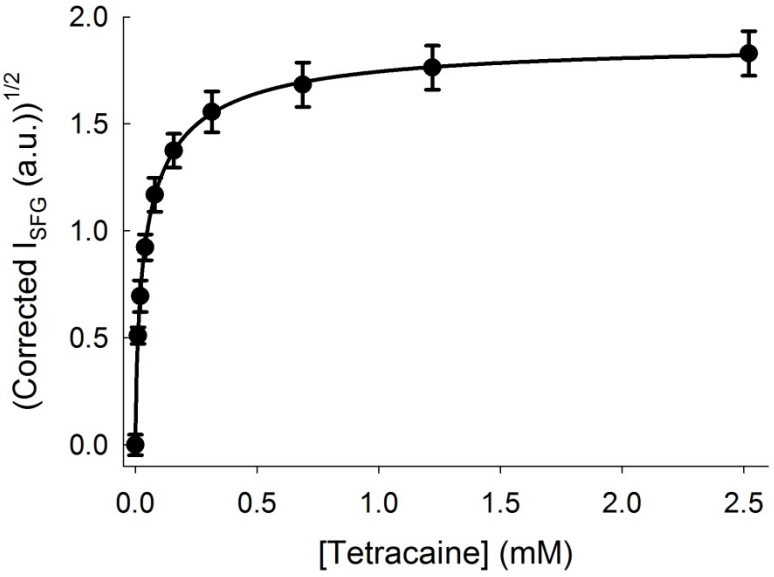

Figure 5.7 Corrected square-root of UV-Vis SFG intensity vs. bulk tetracaine concentration. The solid line is the fit to the Frumkin isotherm. The error bars represent the standard deviation from three independent experiments.

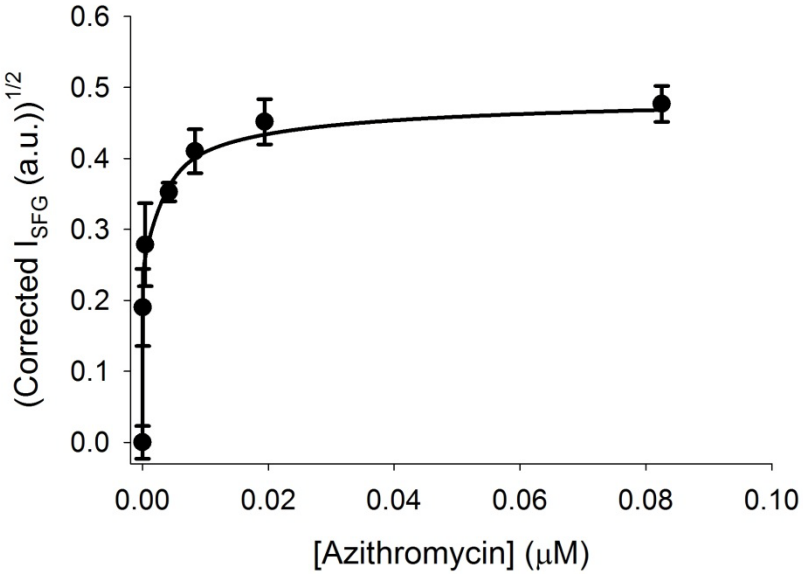

Figure 5.8 Corrected square-root of UV-Vis SFG intensity vs. bulk azithromycin concentration. The solid line is the fit to the Frumkin isotherm. The error bars represent the standard deviation from three independent experiments.

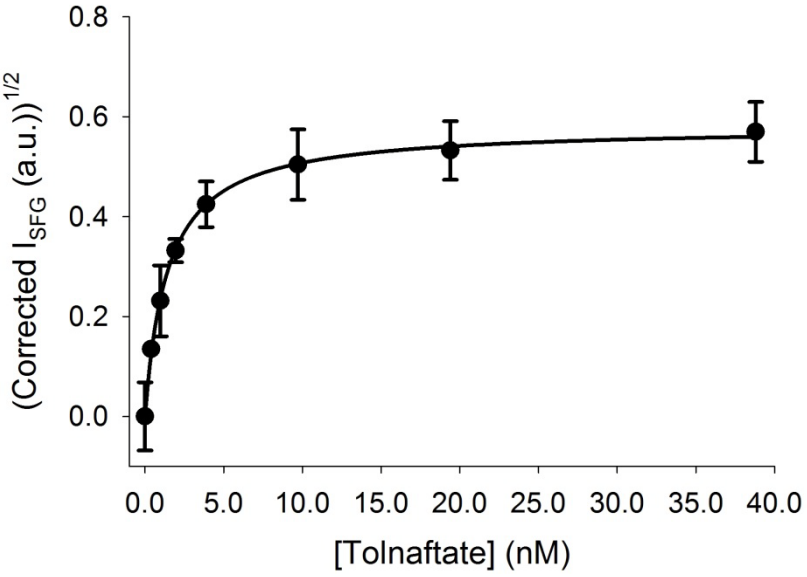

Figure 5.9 Corrected square-root of UV-Vis SFG intensity vs. bulk tolnaftate concentration. The solid line is the fit to the Langmuir isotherm. The error bars represent the standard deviation from three independent experiments.

Table 5.3 Measured equilibrium association constant, square-root of maximum SFG intensity at surface saturation, and g values for various drugs.

Drug	K_a (M^{-1})	$\sqrt{I_{SFG}^{Max}}$ (a.u.)	g
Ibuprofen	$(4.37 \pm 0.33) \times 10^4$	0.66 ± 0.09	
Tetracaine	$(5.14 \pm 0.01) \times 10^4$	1.88 ± 0.01	$- 1.51 \pm 0.06$
Azithromycin	$(1.25 \pm 0.09) \times 10^8$	0.49 ± 0.05	$- 6.51 \pm 2.19$
Tolnaftate	$(7.00 \pm 0.26) \times 10^8$	0.58 ± 0.02	

Table 5.4 Partition coefficient in membrane-water system, transfer free energy, and adsorption free energy for various drugs.

Drug	$\log P^{i}_{mem}$	ΔG_{trans} (kJ/mol)	ΔG_{ads} (kJ/mol)
Ibuprofen	1.81	- 10.3	- 26.5
Tetracaine	2.11	- 12.0	- 26.9
Azithromycin	2.12*	- 12.1	- 46.2
Tolnaftate	5.17*	- 29.5	- 50.5

*extrapolated values described in section 5.2.5

liposome-membrane is the hydrophobicity of the drug compounds. It is important to note that the correlation is clearly not linear which points to the underling difficulties of obtaining drug-membrane binding affinities from equilibrium bulk partitioning data. In order to obtain binding affinities from bulk partition measurements, knowledge of the molar free-volumes of the solute and matrix is required.[28] Additionally, binding saturation is never achieved in the bulk partition measurements due to the nature of the bulk phase with unlimited number of binding sites. The fact that UV-Vis SFG is able to obtain this information in a straightforward manner is therefore advantageous.

The obtained negative value of g for tetracaine and azithromycin illustrates the repulsive interactions between the charged drug molecules. At pH 7.5, tetracaine and azithromycin are both primarily positive charged while ibuprofen possesses one negative charge. However the Langmuir model provides a better fit to the adsorption data of ibuprofen, presumably due to the electrostatic shielding from the supporting electrolytes. This behavior was not observed for tetracaine and azithromycin, suggesting the electrostatic shielding could be more significant for ibuprofen. It has been reported that ionized ibuprofen (weak acid) locates closer to the membrane-water interface while the ionized tetracaine and azithromycin (weak bases) associate more strongly into the hydrophobic tails of the lipid membrane.[39] Therefore, in order to screen the electrostatic interactions between the ionized tetracaine and azithromycin molecules, electrolyte species from the bulk phase have to move deeper into the membrane, which is not an energetically favorable process.[39] The absence of any electrostatic repulsion is clearly seen for tolnaftate, which is the only neutral drug in this study and is best fit with a Langmuir isotherm ($g = 0$).

5.3.2 Calculation of Surface Excess of Drugs in a DOPC Bilayer

In addition to retrieving information on the thermodynamics of drug-membrane association, the ability of UV-Vis SFG to obtain information about the surface excess of the drug Γ_{max} in the membrane is also possible. As with other spectroscopic methods, the UV-Vis SFG response as a function of surface concentration needs to be calibrated. This could be achieved by using lipid membranes which have fixed and known concentrations of drug in the membrane and measuring the UV-Vis SFG response. As the drug-membrane association is a dynamic equilibrium process, it is not possible to create such standards easily. However, data do exist, in the form of partition coefficients for the drugs in liposome-membrane systems or octanol-water partitioning data,[7] which can be used to calibrate the UV-Vis SFG data. In the linear region of the binding isotherms, i.e., at low surface density, the partitioning of the drug in the membrane is identical to that in a bulk liquid phase as there is effectively no competition for binding sites.[40] Using the linear regions of the isotherms shown in Figures 5.6-5.9, the UV-Vis SFG intensity was calibrated for each drug. The partition coefficients were used to determine the membrane concentration from the bulk aqueous concentration of the drug:

$$[Drug]_{mem} = P^{i}_{mem}[Drug]_{aqueous}\ , \tag{5.3}$$

where $[Drug]_{mem}$ and $[Drug]_{aqueous}$ are the concentrations of the drug in the membrane and aqueous phases, respectively. P^{i}_{mem} is the partition coefficient of the charged drug in the membrane. The surface concentration of the drugs in molecules (molc)/cm^2 was then determined by assuming an effective thickness of the DOPC bilayer of 50 Å.

The calculated surface excess Γ (in molc/cm^2) is plotted as a function of bulk concentration for ibuprofen, tetracaine, azithromycin and tolnaftate in Figures 5.10, 5.11, 5.12, and 5.13, respectively. The maximum surface excess of the drugs Γ_{max} is given in Table 5.5. Although the affinity constants for the drugs are in the order ibuprofen < tetracaince < azithromycin < tolnaftate, the same cannot be said of the saturation concentration of the drugs in the membranes. Azithromycin has the lowest surface saturation, $(1.58 \pm 0.16) \times 10^{10}$ molc/cm^2 while tolnaftate is considerably larger, $(1.00 \pm 0.03) \times 10^{13}$ molc/cm^2. Ibuprofen and tetracaine have similar surface saturation values, $(0.92 - 2.08) \times 10^{12}$ molc/cm^2. The lowest maximum surface excess observed for azithromycin could be related to the lipid membrane disruption caused by azithromycin upon its interaction with the lipid membrane. It has been previously reported that azithromycin at a concentration of 50 μM was found to affect the elasticity of DOPC giant unilamellar vesicles (GUVs) by decreasing the cohesion between the DOPC molecules, resulting in a disruption of the GUVs of DOPC.[41] The μM concentration range of azithromycin used in the present study could cause the disruption of the DOPC lipid bilayer, leading to the low maximum surface excess of azithromycin.

The absence of a direct link between K_a and Γ_{max} is not surprising, as the factors determining these two quantities are not necessarily correlated. K_a is governed by the thermodynamic stability of the molecule in the membrane. However, the partition coefficient does not have any dependence on the number of binding sites, as it represents bulk equilibrium. Likewise, the value of K_a is not dependent on the absolute number of binding sites, but rather is a reflection of the fraction of surface occupancy at a specific bulk concentration; which is why knowledge of the affinity constant alone is not

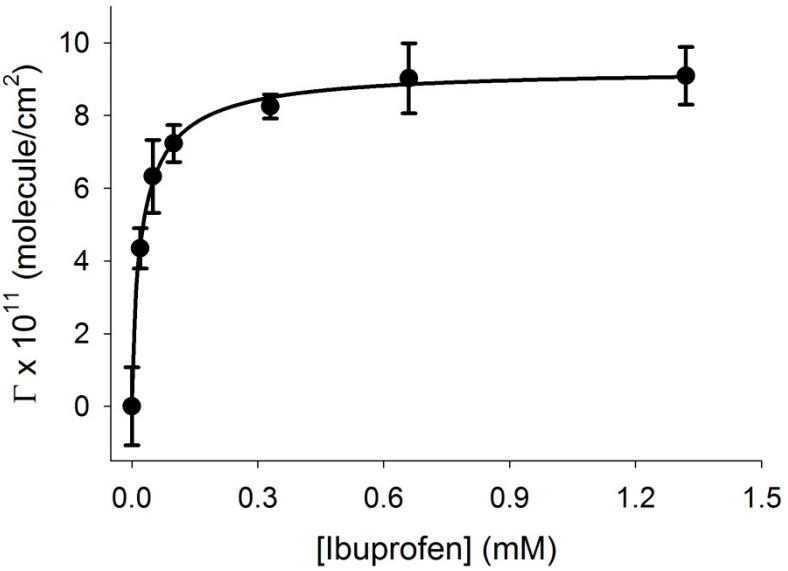

Figure 5.10 Surface excesses Γ vs. bulk concentration of ibuprofen. The solid line is the fit to the data using the Langmuir isotherm. The error bars represent the standard deviation from three independent experiments.

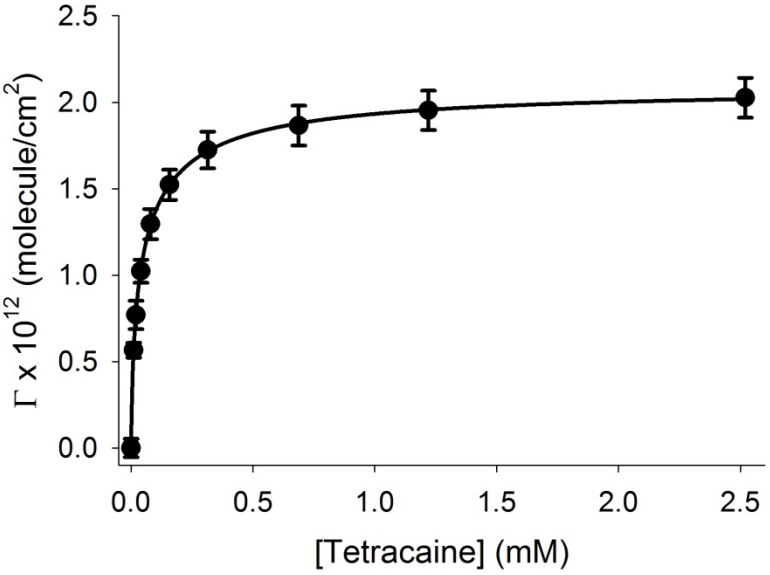

Figure 5.11 Surface excesses Γ vs. bulk concentration of tetracaine. The solid line is the fit to the data using the Frumkin isotherm. The error bars represent the standard deviation from three independent experiments.

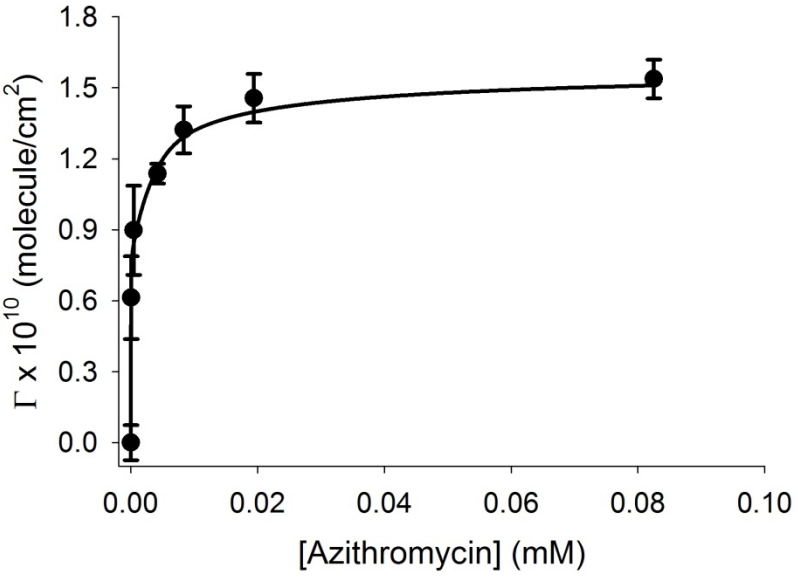

Figure 5.12 Surface excesses Γ vs. bulk concentration of azithomycin. The solid line is the fit to the data using the Frumkin isotherm. The error bars represent the standard deviation from three independent experiments.

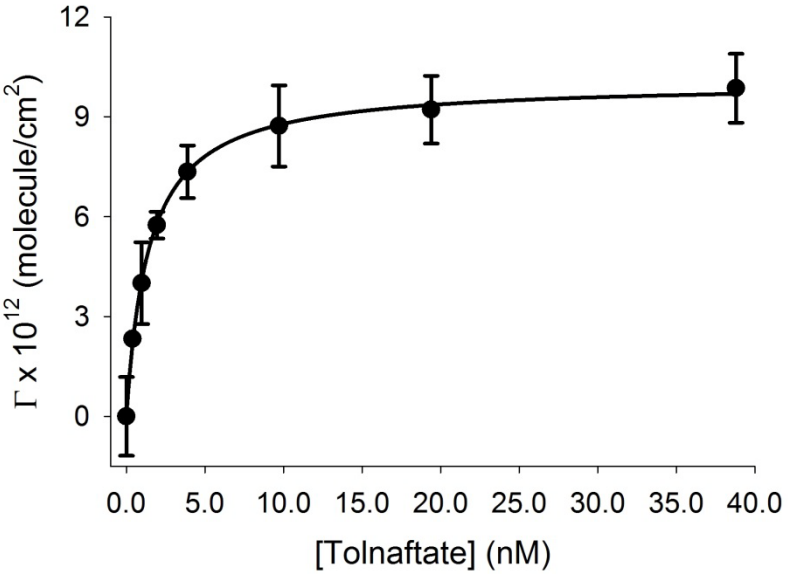

Figure 5.13 Surface excesses Γ vs. bulk concentration of tolnaftate. The solid line is the fit to the data using the Langmuir isotherm. The error bars represent the standard deviation from three independent experiments.

Table 5.5 Maximum surface excess and limit of detection for various drugs.

Drug	Γ_{max} (molecule/cm^2)	*LOD* (pg/cm^2)
Ibuprofen	$(9.22 \pm 0.14) \times 10^{11}$	46.9 ± 4.7
Tetracaine	$(2.08 \pm 0.01) \times 10^{12}$	116.7 ± 10.9
Azithromycin	$(1.58 \pm 0.16) \times 10^{10}$	3.6 ± 0.3
Tolnaftate	$(1.00 \pm 0.03) \times 10^{13}$	1306.8 ± 52.8

sufficient to determine the absolute number of molecules bound to the membrane. A quantitative determination of drug saturation in the membrane is possible when both the data from bulk phase equilibrium measurements and UV-Vis SFG are used in combination, with the use of PSLBs, as demonstrated here.

A quantitative assessment of the limit of detection (*LOD*) of UV-Vis SFG can also be made. Using the spectroscopic sensitivity determined from the calibration of the UV-Vis SFG intensity and the standard deviation in the measured signal, the detection limits for the three drugs examined were calculated by:

$$LOD = \frac{3\sigma}{sensitivity} \tag{5.4}$$

where σ is the average standard deviation from the background signals (in the absence of the drugs). The *sensitivity* in equation 5.4 was obtained from the calibrated SHG intensity. The calculated values of *LOD* are listed in Table 5.5. The lowest calculated *LOD* is 3.6 ± 0.3 pg/cm^2 for azithromycin with the highest observed for tolnaftate at 1.31 ± 0.05 ng/cm^2. The lowest calculated *LOD* obtained for azithromycin could be related to the highly ordered orientation of azithromycin in the DOPC lipid bilayer. The protonated form of azithromycin was found to penetrate into a monolayer of the negatively charged phosphatidylinositol lipid with the drug's desoamine group inserting into the hydrophobic cores of the lipid monolayer and the endocyclic tertiary amine staying closer to the negatively charged phosphate of the lipid head group.[42] Another factor that could also contribute to the low calculated *LOD* of azithromycin is the larger asymmetry of the drug molecule as compared to the other drugs used in the study, which enables the detection of azithromycin to be done more easily.

These detection limits are far superior to the other surface specific and label-free method, SPR, and are comparable to fluorescence measurements but without a label being needed and with reduced photo-degradation. The impressive *LOD* and the surface specificity of UV-Vis SFG illustrate the potential application of the method for measuring low-molecular weight drug-membrane interactions.

5.3.3 Effect of Electrolyte Concentration on Drug Binding to a DOPC Bilayer

In order to verify the repulsive interaction between the charged drug molecules, the UV-Vis SFG measurements were performed at two different salt concentrations of PBS for ibuprofen: 150 mM (100 mM NaCl + 50 mM Na_2HPO_4) and 15 mM (10 mM NaCl + 5 mM Na_2HPO_4). The adsorption isotherms for ibuprofen at these two salt concentrations are shown in Figure 5.14. The equilibrium association affinity K_a, g and square-root of the maximum intensity, $\sqrt{I_{SFG}^{Max}}$ obtained are listed in Table 5.6.

As seen in Figure 5.14 and Table 5.6, the electrolyte concentration does not significantly affect the equilibrium association affinity of ibuprofen to DOPC bilayer. However, the electrostatic repulsion between the charged ibuprofen molecules is observed at low electrolyte concentration as demonstrated by negative value of g (-2.36 ± 0.67). This is due to the increase in the Debye length at low electrolyte concentration (15 mM PBS) or a decrease in the shielding strength, resulting in more repulsion between the charged ibuprofen molecules. Accordingly, the maximum surface excess, Γ^{max}, for ibuprofen decreases (lower value of $\sqrt{I_{SFG}^{Max}}$) at the lower electrolyte concentration.

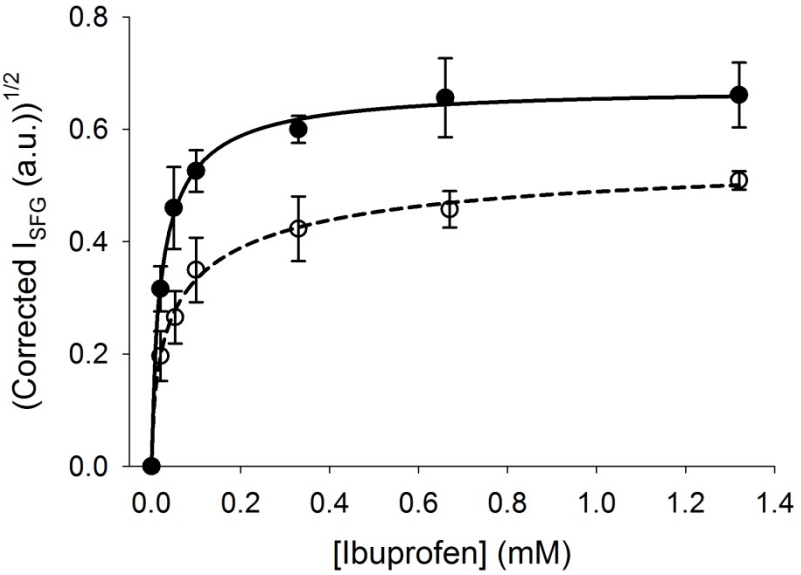

Figure 5.14 UV-Vis SFG isotherms for ibuprofen binding to a DOPC lipid bilayer in 150 mM PBS (filled circles) and at 15 mM PBS (open circles). The lines are the fits to the data using the Langmuir isotherm (solid) and Frumkin isotherm (dash). The error bars represent the standard deviation from three independent experiments.

Table 5.6 Measured equilibrium association constant, square-root of maximum SFG intensity at surface saturation, and g values for ibuprofen at different electrolyte concentrations.

Electrolyte concentration	$K_a \times 10^4$ (M^{-1})	$\sqrt{I_{SFG}^{Max}}$ (a.u.)	g
100 mM NaCl + 50 mM Na_2HPO_4	4.37 ± 0.33	0.66 ± 0.09	
10 mM NaCl + 5 mM Na_2HPO_4	6.27 ± 1.43	0.55 ± 0.03	-2.36 ± 0.6

5.4 Summary

The detection of drug-lipid membrane association was directly achieved using UV-Vis SFG spectroscopy without chemical modification. The equilibrium association constants of ibuprofen, azithromycin, tolnaftate and tetracaine into a lipid membrane have been measured for the first time and have been shown to correlate with the drugs' hydrophobicity. The concentration of the drugs in the lipid membrane was quantitatively obtained using the knowledge of bulk partition coefficients in combination with the UV-Vis SFG measurements. The electrostatic repulsion between the charged ibuprofen became obvious when low electrolyte concentration was used. The detection limit of the technique of pg/cm^2 and the surface specificity of UV-Vis SFG suggest that UV-Vis SFG is a valuable alternative in measuring the association of drugs to the membranes.

5.5 References

(1) Seydel, J. K. *Methods and Principles in Medicinal Chemistry* **2002**, *15*, 217-289.

(2) Mingeot-Leclercq, M. P. *Drug-Membrane Interactions Analysis, Drug Distribution, Modelling Edited by J. K. Seydel and M. Wiese* **2004**, *Vol.5*.

(3) Triggle, D. J. *Drug-Membrane Interactions. Analysis, Drug Distribution, Modeling. Methods and Principles in Medicinal Chemistry, Volume 15, by J. K. Seydel and M. Wiese* **2003**, *Vol.46*.

(4) Bouchard, G.; Galland, A.; Carrupt, P.-A.; Gulaboski, R.; Mirceski, V.; Scholz, F.; Girault, H. H. *Phys. Chem. Chem. Phys.* **2003**, *5*, 3748-3751.

(5) Avdeef, A. *J. Pharm. Sci.* **1993**, *82*, 183-190.

(6) Boudeville, P.; Bona, M.; Burgot, J.-L. *J. Pharm. Sci.* **1996**, *85*, 990-998.

(7) Seydel, J. K., Wiese, M. *Drug-Membrane Interactions*; Wiley-VCH Verlag GmbH: Weinheim, 2002.

(8) Tamm, L. K.; McConnell, H. M. *Biophys. J.* **1985**, *47*, 105-113.

(9) Flaten, G. E.; Skar, M.; Luthman, K.; Brandl, M. *Eur. J. Pharm. Sci.* **2007**, *30*, 324-332.

(10) Liu, X. Y.; Yang, Q.; Kamo, N.; Miyake, J. *J. Chromatogr., A* **2001**, *913*, 123-131.

(11) Pauletti, G. M.; Wunderli-Allenspach, H. *Eur. J. Pharm. Sci.* **1994**, *1*, 273-282.

(12) Choi, Y. W.; Rogers, J. A. *Pharm. Res.* **1990**, *7*, 508-512.

(13) Vazquez, J. L.; Montero, M. T.; Trias, J.; Hernandez-Borrell, J. *Int. J. Pharm.* **1998**, *171*, 75-86.

(14) Custodio, J. B.; Almeida, L. M.; Madeira, V. M. *Biochem. Biophys. Res. Commun.* **1991**, *176*, 1079-1085.

(15) Du, L.; Liu, X.; Huang, W.; Wang, E. *Electrochimica Acta* **2006**, *51*, 5754-5760.

(16) Barghouthi, S.; Eftink, M. R. *Proc. SPIE-Int. Soc. Opt. Eng.* **1992**, *1640*, 632-636.

(17) Barghouthi, S.; Eftink, M. R. *Biophys. Chem.* **1993**, *46*, 13-19.

(18) Suwalsky, M.; Schneider, C.; Villena, F.; Norris, B.; Cardenas, H.; Cuevas, F.; Sotomayor, C. P. *Biophys. Chem.* **2004**, *109*, 189-199.

(19) Auger, M.; Smith, I. C. P.; Mantsch, H. H.; Wong, P. T. T. *Biochemistry* **1990**, *29*, 2008-2015.

(20) Casal, H. L.; Martin, A.; Mantsch, H. H. *Chem. Phys. Lipids* **1987**, *43*, 47-53.

(21) Auger, M.; Jarrell, H. C.; Smith, I. C.; Siminovitch, D. J.; Mantsch, H. H.; Wong, P. T. *Biochemistry* **1988**, *27*, 6086-6093.

(22) Kyrikou, I.; Hadjikakou, S. K.; Kovala-Demertzi, D.; Viras, K.; Mavromoustakos, T. *Chem. Phys. Lipids* **2004**, *132*, 157-169.

(23) Potamitis, C.; Chatzigeorgiou, P.; Siapi, E.; Viras, K.; Mavromoustakos, T.; Hodzic, A.; Pabst, G.; Cacho-Nerin, F.; Laggner, P.; Rappolt, M. *Biochim. Biophys. Acta, Biomembr.* **2011**, *1808*, 1753-1763.

(24) Dufourc, E. J.; Parish, E. J.; Chitrakorn, S.; Smith, I. C. P. *Biochemistry* **1984**, *23*, 6062-6071.

(25) Boulanger, Y.; Schreier, S.; Smith, I. C. *Biochemistry* **1981**, *20*, 6824-6830.

(26) De Young, L. R.; Dill, K. A. *Biochemistry* **1988**, *27*, 5281-5289.

(27) de Paula, E.; Schreier, S. *Biochim. Biophys. Acta, Biomembr.* **1995**, *1240*, 25-33.

(28) Bianconi, M. L.; do Amaral, A. T.; Schreier, S. *Biochem. Biophys. Res. Commun.* **1988**, *152*, 344-350.

(29) De Matos Alves Pinto, L.; Yokaichiya, D. K.; Fraceto, L. F.; De Paula, E. *Biophys. Chem.* **2000**, *87*, 213-223.

(30) Arkin, I. T.; Russ, W. P.; Lebendiker, M.; Schuldiner, S. *Biochemistry* **1996**, *35*, 7233-7238.

(31) Aoki, P. H. B.; Alessio, P.; De Saja, J. A.; Constantino, C. J. L. *J. Raman Spectrosc.* **2010**, *41*, 40-48.

(32) Fox, C. B.; Horton, R. A.; Harris, J. M. *Anal. Chem.* **2006**, *78*, 4918-4924.

(33) Fox, C. B.; Harris, J. M. *J. Raman Spectrosc.* **2010**, *41*, 498-507.

(34) Pawley, J. B. *Handbook of Biological Confocal Microscopy*; 3rd ed.; Spinger Science + Business Media, LCC: New York, 2006.

(35) Barbato, F.; La Rotonda, M. I.; Quaglia, F. *J. Pharm. Sci.* **1997**, *86*, 225-229.

(36) Tyteca, D.; Schanck, A.; Dufrene, Y. F.; Deleu, M.; Courtoy, P. J.; Tulkens, P. M.; Mingeot-Leclercq, M. P. *J. Membr. Biol.* **2003**, *192*, 203-215.

(37) Gupta, M. P.; Kapur, N.; Bala, I.; Khuller, G. K. *J. Med. Vet. Mycol.* **1991**, *29*, 45-52.

(38) Avdeef, A. *Absorption and Drug Development: Solubility, Permeability, and Charge State*; Wiley-Interscience: Hoboken: NJ, 2003.

(39) Avdeef, A.; Box, K. J.; Comer, J. E. A.; Hibbert, C.; Tam, K. Y. *Pharm. Res.* **1998**, *15*, 209-215.

(40) Schreier, S.; Malheiros, S. V. P.; de Paula, E. *Biochim. Biophys. Acta, Biomembr.* **2000**, *1508*, 210-234.

(41) Fa, N.; Lins, L.; Courtoy, P. J.; Dufrene, Y.; Van Der Smissen, P.; Brasseur, R.; Tyteca, D.; Mingeot-Leclercq, M. P. *Biochim. Biophys. Acta, Biomembr.* **2007**, *1768*, 1830-1838.

(42) Montenez, J.-P.; Van Bambeke, F.; Piret, J.; Schanck, A.; Brasseur, R.; Tulkens, P. M.; Mingeot-Leclercq, M.-P. *Eur. J. Pharmacol.* **1996**, *314*, 215-227.

CHAPTER 6

HIGH-THROUGHPUT SCREENING OF DRUG-LIPID MEMBRANE INTERACTIONS WITH SECOND HARMONIC GENERATION IMAGING

6.1 Introduction

In the previous chapter it was shown that the nonlinear optical spectroscopic technique, ultraviolet-visible sum frequency generation (UV-Vis SFG), is an ultrasensitive and powerful method for the detection of drug-lipid membrane interactions. The drug-lipid membrane interactions were studied with a single lipid species which was used to compose the membrane; however, biological membranes are composed of many types of phospholipids along with other small molecules, such as cholesterol. Therefore, it is also important to study the effect of lipid membrane structure and composition on drug-lipid membrane interactions. Currently, this is a time consuming and costly task which requires a large number of experiments and samples. This chapter presents the use of second harmonic generation imaging in combination with micropatterned lipid bilayer arrays which allow for a simultaneous investigation of the influence of different bilayer phase states and cholesterol content on drug binding in a high-throughput manner.

Micropatterned lipid bilayer arrays (MLBAs) are a 2D assembly of planar supported lipid bilayers (PSLBs) patterned on a surface. MLBA can be created by micro-contact printing,[1] deep ultraviolet photolithography (UV),[2] prepatterned substrates,[3] a

combination of prepatterned substrates with a robotic spotter systems,[4] and 2D and 3D microfluidics.[5,6] Among these techniques, 3D microfluidics has proven to be a promising method for making patterned planar supported lipid bilayers (PSLBs).[6] The microfluidic system delivers fluid to a discrete region on a substrate through a printhead with individually addressable microchannels within a polydimethylsiloxane (PDMS) substrate. This allows different lipid vesicle solutions to be introduced to the microchannels, thus forming an array of different PSLBs on a single substrate. The microfluidic system does not require the use of a prepatterned substrate because the PSLBs are effectively "corralled" into discrete microsized domains by the residual PDMS deposited on the substrate from the printhead. Prevention of lipid spreading can also be enhanced by introducing bovine serum albumin or polyelectrolytes after the deposition step to bind to the residual hydrophobic PDMS.[7]

Several techniques have been successfully employed to detect drug-membrane interactions including UV-Vis,[8] NMR,[9,10] vibrational spectroscopies (IR, Raman),[11,12] and fluorescence.[13,14] However, most of these methods are not suitable to study MLBAs. Vibrational spectroscopic techniques require signal enhancement such as attenuated total internal reflection (ATR) IR[15] or surface enhanced Raman scattering (SERS)[16] if they are to be used for surface detection. Intrinsic fluorescence of drug molecules can be a useful probe if present, but self-quenching can influence the response at high concentrations of the drug.[17] In the absence of intrinsic fluorescence, the covalent attachment of a fluorescent label to the drug is possible. However, such an alteration would severely change the drug's structure and more likely than not its biological activity.[18] The label-free technique of surface plasmon resonance has also been applied to detect drug-lipid

membrane binding.[19,20] In these studies, liposomes attached to a lipophilic functionalized gold surface were used as model membranes for drug binding.

Counter-propagating SHG has previously been employed to measure the association of the chiral molecules ((R)-(+)-1,1'-bi-2-naphthol (RBN) and (S)-(+)-1,1'-bi-2-naphthol (SBN)) into lipid bilayers.[21] It has also been successfully applied to image chiral RBN and SBN adsorbed to a patterned lipid bilayer.[22] In this study, SHG imaging is coupled with MLBAs to image drug-lipid membrane interactions directly for the first time in a high-throughput manner.

It has been previously discussed in Chapter 2 that an increase in SHG signal will be observed when the incident, ω, or SHG, 2ω, frequency is in resonance with an electronic transition of a molecules comprising at the interface. This can be used as an intrinsic probe to detect the presence of drug molecules in the lipid membrane if the drug has an electronic transition at the frequency of the incident or the SHG light. The SHG process, under the electric-dipole approximation, is not allowed in the bulk of the centrosymmetric medium but is allowed at a surface or interfacial region between two centrosymmetric media due to the break in symmetry of the bulk phases. This makes SHG a surface specific technique. It should be noted that the electric-quadrupole contribution from the bulk medium can contribute to the overall SHG signal.[33,34] However, its contribution can be neglected if the interfacial layer is highly symmetric[23] and/or the SHG frequency is in resonance with the electric-dipole allowed transitions of the interfacial layers.[24] In these cases, the SHG signal should be governed principally by the electric-dipole contribution from the interfacial layer. The local anesthetic tetracaine (extinction coefficient spectrum and molecular structure were shown in Chapter 5) was

chosen as a model drug in the present study. As the SHG wavelength at 266 nm is resonant with the $\pi \rightarrow \pi^*$ transition of the benzene ring of tetracaine adsorbed to a surface, the SHG intensity will be significantly enhanced, dominating over the bulk contribution.

The aim of the present work is to show that counter-propagating SHG imaging combined with MLBAs can be used as a label-free technique to visualize tetracaine-membrane interactions in a high-throughput manner. Tetracaine's anesthetic activity mainly involves blocking Na^+ influx through Na^+ channels of the nerve axonal membranes.[25] It is still unclear if the anesthetic mechanism depends on the direct interaction between the drug and its target protein or on the passive interaction between the drug and the surrounding membrane.[26-28] In an attempt to elucidate this mechanism, several extensive studies investigating tetracaine-membrane interactions have been conducted. Specifically, the effects of tetracaine on the structure and dynamics of phospholipids were studied by FTIR[29] and its effects on the phase behavior and thermodynamics of phospholipids were studied by differential scanning calorimetry.[30] The location of tetracaine in phospholipid vesicles has also been studied by fluorescence quenching and resonance energy transfer.[31] Using the intrinsic fluorescence of tetracaine, the partitioning of tetracaine into lipid membranes was measured and found to depend on the physical state and composition of the lipids.[14] Additionally, the ionization state of tetracaine was reported to affect its interaction with lipid membranes. It was found that neutral tetracaine partitions more strongly and deeply into zwitterionic phospholipids than the protonated tetracaine.[14,29] It is important to mention that these studies were performed using lipid vesicles, allowing only one lipid component to be studied in each experiment**.**

As a proof-of-principle investigation, the effects of the lipid phase state (solid-gel and liquid-crystalline) and membrane composition (saturated, unsaturated lipids, charged lipids and cholesterol content) on tetracaine binding were examined using SHG imaging. Using the MLBAs, multiple lipid membrane components with different phase states and cholesterol content were prepared on a single substrate allowing for simultaneous investigation of influence of these factors on tetracaine binding. Additionally, the binding of tetracaine in different charge states, including protonated and neutral, to the lipid bilayers were also examined. The results were found to correlate with the literature reports, validating the SHG imaging technique as a label-free and high-throughput method to detect drug-membrane interactions. Moreover, the study of tetracaine binding to the unsaturated lipids, which has not been previously published, reveals the crucial role that the phospholipid unsaturation plays in the binding affinity and surface concentration of tetracaine.

6.2 Experimental

6.2.1 Materials

1,2-dioleoyl-*sn*-glycero-3-phosphocholine (DOPC), 1,2-dimyristoyl-*sn*-glycero-3-phosphocholine (DMPC), 1,2-dipalmitoyl-*sn*-glycero-3-phosphocholine (DPPC), 1-stearoyl-2-oleoyl-*sn*-glycero-3-phosphocholine(SOPC), 1,2-dioleoyl-3-trimethylammonium-propane (DOTAP) and 1,2-dioleoyl-*sn*-glycero-3-phospho-(1'-*rac*-glycerol) (DOPG) were obtained from Avanti Lipids and used as received. Tetracaine hydrochloride, cholesterol, poly(allylamine hydrochloride) (56,000 MW) and sodium dodecyl sulfate (SDS) were purchased from Sigma Aldrich. All water used in the experiments was obtained from a Nanopure^{TM} Infinity Ultrapure water system with a resistivity of 18.2

MΩ-cm. Phosphate buffered saline (PBS) was made from $Na_2HPO_4 \cdot 7H_20$ and NaCl at a concentration of 50 mM and 100 mM, respectively, in water. The PBS buffer was adjusted to pH 7.4 using NaOH. Tetracaine hydrochloride was dissolved in PBS to working concentrations. The substrates used for the preparation of the MLBAs consisted of custom manufactured full spectrum grade (IR/UV) fused silica prisms (Almaz Optics). The prism was mounted onto a custom-built Teflon flowcell. The prisms were cleaned by immersion in a solution of 70% sulfuric acid and 30% hydrogen peroxide overnight. Prior to use, the prisms were rinsed with copious amounts of Nanopure water and cleaned with Ar plasma (Harrick Scientific Plasma Cleaner/Sterilizer, Ossining, NY) for 3 minutes.

6.2.2 Small Unilamellar Vesicle (SUV) Preparation

Stock lipid solutions in chloroform were evaporated gently under a stream of $N_2(g)$ and vacuum dried overnight to remove residual chloroform. The dried lipids were resuspended in PBS pH 7.4 at a concentration of 0.25 mg/mL by vortexing followed by bath sonication for 10 - 30 minutes until clear. The temperature during sonication was kept at least 10°C above the lipids' phase transition temperature (T_m): room temperature for DOPC, DOPG and DOTAP (T_m = - 20°C) and SOPC (T_m = 6°C), 35°C for DMPC (T_m = 24°C), and 55°C for DPPC (T_m = 41°C). The molecular structures of these lipids and cholesterol are shown in Figure 6.1.

6.2.3 MLBA Preparation

Details of the preparation of the MLBAs using the continuous flow microspotter (CFM) have been reported in detail elsewhere.[6] Briefly, up to 48 spots (each spot is 400 ×

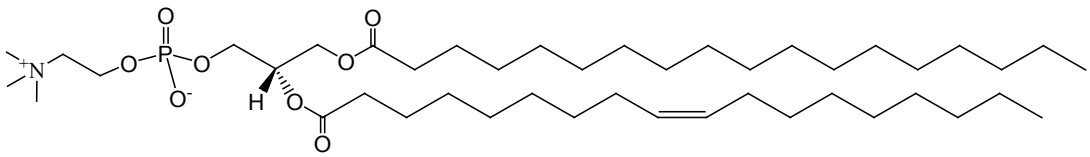

1,2-stearoyl-2-oleoyl-*sn*-glycero-3-phosphocholine (SOPC)

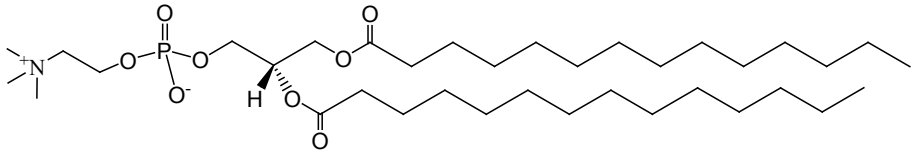

1,2-dimyristoyl-*sn*-glycero-3-phosphocholine (DMPC)

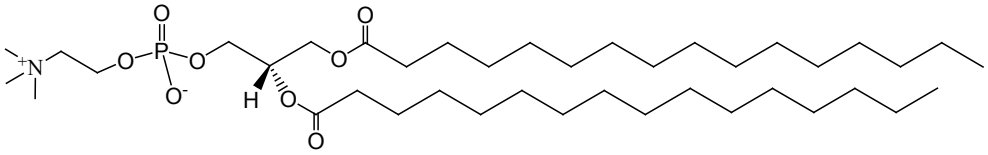

1,2-dipalmitoyl-*sn*-glycero-3-phosphocholine (DPPC)

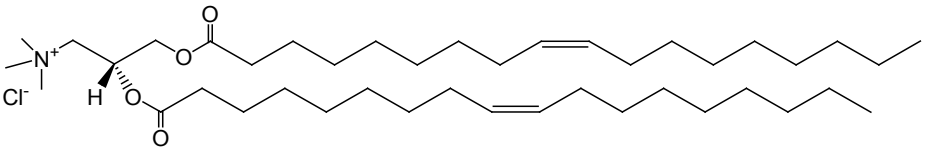

1,2-dioleoyl-3-trimethylammonium-propane (DOTAP)

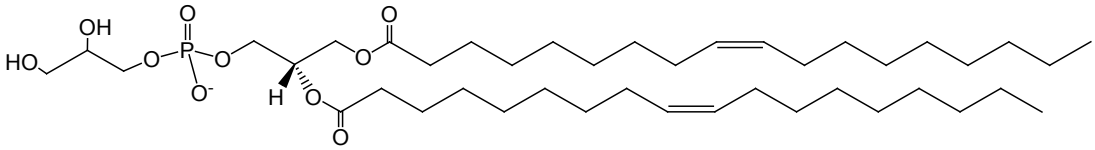

1,2-dioleoyl-*sn*-glycero-3-phospho-(1'-*rac*-glycerol) (DOPG)

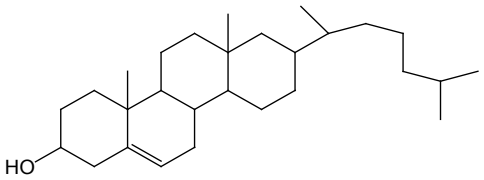

Cholesterol

Figure 6.1 Structures of the lipids and cholesterol used in the study.

400 μm^2) can be produced by the CFM. The PDMS printhead was pretreated with 1.0 mg/mL SDS in a 50:50 volume ratio of H_2O and isopropyl alcohol solution for 30 minutes and air dried. The clean prism was brought in contact with the pretreated PDMS printhead to create a pressure seal. Prior to lipid deposition, the microchannels were rinsed twice with a 50:50 solution of H_2O and isopropyl alcohol and once with Nanopure water. The 0.25 mg/mL SUV solutions were simultaneously introduced through the microchannels and allowed to circulate over the prism for at least 20 minutes. The SUVs spontaneously fused to the hydrophilic substrate, forming an array of lipid bilayers. The free vesicle solutions were removed from the channels by rinsing with Nanopure water. The prism was removed from the PDMS printhead in a reservoir containing a solution of 2 mg/mL polyallylamine in H_2O and incubated for 20 minutes. The polyallylamine adsorbs to the PDMS residue from the printhead on the prism preventing the lipids from spreading. The prism was then transferred in water to a custom-built Teflon flow cell for imaging. The temperature in the flowcell was monitored using a water bath (Haake Phoenix II, Thermo Scientific).

6.2.4 SHG Imaging

Counter-propagating SHG imaging was used in this work for the detection of the tetracaine-lipid membrane interactions. The 2nd harmonic output (532 nm) of a Nd:YAG laser (Continuum, Surelite I, 20 Hz, 7ns) with an energy of 22 mJ/pulse was directed on the surface of a quartz prism under total internal reflection. A laser beam diameter of 3.5 mm was used. The reflected beam from the surface is reflected back upon itself using a 532 nm mirror. This results in two incident beams at the same frequency arriving at the surface from opposite directions, both with an incident angle of 67° to ensure total

internal reflection. The schematic of the optical arrangement was previously shown in Chapter 3. A slight displacement of the reflected beam is introduced in order to prevent the redirected beam from entering the laser cavity.

The resulting SHG is emitted at 266 nm along the surface normal and optically filtered to remove any scattered visible light prior to imaging. Imaging of the SHG signal was achieved using a modified Olympus microscope[22] with a 3× UV objective (Optics for Research). An image intensifier (Phototek) coupled to a CCD camera (Roper Scientific, 512 × 512 pixels) was used for image acquisition. An integration time of 1200 seconds was used to collect all SHG images. SHG images were analyzed and false-color applied using the software package imageJ (http://rsbweb.nih.gov/ij/index.html). Each SHG image was first background corrected by subtracting the minimum pixel intensity from the image. The image was then flat-field corrected using the ImageJ macro available at the Integrated Microscopy Core Facility at the University of Chicago (http://digital.bsd.uchicago.edu/%5Cimagej_macros.html). The SHG images were normalized to allow for a direct comparison between the images recorded from different experiments.

6.2.5 Normalization of SHG Images

In order to obtain accurate and statistically meaningful results from the SHG experiments, normalization of the image data was performed in order to directly compare SHG images recorded from different experiments. An internal calibration procedure was conducted after the completion of each experiment by using the SHG intensities measured from a continuous DOPC bilayer measured first in pure PBS and then in a 0.83 mM solution of tetracaine in PBS at pH 7.4. Prior to depositing the continuous DOPC

bilayer, a 0.1 M KOH solution was injected in the flowcell for 30 minutes to destroy the MLBA and remove all adsorbed species from the substrate. The SHG image was then normalized using the following equation:

$$Normalized\ image = \frac{flat\text{-}field\ corrected\ image - I_o^{SHG}}{I_{Tec}^{SHG} - I_{PBS}^{SHG}} \times constant\ , \tag{6.1}$$

where I_o^{SHG} is the average SHG intensity obtained from the two DOPC spots in each array in PBS at pH 7.4 (before adding tetracaine), I_{PBS}^{SHG} and I_{Tec}^{SHG} are the SHG intensities measured from the continuous DOPC bilayer in PBS pH 7.4 before and after introducing 0.83 mM tetracaine (in PBS at pH 7.4), respectively.

6.2.6 Equilibrium Binding Affinity of Tetracaine

The SHG images were collected at various bulk concentrations of tetracaine, increasing from low to high. Each concentration was allowed to incubate for at least 30 minutes before imaging to insure tetracaine binding to the lipid bilayer had reached equilibrium. The SHG intensity for each lipid component was plotted versus tetracaine concentration.

As described in equations 2.17 and 2.19 in Chapter 2, the SHG intensity (I_{SHG}) is proportional to N^2 which is the surface density squared; therefore, the Langmuir isotherm used to fit the integrated SHG intensity from each spot on the MLBA is expressed as:

$$\frac{I_{SHG}}{I_{SHG}^{Max}} = \left(\frac{K_a C}{1 + K_a C}\right)^2 , \tag{6.2}$$

where I_{SHG} is the measured SHG intensity as a function of the bulk tetracaine concentration C, K_a is the equilibrium association constant and I_{SHG}^{Max} is the maximum

SHG intensity at surface saturation. The Frumkin model takes account into the electrostatic interaction between charged molecules, which is given by:

$$\frac{I_{SHG}}{I_{SHG}^{Max}} = \left(\frac{K_a C \exp\left(2g\sqrt{I_{SHG}}/RT\right)}{1 + K_a C \exp\left(2g\sqrt{I_{SHG}}/RT\right)} \right)^2, \tag{6.3}$$

when $g > 0$, the interaction between the adsorbed molecules is attractive while a repulsive interaction is represented by $g < 0$. When $g = 0$, the Frumkin model becomes the Langmuir model. A statistical evaluation (F-test) was performed using SigmaPlot with a confidence level of 95% to determine the most appropriate model to be applied to the data.

6.3 Results and Discussion

MLBAs composed of eight different lipid components were used to examine the effect of lipid physical state and the presence of cholesterol on tetracaine binding in PBS buffer (100 mM NaCl and 50 mM Na_2HPO_4) at physiological pH 7.4. The pK_a of tetracaine in an aqueous solution is ~ 8.48[14] so the tetracaine used in this study is mostly positively charged at pH 7.4. Four primary lipid components, DOPC, SOPC, DMPC and DPPC, were examined with and without 28 mol % cholesterol. These different lipid compositions were deposited in a 5 column, 3 row array for a total of 15 individual spots. In each column of the array, the primary lipid component was prepared in duplicate while the same lipid containing cholesterol was deposited once. The last spot in column 1 is the control where no lipid was deposited. The positions of the lipid bilayer spots were kept consistent throughout this work. It should be noted that the two first DOPC spots in column 1 were not used in the calculation. These two spots, labeled with a fluorescent

dye rhodamine (Rh), were used to locate the position of the lipid bilayer spots in the array before imaging with the microscope.

6.3.1 Effect of Lipid Physical State

The effect of the lipid physical state on tetracaine binding was examined by comparing the relative adsorption of tetracaine to DOPC, SOPC, DMPC and DPPC bilayers which correspond to the lipid spots at the following positions in the array: 2A, 2B (DOPC, 18:1), 3A, 3B (SOPC, 18:0-18:1), 4A, 4D (DMPC, 14:0) and 5A, 5B (DPPC, 16:0), shown in Figure 6.2. The numbers in the parenthesis represent the number of carbons in the acyl chain followed by the number of double bonds in the acyl chain. The experiments examining the effect of lipid physical state were conducted at 18°C, 27°C and 46°C. At 18°C, DOPC and SOPC are in the liquid-crystalline (l_c) phase while DMPC and DPPC are in the solid-gel phase. When the temperature increases to 27°C, DOPC, SOPC and DMPC are in the l_c phase while DPPC is in the gel phase. At 46°C, all the lipids are in the l_c phase.

The effect of the lipid physical state was first investigated at 18°C. The SHG images of tetracaine binding to DOPC, SOPC, DMPC and DPPC bilayer spots at this temperature are represented in Figure 6.2. As the concentration is increased, more tetracaine associates into the lipid bilayers causing the intensity at each lipid bilayer spot to increase. The control spot (1C) remains unchanged over the concentration range confirming the specific binding of tetracaine to the lipid bilayers. The binding curves of tetracaine to DOPC, SOPC, DMPC and DPPC bilayers are shown in Figure 6.3. The data presented in the figure are the average of four bilayer spots from two independent arrays (two spots in each array). These data were best fit by the Langmuir isotherm model

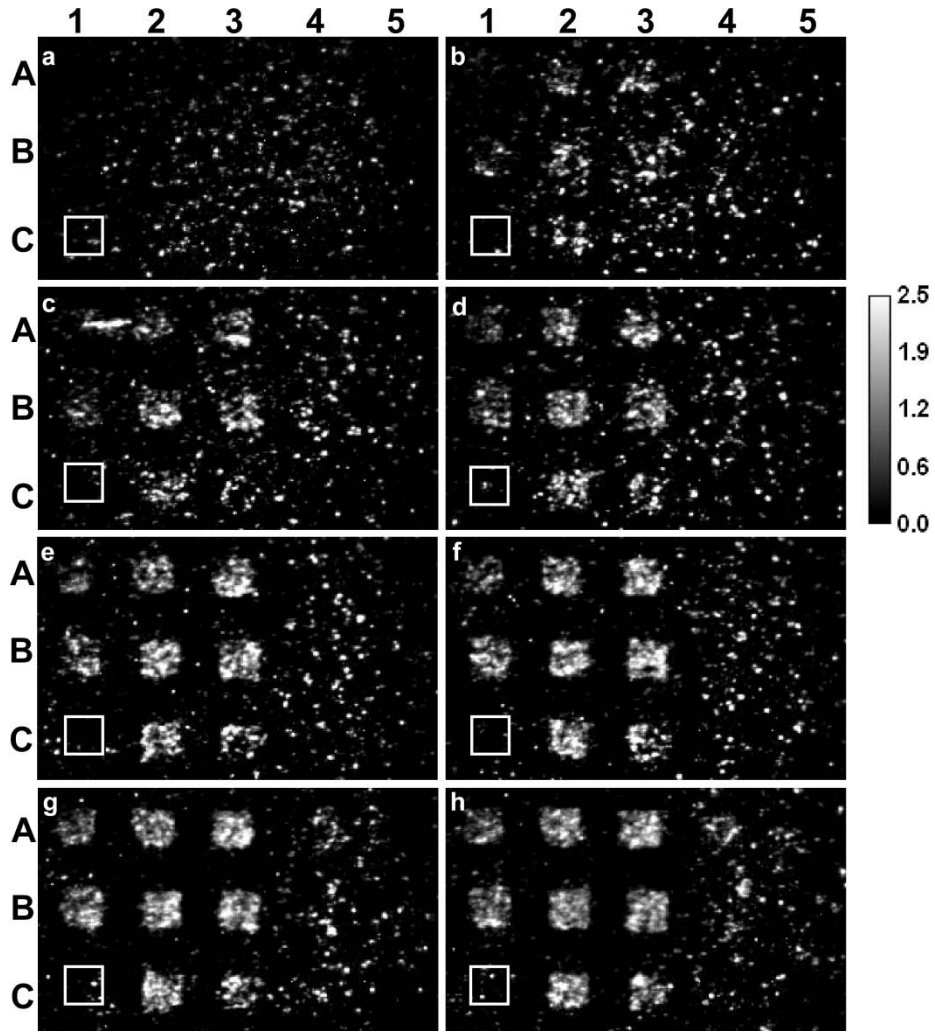

Figure 6.2 Normalized SHG images of tetracaine binding to a multicomponent lipid bilayer array which contains the following lipid compositions: DOPC (1A, 1B, 2A, 2B); no lipids, control spot (1C) labeled by the white box; DOPC + 28 mol % cholesterol (2C); SOPC (3A, 3B); SOPC + 28 mol % cholesterol (3C); DMPC (4A, 4B); DMPC + 28 mol % (4C); DPPC (5A, 5B); DPPC + 28 mol % cholesterol (5C). Each image represents a different bulk tetracaine concentration: 0 mM (a); 0.05 mM (b); 0.11 mM (c); 0.21 mM (d); 0.42 mM (e); 0.83 mM (f); 1.59 mM (g), and 3.32 mM (h). The images were collected at 18°C. Each bilayer patch is approximately 400 μm × 400 μm.

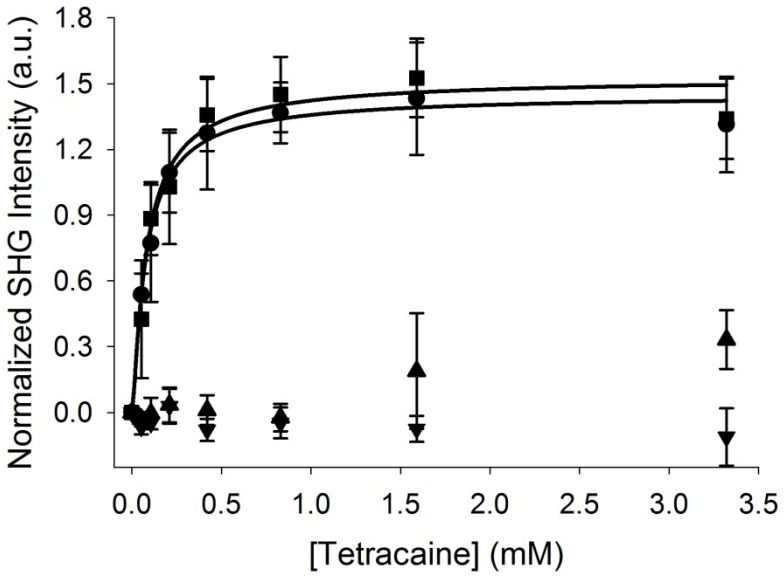

Figure 6.3 Normalized SHG intensities from the images in Figure 6.2 for the following lipid compositions: DOPC (circles), SOPC (squares), DMPC (upright triangles), and DPPC (inverted triangles). The lines are fits to the Langmuir adsorption isotherm model. The error bars represent the standard deviations from two independent bilayer arrays with two lipid spots in each array.

(equation 6.2) and the extracted equilibrium binding affinities are given in Table 6.1. It is assumed that a monolayer of tetracaine is formed in the lipid bilayer based on several factors. First, it has been previously proposed that tetracaine is present mainly in the outer leaflet of the lipid bilayer where the positive dimethylammonium group of tetracaine lies close to the negative phosphate group of the lipid interfacial region.[32] This proposed bilayer location is supported by an NMR study showing that no flip-flop of tetracaine across the lipid bilayer occurs.[32] Additionally, if tetracaine is present in both the inner and outer leaflets, the dipole moments of tetracaine in the two leaflets would cancel out, resulting in no net change in the SHG signal. In this study, an increase in the SHG intensity was observed with increasing tetracaine concentration up to 3.2 mM, suggesting that tetracaine binds as a monolayer in one leaflet of the bilayer. However, at concentrations above 3.2 mM, the intensity began to decrease which could be attributed to the binding of tetracaine into both leaflets of the bilayer. Although the decrease in the SHG intensity can be ascribed to the dipole moment cancellation of tetracaine, it is possible that the decrease in the intensity is due to the disruption of the lipid bilayer caused by high concentration of tetracaine.[33] Nonetheless, the binding data exhibit one plateau at saturation as opposed to multiple plateaus which indicates that a single adsorbed tetracaine layer is formed in the lipid bilayer. Collectively, from this information it can be inferred that the measured SHG signal in these experiments is from a monolayer of tetracaine inserting into one leaflet of the lipid bilayer.

Tetracaine binding to DMPC and DPPC bilayer spots at 18°C does not reach saturation over the concentration range used in this study, as seen in Figure 6.3, and thus it was not able to obtain the binding affinity of tetracaine to gel phase DMPC and DPPC.

Table 6.1 Measured binding affinity of tetracaine to lipid bilayers at different temperatures.

Lipid bilayer	$K_a \times 10^4$ (M^{-1})		
	18°C	27°C	46°C
DOPC	2.9 ± 0.2	1.3 ± 0.1	0.78 ± 0.08
SOPC	2.8 ± 0.5	1.4 ± 0.1	0.83 ± 0.04
DMPC	N.A.	0.53 ± 0.07	0.55 ± 0.08
DPPC	N.A.	N.A.	0.24 ± 0.08

Although the tetracaine binding cannot be quantitatively assessed, it is qualitatively observed that the binding affinity of tetracaine to DMPC and DPPC at this temperature would be the lowest of the lipids in this study. The data in Table 6.1 show that the binding affinity, K_a, of tetracaine at 18°C to the lipids in this study increases in the order DPPC ≈ DMPC < SOPC≈ DOPC. At 18 °C, DOPC and SOPC are in the l_c phase while DMPC and DPPC are in the gel phase. The higher K_a of tetracaine to DOPC and SOPC suggests that tetracaine associates into the l_c phase lipids to a greater extent than into the gel phase lipids DMPC and DPPC. This is due to the fact that lipids in the l_c phase are more loosely packed (~ 60-75 Å^2/molecule[34]) which allows tetracaine to partition into the bilayer more easily than the tightly packed solid-gel phase (~ 45-50 Å^2/molecule[34]). The association behavior of tetracaine reported here is consistent with literature reports that tetracaine incorporates more readily into l_c DMPC[14,31] and DPPC[20] liposomes as compared to lipids in gel phase. This same trend has been observed for other local anesthetic drugs, including dibucaine, bupivacaine and lidocaine.[35]

To further examine the impact of lipid phase on tetracaine binding, the same experiment was performed at a higher temperature, 27°C. The SHG images of tetracaine binding to the MLBA and the binding curves at this temperature are shown in Figures 6.4 and 6.5, respectively. Upon increasing the temperature from 18°C to 27°C, DMPC goes from the gel phase to the l_c phase which allows tetracaine binding to DMPC to significantly increase. It should be noted that tetracaine binding to DPPC bilayer spots at 27°C still does not reach saturation (Figure 6.4) and it can be deduced that the binding affinity of tetracaine to DPPC at this temperature would be the lowest relative to the other

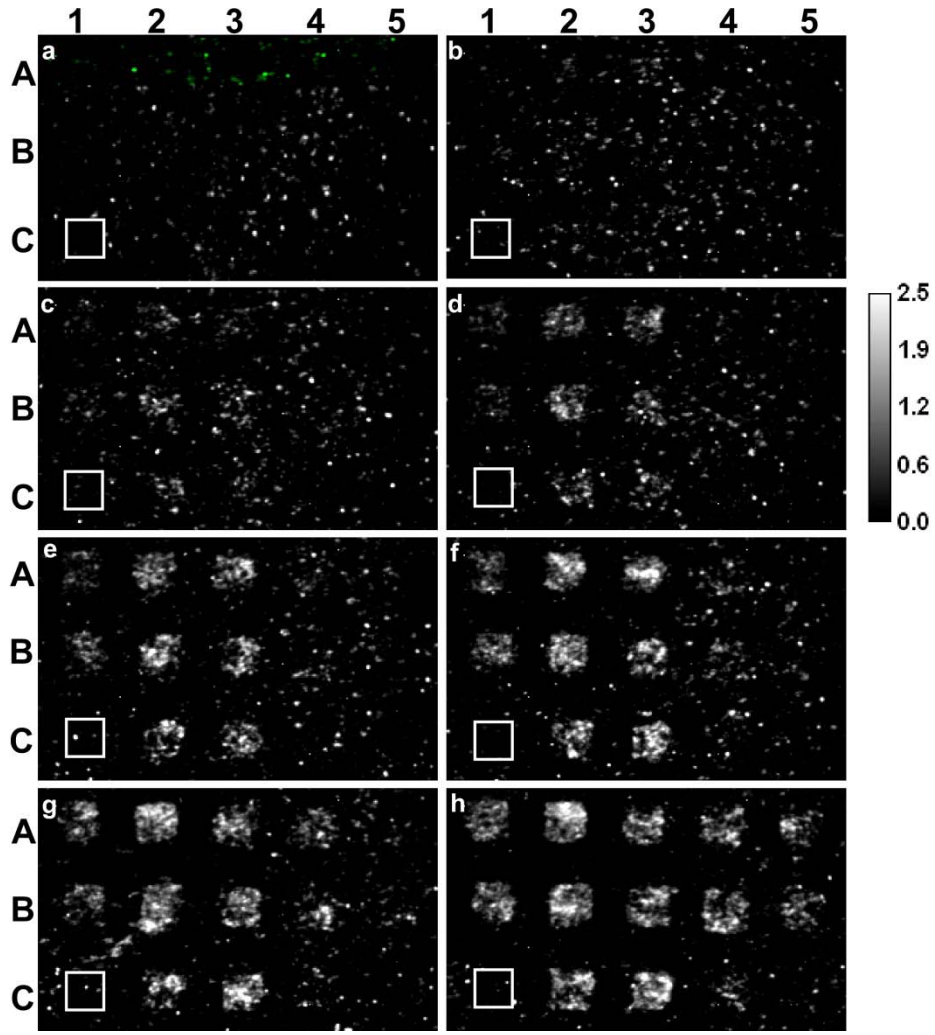

Figure 6.4 The normalized SHG images of tetracaine binding to a multicomponent lipid bilayer array which contains the following lipid compositions: DOPC (1A, 1B, 2A, 2B); no lipids, control spot (1C) labeled by the white box; DOPC + 28 mol % cholesterol (2C); SOPC (3A, 3B); SOPC + 28 mol % cholesterol (3C); DMPC (4A, 4B); DMPC + 28 mol % (4C); DPPC (5A, 5B); DPPC + 28 mol % cholesterol (5C). Each image represents a different bulk tetracaine concentration: 0 mM (a); 0.05 mM (b); 0.11 mM (c); 0.21 mM (d); 0.42 mM (e); 0.83 mM (f); 1.59 mM (g), and 3.32 mM (h). The images were collected at 27°C. Each bilayer patch is approximately 400 μm × 400 μm.

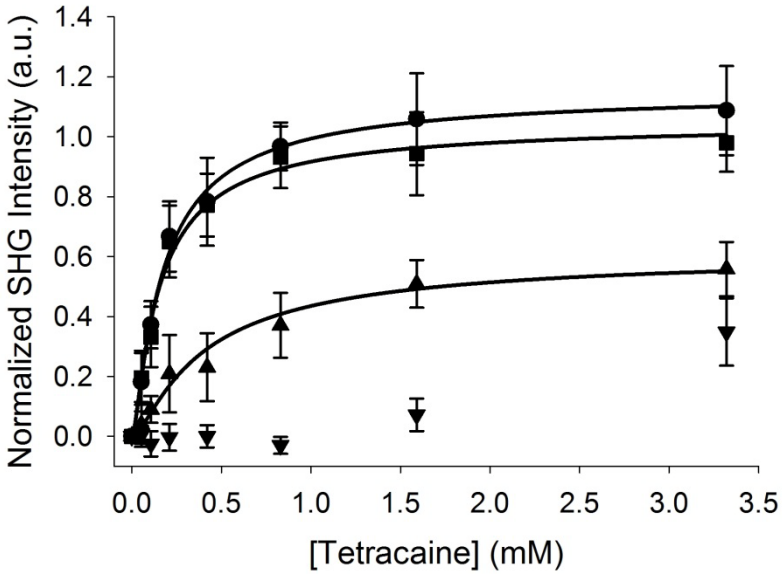

Figure 6.5 Normalized SHG intensities from the images in Figure 6.4 for the following lipid compositions: DOPC (circles), SOPC (squares), DMPC (upright triangles), and DPPC (inverted triangles). The lines are fits to the Langmuir adsorption isotherm model. The error bars represent the standard deviations from three independent bilayer arrays with two lipid spots in each array.

lipids in the study. The K_a of tetracaine to the DOPC, SOPC, DMPC and DPPC at 27°C is listed in Table 6.1 and increases in the order DPPC < DPMC < DOPC ≈ SOPC.

Similarly, when the temperature is increased to 46°C and DPPC enters the fluid phase there is an increase in tetracaine binding as illustrated in Figures 6.6 and 6.7. The K_a of tetracaine to DOPC, SOPC, DMPC and DPPC at 46°C is listed in Table 6.1. The K_a increases in the order DPPC < DMPC < DOPC ≈ SOPC. Interestingly, the K_a of tetracaine binding to the unsaturated lipids (DOPC and SOPC) is much greater than for the saturated lipids (DMPC and DPPC) when all the lipids are in the fluid phase. This could be related to the difference in the molecular packing of the unsaturated and saturated lipids. The *cis* double bond in the unsaturated lipids results in a larger area per molecule (~ 75 Å^2/molecule for l_c phase DOPC[34]) as compared to the saturated lipids (~ 67 Å^2/molecule for l_c DPPC[34]). Accordingly, the more loosely packed unsaturated lipids may allow more tetracaine binding. Surprisingly, very little work regarding tetracaine or other local anesthetic-lipid membrane interactions has been reported in the literature using unsaturated lipids, despite the fact that the lipids in cellular membranes are predominantly unsaturated.[36] Instead, saturated DMPC and DPPC are commonly used in tetracaine and other local anesthetic membrane studies.[10,14,37]

A significant reduction in teracaine binding to DOPC and SOPC was observed when the temperature increased from 18°C to 27°C and 46°C. The decrease in drug partitioning into fluid lipids at elevated temperatures was also reported by Wright *et al.* who found teniposide, an anticancer agent, partitioning into DOPC gradually decreases with increasing temperature above the lipid's phase transition temperature.[38] Liu and coworkers reported the effect of temperature on the decrease in the partition coefficients

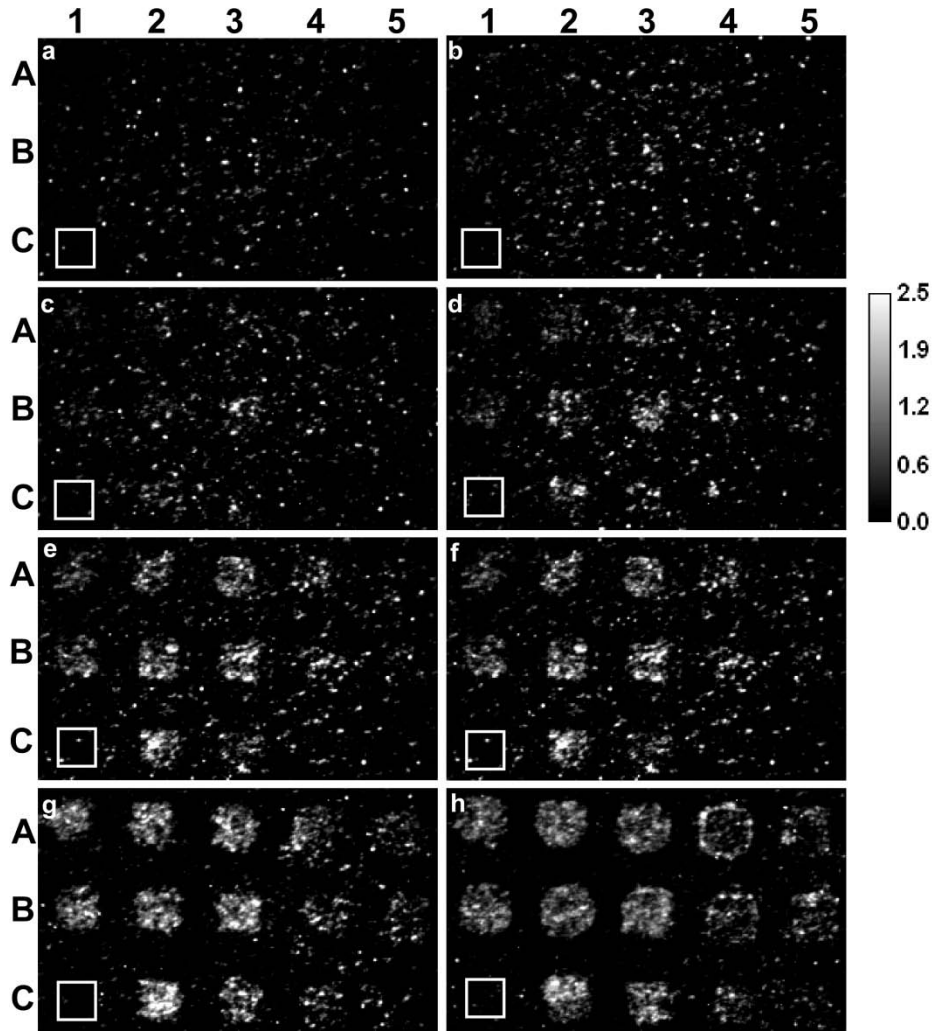

Figure 6.6 Normalized SHG images of tetracaine binding to a multicomponent lipid bilayer array which contains the following lipid compositions: DOPC (1A, 1B, 2A, 2B); no lipids, control spot (1C) labeled by the white box; DOPC + 28 mol % cholesterol (2C); SOPC (3A, 3B); SOPC + 28 mol % cholesterol (3C); DMPC (4A, 4B); DMPC + 28 mol % (4C); DPPC (5A, 5B); DPPC + 28 mol % cholesterol (5C). Each image represents a different bulk tetracaine concentration: 0 mM (a); 0.05 mM (b); 0.11 mM (c); 0.21 mM (d); 0.42 mM (e); 0.83 mM (f); 1.59 mM (g), and 3.32 mM (h). The images were collected at 46°C. Each bilayer patch is approximately 400 μm × 400 μm.

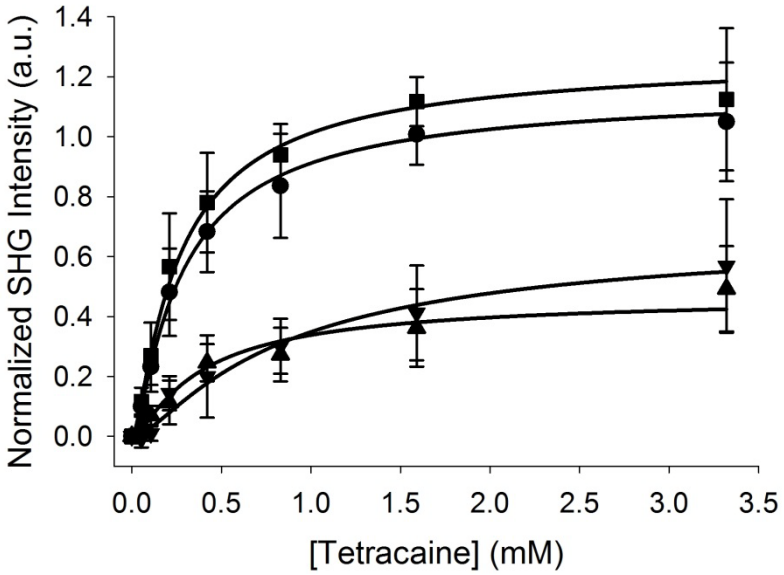

Figure 6.7 Normalized SHG intensities from the images in Figure 6.6 for the following lipid compositions: DOPC (circles), SOPC (squares), DMPC (upright triangles), and DPPC (inverted triangles). The lines are fits to the Langmuir adsorption isotherm model. The error bars represent the standard deviations from three independent bilayer arrays with two lipid spots in each array.

of beta blockers such as propranolol, alprenolol, and pindolol.[39] Additionally, a decrease in the partitioning of dopamine antagonists into fluid lipid bilayers with increasing temperature was obtained by Sarmento *et al*.[40] A possible explanation is that the water solubility of hydrophobic drugs increases with temperature resulting in the decrease in the membrane partitioning.[38,39] Another reason could be related to the conformational change in the lipid head group induced by temperature.[38,40,41] As the temperature increases, the positively charged amine of the phosphocholine head group, which normally remains parallel to the lipid bilayer surface, moves deeper into the hydrophobic core of the bilayer,[41] where tetracaine is located. The electrostatic repulsion between the amine group and protonated tetracaine could repel tetracaine from the lipid bilayer.

A quantitative comparison can be made between the measured binding affinities of tetracaine in this work and the values obtained by the UV-Vis SFG in Chapter 5 and the values published in the literature. Using UV-Vis SFG spectroscopy, an affinity of $5.1 \pm 0.1 \times 10^4$ was measured for tetracaine binding to a DOPC bilayer (at room temperature) (see Chapter 5).[42,43] In this work, a slightly smaller value ($1.3 \pm 0.1 \times 10^4$) was obtained for tetracaine associated into a DOPC bilayer at 27°C. Additionally, the adsorption models used to fit the data in the two studies are different. The Frumkin model fit best to the data in the previous study with a *g* value of -1.51 demonstrating the electrostatic repulsion between the charged tetracaine molecules. However, it was found that the Langmuir model was the statistically better fit to the data obtained by the SHG imaging. The difference between the Frumkin and Langmuir models is most pronounced at surface coverage below saturation. At low surface coverage, i.e., at low bulk tetracaine concentrations, the low signal/noise ratio in the SHG imaging data is not sufficient for the

nonlinear regression to identify the Frumkin behavior in the isotherm. On the other hand, the higher signal/noise ratio in the UV-Vis SFG experiment allows the Frumkin behavior in the isotherm to be statistically discerned as determined from a *F*-test analysis of the two models.

There are several factors that contribute to the lower signal/noise ratio in the SHG imaging data. The most significant difference between the two experiments is the illuminated sample area. For the UV-Vis SFG experiments a continuous bilayer was examined with an illumination area of approximately 18 mm^2 compared to the 0.16 mm^2 dimensions of the lipid spots in the current study with SHG imaging. As the SHG signal is proportional to the surface density squared, the two orders of magnitude decrease in the surface area of the lipid bilayer spots compared to the UV-SFG study will decrease the SHG signal by four orders of magnitude. Additionally, the sensitivity of the photocathode of the solar blind photomultiplier tube (~ 60 mA/W) used to collect the UV-Vis SFG signals is twice that of the image intensifier (~ 30 mA/W) used in the SHG imaging; thus, the measured SHG intensity is further reduced by a factor of two.

In another study, Zhang *et al*. obtained a partition coefficient of $(1.18 \pm 0.2) \times 10^4$ for DMPC (at 30°C) and $(1.31 \pm 0.13) \times 10^4$ for DPPC (at 45°C) at pH 5.5 (tetracaine is completely protonated).[14] In this work, a binding affinity of $(0.53 \pm 0.07) \times 10^4$ M^{-1} and $(0.24 \pm 0.08) \times 10^4$ M^{-1} were obtained for fluid DMPC (at 27°C) and DPPC (at 46°C), respectively. The difference between these values can be related to the models used to describe the interactions between tetracaine and lipid membrane. Zhang and coworkers employed a partitioning equilibrium model to study tetracaine and lipid membrane interaction with an unlimited number of binding sites in the membrane. The data

presented here were described by the Langmuir model, which has been proposed to be the more suitable model to characterize tetracaine-lipid membrane interaction.[31] Additionally, the 3D structure of the lipid vesicles used in Zhang' study could be more flexible thereby accommodating more tetracaine molecules as compared to the 2D structure of the planar supported lipid bilayers used here.

In addition to retrieving the binding affinity of tetracaine to lipid membranes, the maximum surface excess Γ_{max} of tetracaine in the membrane can be assessed using the SHG binding curves and the bulk partition coefficient of tetracaine as described previously in Chapter 5.[42] Knowledge of the surface excess of the drug in the membrane is essential in determining the bioavailability of the drug to the targeted protein that is embedded in the membrane. It is important to point out that this information cannot be determined solely from the partition coefficient data. The calculated Γ_{max} of tetracaine in DOPC, SOPC, DMPC and DPPC bilayers at 18°C, 27°C and 46°C is given in Table 6.2. In general, the Γ_{max} of tetracaine in the unsaturated lipid bilayers (DOPC and SOPC) is greater than in the saturated lipids bilayers (DMPC and DPPC). This is consistent with the higher binding affinity of tetracaine to the unsaturated lipids as compared to the saturated lipids. This behavior illustrates the correlation between the existence of double bonds in the lipid acyl chains and the resulting increase in the area per lipid molecule and an increase in tetracaine association. The effect of temperature on the Γ_{max} of tetracaine, however, is not significant. As the temperature increases from 18°C to 27°C and 46°C, the Γ_{max} of tetracaine in DOPC and SOPC does not significantly change, in contrast to the considerable reduction in the binding affinity of tetracaine to these lipids. This suggests that the molecular packing of the lipid membrane primarily governs the amount of

Table 6.2 Maximum surface excess of tetracaine in lipid bilayers.

Lipid bilayer	$\Gamma_{max} \times 10^{12}$ (molecule/cm^2)		
	18°C	27°C	46°C
DOPC	9.68 ± 0.08	8.63 ± 0.08	8.71 ± 0.08
SOPC	10.0 ±0.16	8.23 ± 0.08	9.11 ± 0.08
DMPC	N.A.	6.37 ± 0.16	5.56 ± 0.24
DPPC	N.A.	N.A.	6.69 ± 0.73

tetracaine adsorbed at saturation. When the lipids are in the fluid phase, the maximum surface excess is unaffected by temperature.

6.3.2 Effect of Cholesterol on Tetracaine Binding

The effect of 28 mol % cholesterol on tetracaine binding was investigated using the lipid bilayer spots at the following positions in the array: 2C (DOPC + CHO), 3C (SOPC + CHO), 4C (DMPC + CHO) and 5C (DPPC + CHO) at 18°C, 27°C and 46°C in Figure 6.2, 6.4 and 6.6, respectively. The binding curves for these lipids compositions are shown in Figure 6.8, 6.9 and 6.10. For comparison, the binding curves for the pure lipids were also re-plotted in the same figures. The binding affinities at 18°C, 27°C and 46°C are given in Table 6.3. It should be noted that the binding affinities of tetracaine to DMPC in the presence of cholesterol are lower than that of the pure lipid at 18°C. Similarly, the SHG response from the binding of tetracaine to DPPC bilayer containing cholesterol is lower than that of the pure lipid at both 27°C and 46°C. Accordingly, it can be inferred that cholesterol reduces the binding of tetracaine into DMPC bilayer at 18°C and DPPC bilayer at both 27°C and 46°C.

The incorporation of 28 mol % cholesterol into the lipid bilayers does not have any effect on tetracaine binding to DOPC but does decrease tetracaine binding to SOPC, DMPC and DPPC in the temperature range used. In particular, cholesterol decreases the K_a of tetracaine to SOPC 68 %, 40% and 10% at 18°C, 27°C and 46°C, respectively, as compared to the pure lipid. In DMPC, the K_a of tetracaine in the presence of cholesterol is reduced by 42% and 60% at 27°C and 46°C, respectively. The reduction in tetracaine binding caused by cholesterol has been previously reported.[10,14] Auger *et al.* found that the addition of 30 mol % cholesterol into fluid DMPC decreases the partition coefficient

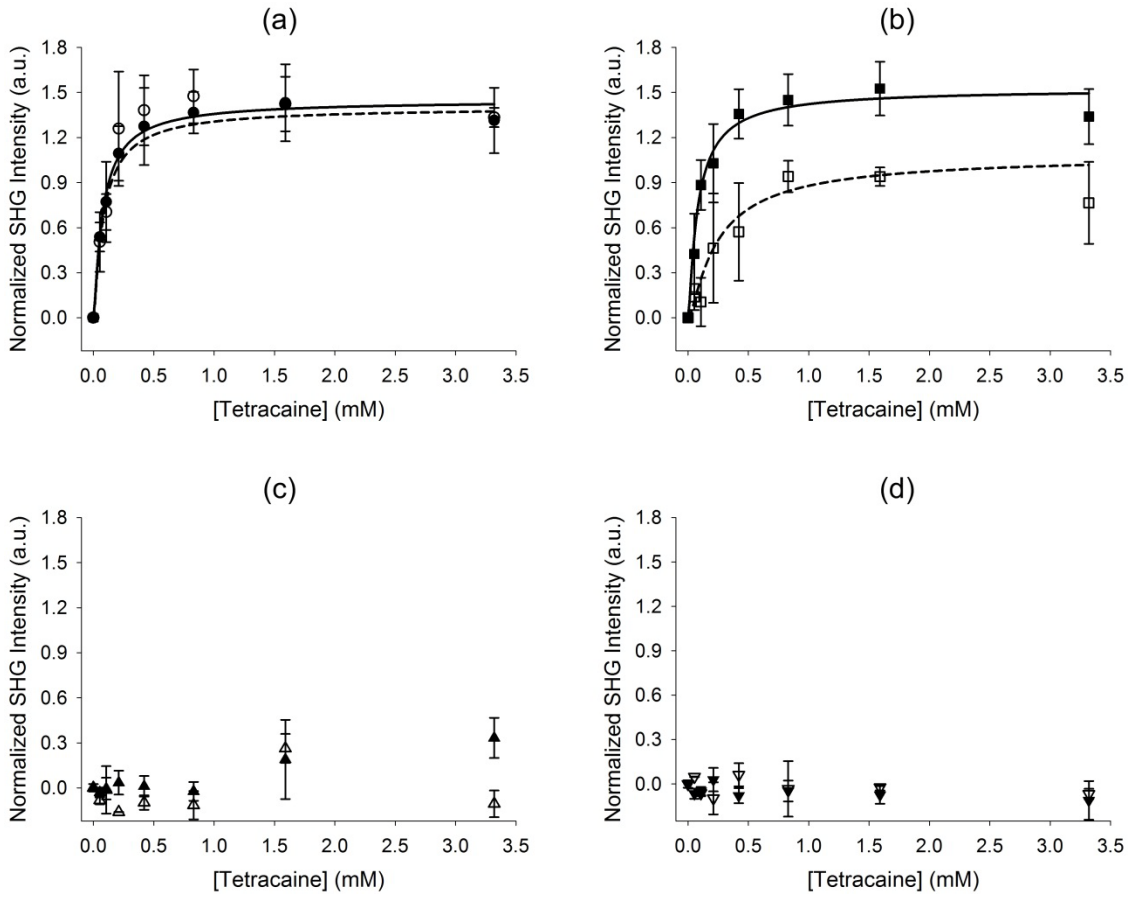

Figure 6.8 Normalized SHG intensities at 18°C for the following lipid compositions: (a) DOPC + 28 mol % cholesterol (open circles), DOPC (filled circles); (b) SOPC + 28 mol % cholesterol (open squares), SOPC (filled squares); (c) DMPC + 28 mol % cholesterol (open upright triangles), DMPC (filled upright triangles); and (d) DPPC + 28 mol % cholesterol (open inverted triangles), DPPC (filled inverted triangles). The lines are fits to the Langmuir adsorption isotherm model for the pure lipids (solid) and lipids containing cholesterol (dash). The error bars represent the standard deviations from two independent bilayer arrays with one lipid spot in each array.

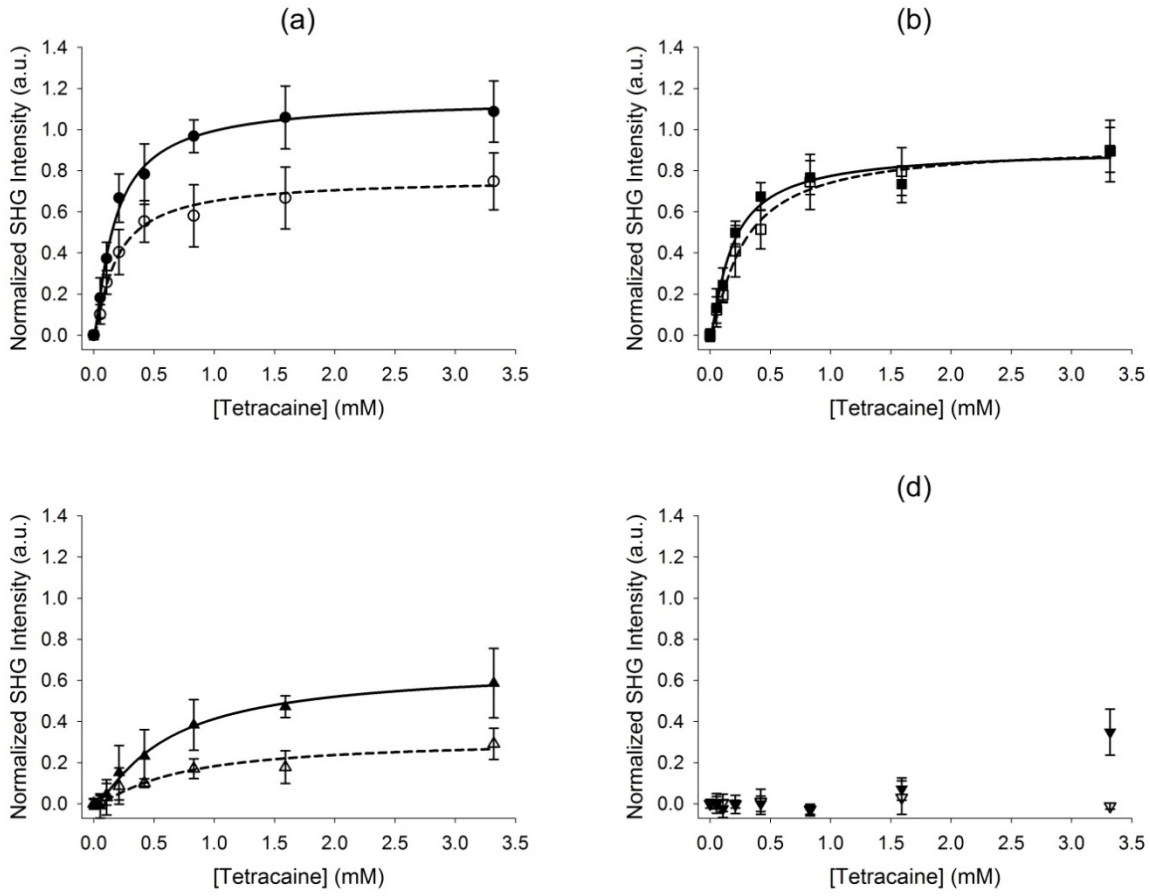

Figure 6.9 Normalized SHG intensities at 27°C for the following lipid compositions: (a) DOPC + 28 mol % cholesterol (open circles), DOPC (filled circles); (b) SOPC + 28 mol % cholesterol (open squares), SOPC (filled squares); (c) DMPC + 28 mol % cholesterol (open upright triangles), DMPC (filled upright triangles); and (d) DPPC + 28 mol % cholesterol (open inverted triangles), DPPC (filled inverted triangles). The lines are fits to the Langmuir adsorption isotherm model for the pure lipids (solid) and lipids containing cholesterol (dash). The error bars represent the standard deviations from three independent bilayer arrays with one lipid spot in each array.

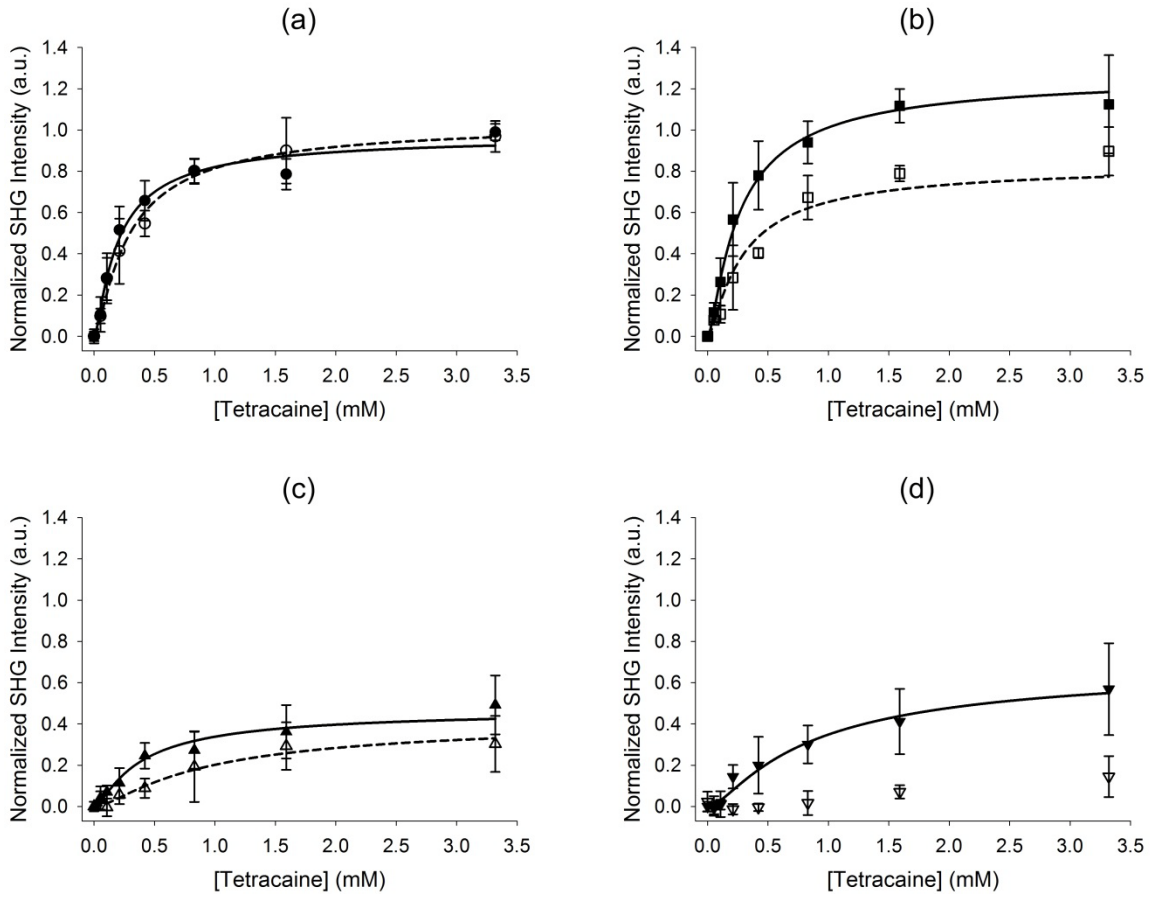

Figure 6.10 Normalized SHG intensities at 46°C for the following lipid compositions: (a) DOPC + 28 mol % cholesterol (open circles), DOPC (filled circles); (b) SOPC + 28 mol % cholesterol (open squares), SOPC (filled squares); (c) DMPC + 28 mol % cholesterol (open upright triangles), DMPC (filled upright triangles); and (d) DPPC + 28 mol % cholesterol (open inverted triangles), DPPC (filled inverted triangles). The lines are fits to the Langmuir adsorption isotherm model for the pure lipids (solid) and membranes containing cholesterol (dash). The error bars represent the standard deviations from three independent bilayer arrays with one lipid spot in each array.

Table 6.3 Measured binding affinity of tetracaine to lipid bilayers containing 28 mol % cholesterol at different temperatures.

Lipid bilayer	$K_a \times 10^4$ (M^{-1})		
	18°C	27°C	46°C
DOPC + CHO	2.7 ± 0.5	1.2 ± 0.1	0.76 ± 0.08
SOPC + CHO	0.89 ± 0.25	0.82 ± 0.06	0.75 ±0.11
DMPC + CHO	N.A.	0.31 ± 0.05	0.22 ± 0.05
DPPC + CHO	N.A.	N.A.	N.A.

of tetracaine in both the neutral and charged forms.[10] Zhang *et al*. observed a decrease on the partition coefficient of tetracaine to DPPC bilayer below and above its phase transition temperature with 28 mol % cholesterol in the bilayer.[14] The same effect has also been observed for other small molecules partitioning into lipid membranes.[38,39,44]

The addition of 28 mol % cholesterol, in the temperature range used in this study (18°C - 46°C), puts DOPC and SOPC in a liquid ordered phase (l_o),[45,46] which exhibits high fluidity as the liquid-crystalline phase but still possesses highly ordered acyl chains similar to those in the condensed phase.[47] On the other hand, for the binary mixtures of DMPC + CHO and DPPC + CHO, there is a phase coexistence between a solid ordered (s_o) and liquid ordered (l_o) below the T_m of the lipid and a liquid disordered (l_d) phase coexists with a liquid ordered (l_o) phase above the T_m.[48-50] It has been reported that phase segregation occurs between the s_o phospholipid-rich domains and the l_o cholesterol-rich domains, with a domain size in the range of ~ 18 nm[51,52] to few μm.[53] Although the l_o and l_d domains do coexist in a binary mixture of phospholipid and cholesterol, there are still questions as to whether or not the phase separation between the l_o phase and l_d phase occurs.[54-56] However, the nm-μm domain size in the s_o - l_o phases is too small to be identified in this work as the resolution of the SHG images limited by the image intensifier to ~ 14 μm.

The decrease in tetracaine binding caused by the incorporation of cholesterol into the lipid bilayers could be related to the increase in the lipid packing density/the decrease in the area per phospholipid induced by cholesterol.[57-59] This condensing effect of cholesterol has been previously reported for several lipid + cholesterol binary mixtures that exhibit a lower area per molecule compared to the average molecular areas of the

lipid and cholesterol alone.[53,60,61] In particular, Kim and coworkers obtained a maximum decrease in the average area of DPPC in the s_o - l_o phase coexistence region in a binary mixture of DPPC and 30 mol % cholesterol at 20°C.[57] Hung *et al*. also observed a reduction in DMPC lipid area per molecule when the lipid is in the l_o-l_d phases for DMPC and 30 mol % cholesterol at 30°C. Most likely, the more densely packed lipid bilayers created by the presence of cholesterol result in less tetracaine partitioning into the lipid bilayers. Additionally, cholesterol is known to reside in the hydrophobic core of the lipid bilayer with the hydroxyl group staying close to the lipid ester carbonyl head group.[62] Evidence from an NMR study showed that tetracaine is located closer to the interfacial region of DMPC containing 30 mol % cholesterol (in the l_o -l_d phases) as compared to pure DMPC (l_c).[10] This indicates that cholesterol occupies empty space between the lipids and could exclude tetracaine from the lipid bilayer resulting in a decrease in tetracaine binding.

One of the models which have been proposed to explain the condensing effect is the formation of a stoichiometric cholesterol and lipid complex.[53,63] In the condensed complex, the lipid acyl chains are more ordered as the interaction between cholesterol and the acyl chains facilitates the extension of the acyl chains adjacent to cholesterol indicated by an increase in the membrane thickness,[60,64] and a decrease in the number of *gauche* rotamers along the acyl chains.[65] The ordering effect is much more significant in saturated lipids than in unsaturated lipids as the proximity between the acyl chains and cholesterol facilitate the interaction between cholesterol and the lipids. In the unsaturated lipid DOPC, the *cis* double bond configuration between C-9 and C-10 forms a bend of 30 degrees in the aliphatic chains, leading to a conformational mismatch in contact with

cholesterol.[66] Therefore, the ordering effect of cholesterol on DOPC is much less than that on saturated lipids (DMPC, DPPC).[66,67] This explains why the effect of cholesterol on tetracaine binding to DOPC is insignificant as compared to DMPC. This behavior is further supported by a simulation study performed by Martinez-Seara and coworkers that showed that the ordering effect caused by cholesterol is minimized for DOPC but maximized for fully saturated 1,2-distearoyl-*sn*-glycero-3-phosphocholine DSPC (18:0, same chain length with DOPC).[68] In the case of the mixed-chain SOPC lipid that contains a saturated *sn-1* chain and a monounsaturated *sn-2* chain, an intermediate behavior between the fully saturated lipid (DMPC) and di-unsaturated lipid DOPC was observed in the present study. This observation is supported by recent molecular dynamics calculations that showed that the increase in the lipid bilayer thickness caused by the incorporation of 20 mol % cholesterol is greatest for DSPC, moderate for SOPC and lowest for DOPC, as compared to the pure lipid systems.[69] This study also demonstrated that cholesterol increases the order parameter *S*, which is used to quantify the ordering of the lipid acyl chain, in the order of DOPC < SOPC < DSPC.[69]

A reduction in the Γ_{max} of tetracaine upon the addition of 28 mol % cholesterol was observed for all the lipids, as listed in Tables 6.2 and 6.4. However, this reduction is not as significant as the decrease in K_a. In the presence of cholesterol, the Γ_{max} of tetracaine in the unsaturated lipids DOPC and SOPC is much higher than that in the saturated lipid DMPC, confirming that the lipid packing in the membrane is the predominate governor of the maximum amount of tetracaine adsorbed to the lipid bilayer.

Table 6.4 Maximum surface excess of tetracaine in lipid bilayers containing 28 mol % cholesterol at different temperatures.

Lipid bilayer	$\Gamma_{max} \times 10^{12}$ (molecule/cm^2)		
	18°C	27°C	46°C
DOPC + CHO	9.60 ± 0.16	7.02 ± 0.08	8.23 ± 0.16
SOPC + CHO	8.39 ± 0.25	7.82 ± 0.16	7.34 ± 0.32
DMPC + CHO	N.A.	4.60 ± 0.24	5.24 ± 0.40
DPPC + CHO	N.A.	N.A.	N.A.

6.3.3 Thermodynamics of Tetracaine Binding

In addition to providing information about the binding affinity and maximum surface excess of tetracaine in lipid bilayers, the data presented here can also be used to determine the thermodynamics of the binding process. The van't Hoff plot shown in Figure 6.11 was used to determine the enthalpy (slope) and entropy (intercept) for tetracaine binding to the lipid bilayers. These values are given in Table 6.5 in addition to the calculated free energy. As seen in Table 6.5, the binding of tetracaine to pure DOPC and SOPC as well as DOPC containing 28 mol % cholesterol (DOPC + CHO) is associated with a large negative change in enthalpy (ΔH) with values ranging from -32 to -34 kJ/mol. This can be attributed to the van der Waals interactions of the nonpolar portion of the drug with the hydrophobic region of the lipid bilayer where tetracaine inserts relative to the aqueous solution phase species.[70,71] The change in entropy (ΔS) is much smaller (-26 to -33 J/mol K) most likely due to the competing processes of desolvation of tetracaine upon insertion into the membrane (increase in S) and the ordering of water at the interface of the lipid bilayer (decrease in S) due to the presence of the positive charge on tetracaine. It has been reported that the water molecules at the air/water interface become more ordered, i.e., more hydrogen bonded with icelike structure in the presence of charged surfactants at the interface.[72] The charged surfactants create a large electrostatic field which induces the alignment of the water at the interface.[72] Similarly, the presence of the protonated tetracaine in the lipid bilayer could increase the surface potential, thus facilitating the ordering of the water at the interface. The significant contribution from ΔH to the free energy (ΔG ~ -23 kJ/mol) indicates that the binding of tetracaine to the lipid bilayers is largely enthalpy-driven. This finding is

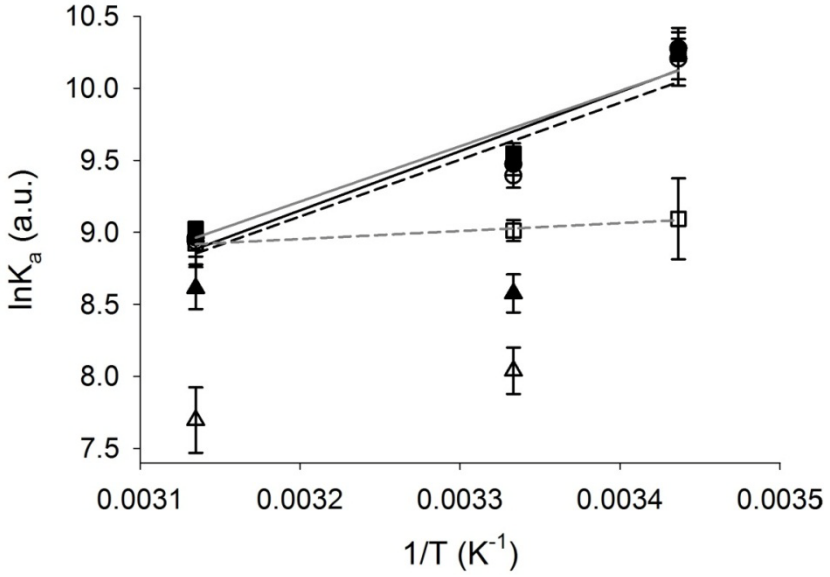

Figure 6.11 Van't Hoff plot for tetracaine binding to various lipid components: DOPC (filled circles), DOPC + 28 mol % cholesterol (open circles), SOPC (filled squares), SOPC + 28 mol % cholesterol (open squares), DMPC (filled triangles), DMPC + 28 mol % cholesterol (open triangles). The lines are the linear fits for the pure lipids (solid) and lipids containing cholesterol (dash): DOPC (black) and SOPC (grey).

Table 6.5 Free energy, enthalpy, and entropy of tetracaine binding to lipid bilayers of various compositions.

Lipid bilayer	ΔG* (kJ/mol)	ΔH (kJ/mol)	ΔS (J/mol K)
DOPC	-23.6 ± 0.19	-34.2 ± 10.9	-33.4 ± 36.0
DOPC + CHO	-23.4 ± 0.21	-32.8 ± 14.4	-29.3 ± 47.5
SOPC	-23.8 ± 0.18	-31.9 ± 10.5	-25.6 ± 34.7
SOPC + CHO	-22.5 ± 0.18	-4.58 ± 0.89	59.7 ± 2.94

* determined at 27°C

consistent with previous studies which show that ΔH dominates the partitioning of small molecules into the lipid membranes.[70,71,73-75]

Interestingly, the thermodynamics of tetracaine binding to SOPC + CHO is entirely different. The enthalpic contribution is small (- 4.6 kJ/mol) while the entropy increases and becomes positive (~ 60 J/mol K). A similar decrease in the enthalpic contribution was reported by Rowe *et al.* for alcohols partitioning into lipid bilayers in the presence of cholesterol, which they attributed to the disruption of the lipid packing by the alcohol.[76] As previously discussed, cholesterol increases the lipid packing density and order of the SOPC acyl chains greater than those of DOPC, and thus it is likely that tetracaine disrupts the more densely packed SOPC + CHO to a greater extent than DOPC + CHO, causing a larger reduction in the van der Waals interactions between the lipid molecules. This results in a decrease in enthalpy when tetracaine binds to SOPC in the presence of cholesterol. The relatively large increase in entropy observed for tetracaine binding to SOPC + CHO may be explained by a disordering of the lipid acyl chains induced by tetracaine.[10] The ordering of the lipid acyl chains by cholesterol is much more pronounced in SOPC relative to DOPC due to the close proximity of cholesterol to the saturated *sn-1* chains of SOPC. Consequently, when tetracaine binds to the lipids the better ordered SOPC + CHO undergoes a larger entropic increase as the lipid transforms from a relatively ordered state into a disordered one. This larger entropy contribution indicates that the binding of tetracaine to SOPC + CHO is entropy-driven.

The enthalpy and entropy for tetracaine binding to DMPC and DMPC + CHO were not obtained in this work as the binding affinities at 18°C were not available. However, as previously mentioned it can be inferred that the binding affinities of

tetracaine to DMPC and DMPC + CHO at 18°C would be lower than at 27°C based on the data in Figures 6.8 and 6.9. This is consistent with an entropy-driven binding process as observed with SOPC + CHO. It is important to note that the previously discussed unsaturated lipids do not go through a phase transition over the temperature range presented here. The introduction of this phase change to DMPC and DMPC + CHO complicates the interpretation of the thermodynamic behavior beyond the scope of the present work.

6.3.4 Neutral and Charged Tetracaine Binding

In the previous section, the interactions between tetracaine and lipid membranes were characterized at physiological pH (~ 7.4) where the drug is mostly positive charged (92% charged and 8% neutral). In this section, the interactions between tetracaine and the MLBAs were examined at different pHs in order to investigate the binding properties of different charge states of the drug, completely protonated and neutral. As the pK_a of tetracaine in aqueous solution is 8.48,[77] the pH of the tetracaine solution was adjusted to 5.5 and 9.5 to ensure that tetracaine is either completely charged or neutral, respectively. It should be noted that tetracaine is neutral at pH 11; however, the solubility of tetracaine in PBS decreases above pH 9.5. For this reason, in order to investigate neutral tetracaine while avoiding solubility issues, a pH of 9.5 was used in this study, where 91% of tetracaine is in the neutral state.

The effect of the tetracaine charge state on its binding to lipid membranes was examined by comparing the relative SHG responses from 1.0 mM tetracaine in PBS at pH 9.5 and pH 5.5 binding to MLBAs composed of DOPC, SOPC, DMPC and DPPC bilayers with and without 28 mol % cholesterol. These experiments were conducted at

18°C, 27°C and 46°C and the positions of the lipid bilayer spots in the MLBAs are consistent with the previous section. As seen in Figure 6.12, the SHG intensity for bilayer bound tetracaine is much higher at pH 9.5 than pH 5.5. The control spot (1C) remains unchanged over the concentration range confirming the specific binding of tetracaine to the lipid bilayers. The normalized square-root of the SHG intensity, which is directly proportional to the amount of bound tetracaine in the bilayer, at 18°C, 27°C and 46°C is plotted in Figure 6.13, 6.14, and 6.15, respectively.

As seen in Figures 6.13a, 6.14a and 6.15a, the square-root of the SHG intensity from tetracaine binding to all lipid bilayer spots over the temperature range used in the study (18°C - 46° C) is significantly higher when the pH of the tetracaine solution is 9.5. This indicates that the neutral form of tetracaine (pH 9.5) binds to a greater extent to the lipids in both liquid-crystalline and solid-gel phases than the charged form (pH 5.5). The same behavior is observed for the lipids containing 28 mol % cholesterol (see Figures 6.13b-6.15b). The favored binding of the neutral form of tetracaine to lipid bilayers relative to the charged species is attributed to the stronger hydrophobic interactions between the neutral drug and the hydrocarbon acyl chains of the lipids.[10] The larger degree of binding observed for neutral tetracaine relative to the charged species is consistent with its higher partition coefficient ($logP_{neutral}$ = 3.32 ± 0.02 and $logP_{charged}$ = 2.11 ± 0.03).[78] It has also been previously reported that the neutral form of tetracaine partitions more to the lipid bilayers in both fluid and solid-gel phases.[10,77] This same trend has been observed for other local anesthetics including dibucaine, bupivacaine and lidocaine.[35,79]

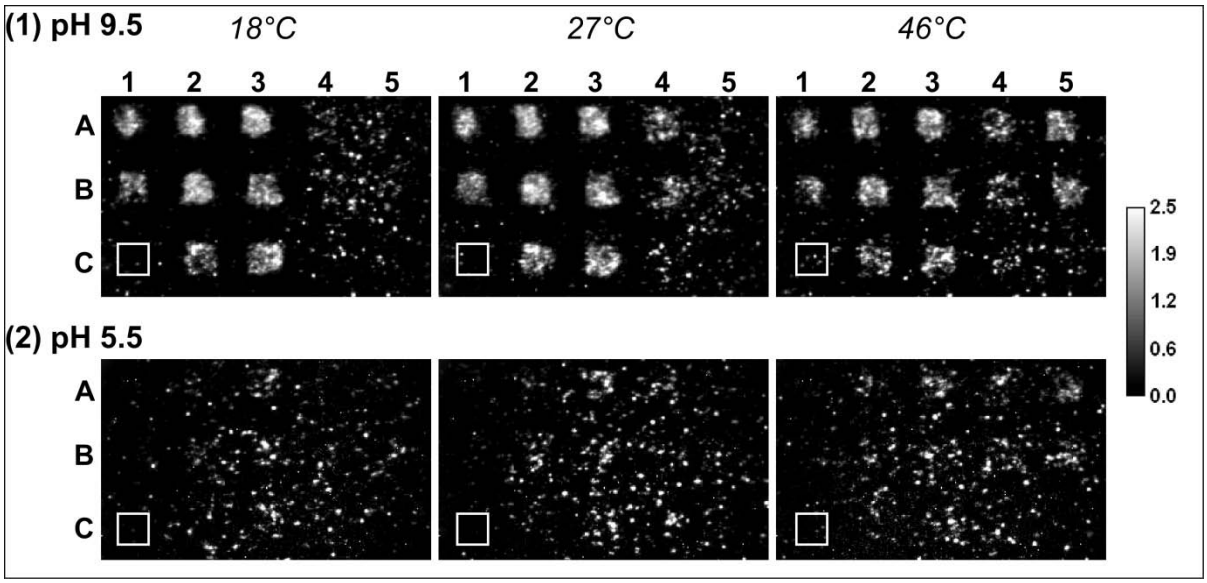

Figure 6.12 The normalized SHG images of 1.0 mM tetracaine in PBS at pH: (1) 9.5 and (2) 5.5 binding to a multicomponent lipid bilayer array which contains the following lipid compositions: DOPC (1A, 1B, 2A, 2B); no lipids, control spot (1C) labeled by the white box; DOPC + 28 mol % cholesterol (2C); SOPC (3A, 3B); SOPC + 28 mol % cholesterol (3C); DMPC (4A, 4B); DMPC + 28 mol % (4C); DPPC (5A, 5B); DPPC + 28 mol % cholesterol (5C). The images were collected at 18°C (left), 27°C (middle) and 46°C (right). Each bilayer patch is approximately 400 μm × 400 μm.

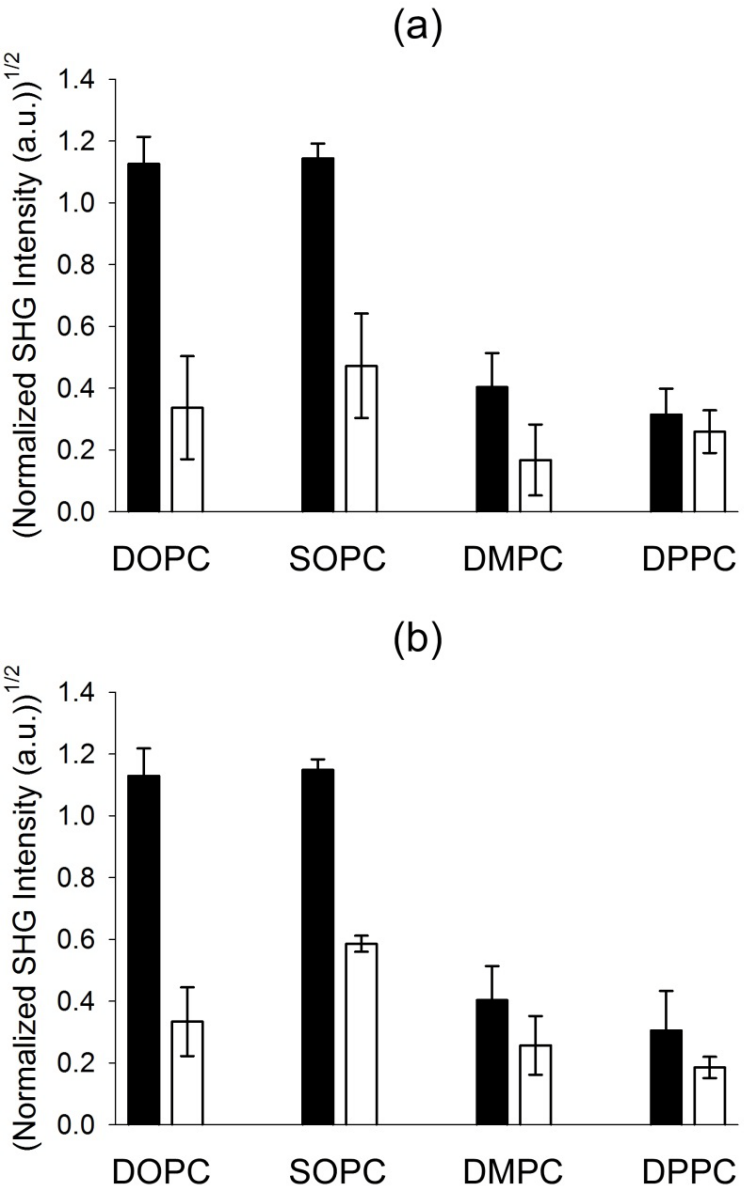

Figure 6.13 Normalized square-root of the SHG intensity from 1.0 mM tetracaine binding at 18°C to various lipid components: DOPC, SOPC, DMPC and DPPC without cholesterol (a) and with 28 mol % cholesterol (b). The filled bar and the empty bar represent pH 9.5 and 5.5, respectively. The error bars depict the standard deviations from at least two separate arrays with two spots for the pure lipids and one spot for the lipids containing cholesterol.

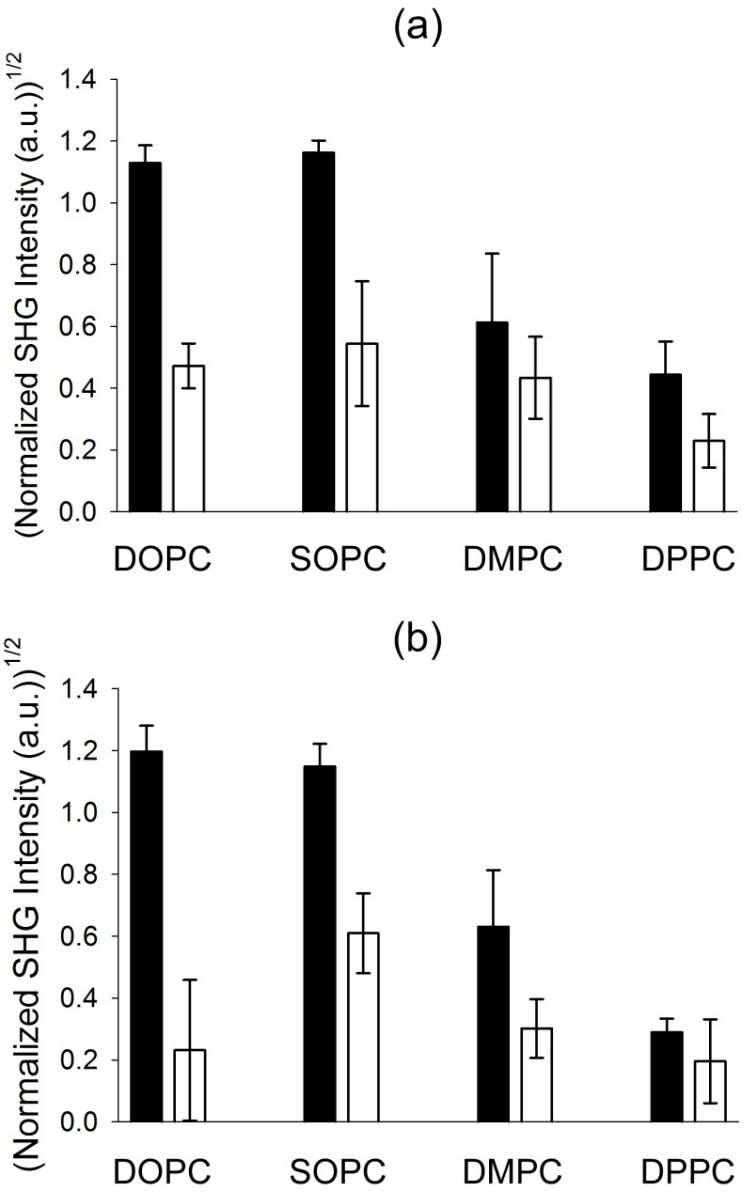

Figure 6.14 Normalized square-root of the SHG intensity from 1.0 mM tetracaine binding at 27°C to various lipid components: DOPC, SOPC, DMPC and DPPC without cholesterol (a) and with 28 mol % cholesterol (b). The filled bar and the empty bar represent pH 9.5 and 5.5, respectively. The error bars depict the standard deviations from at least two separate arrays with two spots for the pure lipids and one spot for the lipids containing cholesterol.

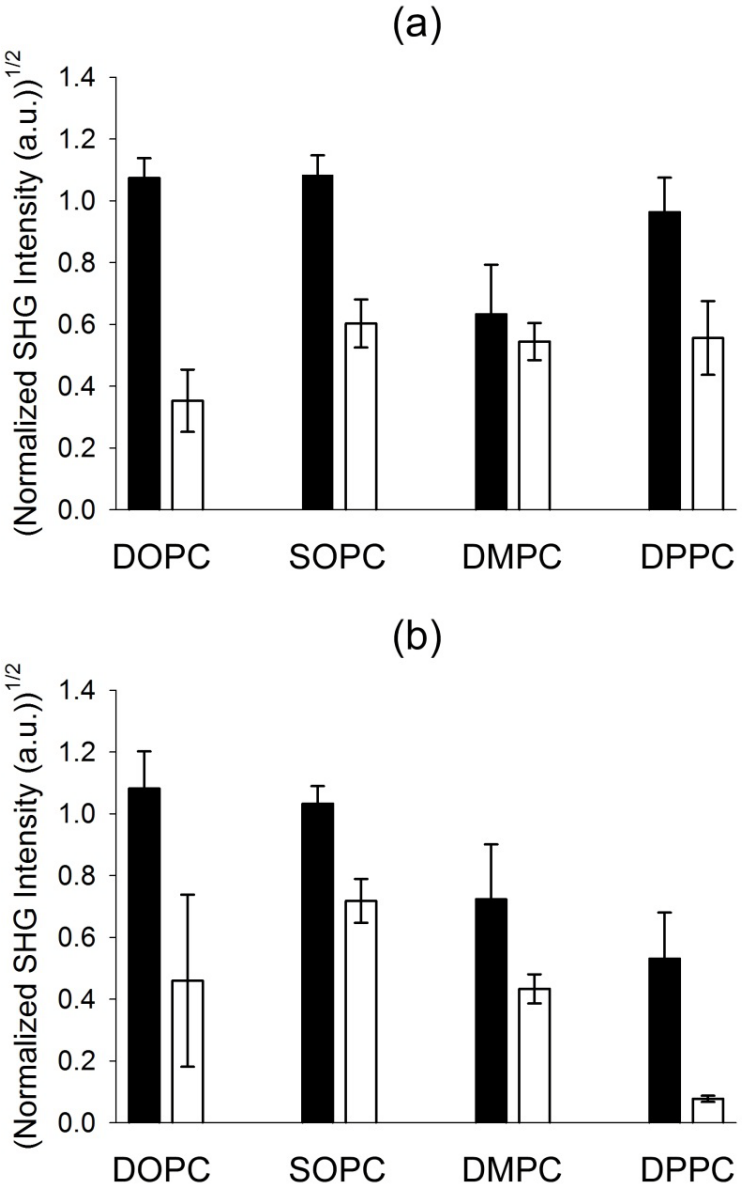

Figure 6.15 Normalized square-root of the SHG intensity from 1.0 mM tetracaine binding at 46°C to various lipid components: DOPC, SOPC, DMPC and DPPC) without cholesterol (a) and with 28 mol % cholesterol (b). The filled bar and the empty bar represent pH 9.5 and 5.5, respectively. The error bars depict the standard deviations from at least two separate arrays with two spots for the pure lipids and one spot for the lipids containing cholesterol.

6.3.5 Effect of Charged Lipids

The effect of charged lipids on tetracaine binding was also investigated in this study. At a pH of 7.4, 92% of tetracaine is positively charged; therefore, changing the surface charge of the lipid bilayer should cause a change in the partitioning of tetracaine at this pH by changing the electrostatic interactions between the drug and the lipid membrane. The surface charge of the lipid membrane was altered by incorporating either the negatively charged lipid DOPG or the positively charged lipid DOTAP into a zwitterionic DOPC lipid bilayer. The chemical structures of DOPG and DOTAP are shown in Figure 6.1. Figure 6.16 shows a representative image of 4.5 mM tetracaine binding to pure DOPC lipid bilayers as well as DOPC bilayers containing 10 mol% DOTAP, 20 mol % DOTAP, 10 mol % DOPG, and 20 mol % DOPG. Increasing the amount of DOTAP in the DOPC bilayer reduces the SHG intensity of the lipid spots while the intensity increases with amount of DOPG. The effect of these charged lipids on tetracaine binding was quantitatively evaluated by comparing the square-root of the SHG intensity of DOPC membranes containing DOPG and DOTAP relative to pure DOPC bilayers (Figure 6.17a). The data in Figure 6.17a are the average of four independent experiments. For each experiment, all bilayer compositions are triplicated in the array except for pure DOPC which is duplicated. It should be noted that the lipid array images were flat-field corrected and normalized by subtracting the image of a continuous DOPC bilayer in PBS pH 7.4 formed on the same substrate upon completion of the experiment (see section 6.2.5). The result of this subtraction was then divided by the image of a continuous DOPC bilayer in 4.5 mM tetracaine solution (in PBS pH 7.4). As seen in Figure 5.16a, the square-root of the SHG intensity was reduced by 10% and 17% relative

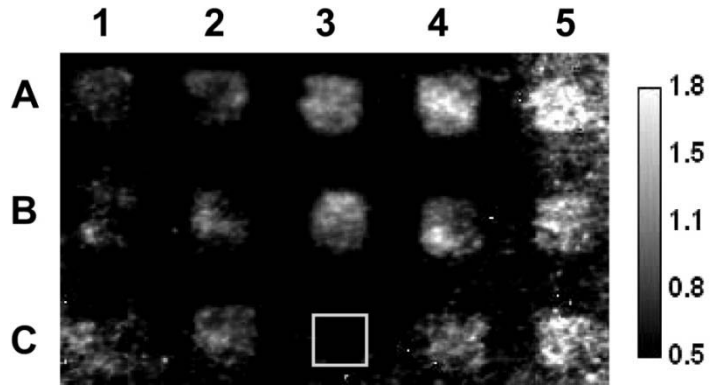

Figure 6.16 Normalized square-rooted SHG image of 4.5 mM tetracaine in PBS pH 7.4 binding to a multicomponent lipid bilayer array which contains the following lipid compositions: DOPC + 20 mol % DOTAP (1A, 1B, 1C); DOPC + 10 mol % DOTAP (2A, 2B, 2C); DOPC (3A, 3B); no lipid, control spot (3C) labeled by the white box; DOPC + 10 mol % DOPG (4A, 4B, 4C); DOPC + 20 mol % DOPG (5A, 5B, 5C). Each bilayer patch is approximately 400 μm × 400 μm.

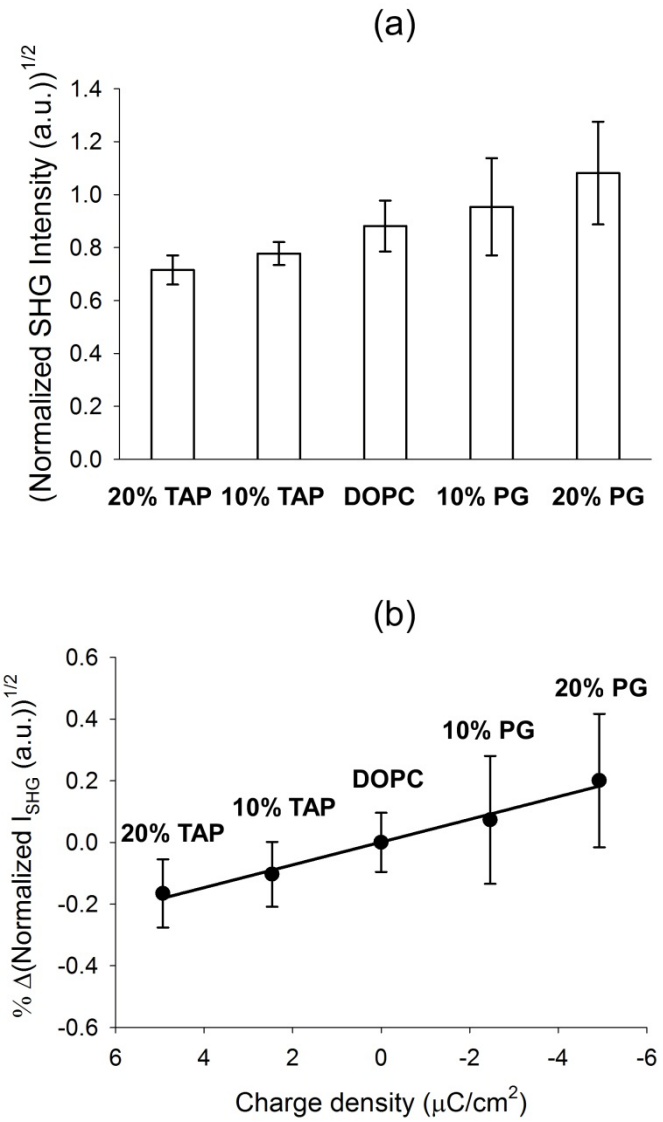

Figure 6.17 Effect of charged lipids on tetracaine binding (a) Square-root of the SHG intensity from 4.5 mM tetracaine binding to various lipid components: DOPC+ 20 mol % DOTAP; DOPC + 10 mol % DOTAP; DOPC; DOPC + 10 mol % DOPG; and DOPC + 20 mol % DOPG. The data are the average from the four independent arrays. (b) % change in square-root of the SHG intensity vs. surface charge density for: DOPC+ 20 mol % DOTAP; DOPC + 10 mol % DOTAP; DOPC; DOPC + 10 mol % DOPG; and DOPC + 20 mol % DOPG.

to pure DOPC when 10 mol % and 20 mol % DOTAP were added, respectively. The decrease in tetracaine binding to in the presence of DOTAP is due to the electrostatic repulsion between positively charged tetracaine and positively charged DOTAP. In contrast, the presence of 10 mol % and 20 mol % DOPG resulted in attractive electrostatic interactions between the drug and the lipid membrane which increased the square-root of the SHG intensity relative to pure DOPC by 7% and 20%, respectively. The stronger partitioning of the charged form of tetracaine into negatively charged membranes has been previously observed with dimyristoylphosphatidic acid (DMPA) vesicles[80] while a similar behavior was observed for another local anesthetic, dibucaine.[37] The repulsive interactions between charged tetracaine and cationic lipid membranes, however, have not yet been reported.

The change in tetracaine binding to lipid bilayers caused by electrostatic interactions can be related to the charge density which arises from the presence of DOPG or DOTAP in the DOPC bilayer. Assuming a surface area of 70 $Å^2$ for a single DOPC, DOPG and DOTAP lipids,[34] the number of charges per unit area due to the incorporation of 10 and 20 mol % DOPG in the DOPC bilayer was calculated to be - 2.29 and - 4.58 $\mu C/cm^2$, respectively. The calculated charge density is the same for DOPC bilayers with 10 and 20 mol % DOTAP but with the opposite sign. Figure 6.17b shows the percentage change in the square-root of the SHG intensity versus the lipid charge density ($\mu C/cm^2$). The linear correlation of the SHG data with the number of charges in the lipid bilayer illustrates the electrostatic interactions between the charged tetracaine and the charged lipid bilayers.

6.4 Summary

This work has demonstrated the use of counter-propagating SHG microscopy for the detection of drug-membrane interactions. The use of an MLBA allowed the effects of lipid physical state and cholesterol content on tetracaine binding to be investigated simultaneously. The results show that tetracaine binds more strongly into lipid bilayers in the liquid-crystalline phase as compared to the solid-gel phase. Cholesterol reduces the binding affinity of tetracaine to saturated DMPC and DPPC and mixed chain (saturated *sn-1* and monounsaturated *sn-2*) SOPC while having no effect on di-unsaturated DOPC. Additionally, the maximum surface excess of tetracaine in the unsaturated lipids is greater than that in the saturated lipids. Furthermore, the binding of tetracaine into DOPC and SOPC bilayers is governed by enthalpic contributions while the entropy dictates the tetracaine binding to DMPC. The presence of cholesterol does not change the thermodynamics of tetracaine binding to DOPC but makes the binding of tetracaine to SOPC become entropy-driven. The neutral form of tetracaine binds to the lipids in both gel and liquid-crystalline phases to a greater extent than the charged species. The presence of the cationic DOTAP lipid lowers the amount of tetracaine binding to a DOPC bilayer while the anionic DOPG lipid increases tetracaine binding to a DOPC bilayer. The study presented in this chapter illustrates that SHG imaging can be used to directly image and quantitatively measure the association of a drug molecule into multicomponent lipid microarrays without using any extrinsic label. More interestingly, the drug concentration in the membrane is accessible with the use of SHG data and the knowledge of the drug partition coefficient. The signal/noise ratio in the SHG imaging experiments can be improved by using a SHG wavelength in better resonance with the

electronic transitions of tetracaine and/or using a more sensitive detector for image acquisition. Additionally, the acquisition time can be speeded up with the use of a high repetition rate laser. This work opens up further opportunities for the use of SHG imaging in high-throughput screening applications.

6.5 References

(1) Kung, L. A.; Kam, L.; Hovis, J. S.; Boxer, S. G. *Langmuir* **2000**, *16*, 6773-6776.

(2) Yee, C. K.; Amweg, M. L.; Parikh, A. N. *Adv. Mater. (Weinheim, Ger.)* **2004**, *16*, 1184-1189.

(3) Cremer, P. S.; Yang, T. *J. Am. Chem. Soc.* **1999**, *121*, 8130-8131.

(4) Yamazaki, V.; Sirenko, O.; Schafer Robert, J.; Nguyen, L.; Gutsmann, T.; Brade, L.; Groves Jay, T. *BMC Biotechnol* **2005**, *5*, 18-28.

(5) Yang, T.; Jung, S.-y.; Mao, H.; Cremer, P. S. *Anal. Chem.* **2001**, *73*, 165-169.

(6) Smith, K. A.; Gale, B. K.; Conboy, J. C. *Anal. Chem.* **2008**, *80*, 7980-7987.

(7) Burridge, K. A.; Figa, M. A.; Wong, J. Y. *Langmuir* **2004**, *20*, 10252-10259.

(8) Custodio, J. B.; Almeida, L. M.; Madeira, V. M. *Biochem. Biophys. Res. Commun.* **1991**, *176*, 1079-1085.

(9) Boulanger, Y.; Schreier, S.; Smith, I. C. *Biochemistry* **1981**, *20*, 6824-6830.

(10) Auger, M.; Jarrell, H. C.; Smith, I. C. P. *Biochemistry* **1988**, *27*, 4660-4667.

(11) Auger, M.; Smith, I. C. P.; Mantsch, H. H.; Wong, P. T. T. *Biochemistry* **1990**, *29*, 2008-2015.

(12) Fox, C. B.; Horton, R. A.; Harris, J. M. *Anal. Chem.* **2006**, *78*, 4918-4924.

(13) Barghouthi, S.; Eftink, M. R. *Biophys. Chem.* **1993**, *46*, 13-19.

(14) Zhang, J.; Hadlock, T.; Gent, A.; Strichartz, G. R. *Biophy. J.* **2007**, *92*, 3988-4001.

(15) Arkin, I. T.; Russ, W. P.; Lebendiker, M.; Schuldiner, S. *Biochemistry* **1996**, *35*, 7233-7238.

(16) Aoki, P. H. B.; Alessio, P.; De Saja, J. A.; Constantino, C. J. L. *J. Raman Spectrosc.* **2010**, *41*, 40-48.

(17) Haugland, R. P. *Handbook of Fluorescent Probes and Research Chemicals*; 6th ed.; Molecular Probes Inc.: Eugene, OR, 1996.

(18) Heithier, H.; Ward, L. D.; Cantrill, R. C.; Klein, H. W.; Im, M. J.; Pollak, G.; Freeman, B.; Schiltz, E.; Peters, R.; Helmreich, E. J. *Biochim. Biophys. Acta* **1988**, *971*, 298-306.

(19) Abdiche, Y. N.; Myszka, D. G. *Anal. Biochem.* **2004**, *328*, 233-243.

(20) Nussio Matthew, R.; Sykes Matthew, J.; Miners John, O.; Shapter Joseph, G. *Chem. Med. Chem.* **2007**, *2*, 366-373.

(21) Kriech, M. A.; Conboy, J. C. *J. Opt. Soc. Am. B* **2004**, *21*, 1013-1022.

(22) Kriech, M. A.; Conboy, J. C. *J. Am. Chem. Soc.* **2005**, *127*, 2834-2835.

(23) Shen, Y. R. *Appl. Phys. B: Lasers Opt.* **1999**, *68*, 295-300.

(24) Guyot-Sionnest, P.; Shen, Y. R. *Phys. Rev. B Condens. Matter* **1987**, *35*, 4420-4426.

(25) Roth, S. H. *Annu. Rev. Pharmacol. Toxicol.* **1979**, *19*, 159-178.

(26) Lee, A. G. *Nature* **1976**, *262*, 545-548.

(27) Seeman, P. *Pharmacol. Rev.* **1972**, *24*, 583-655.

(28) Ueda, I.; Kamaya, H. *Anesth. Analg. (N. Y.)* **1984**, *63*, 929-945.

(29) Auger, M.; Jarrell, H. C.; Smith, I. C.; Siminovitch, D. J.; Mantsch, H. H.; Wong, P. T. *Biochemistry* **1988**, *27*, 6086-6093.

(30) Boettner, M.; Winter, R. *Biophys. J.* **1993**, *65*, 2041-2046.

(31) Hutterer, R.; Kramer, K.; Schneider, F. W.; Hof, M. *Chem. Phys. Lipids* **1997**, *90*, 11-23.

(32) Yeagle, P. L.; Hutton, W. C.; Martin, R. B. *Biochim. Biophys. Acta, Biomembr.* **1977**, *465*, 173-178.

(33) Kitagawa, N.; Oda, M.; Totoki, T. *Anesthesiology* **2004**, *100*, 962-967.

(34) Marsh, D. *Handbook of Lipid Bilayers*; CRC Press, 1990.

(35) Hata, T.; Sakamoto, T.; Matsuki, H.; Kaneshina, S. *Colloids Surf., B* **2001**, *22*, 77-84.

(36) Gennis, R. B. *Biomembranes: Molecular Structure and Function* Spinger-Verlag New York, 1989.

(37) Barghouthi, S. A.; Puri, R. K.; Eftink, M. R. *Biophys. Chem.* **1993**, *46*, 1-11.

(38) Wright, S. E.; White, J. C.; Huang, L. *Biochim. Biophys. Acta, Biomembr.* **1990**, *1021*, 105-113.

(39) Liu, X. Y.; Yang, Q.; Kamo, N.; Miyake, J. *J. Chromatogr., A* **2001**, *913*, 123-131.

(40) Sarmento, A. B.; Pedroso de Lima, M. C.; Oliveira, C. R. *J. Pharm. Pharmacol.* **1993**, *45*, 601-605.

(41) Dill, K. A.; Stigter, D. *Biochemistry* **1988**, *27*, 3446-3453.

(42) Nguyen, T. T.; Rembert, K.; Conboy, J. C. *J. Am. Chem. Soc.* **2009**, *131*, 1401-1403.

(43) Nguyen, T. T.; Rembert, K.; Conboy, J. C. *J. Am. Chem. Soc.* **2011**, *133*, 6096-6097.

(44) Wisniewska, A.; Wolnicka-Glubisz, A. *Biophys. Chem.* **2004**, *111*, 43-52.

(45) Polozov, I. V.; Gawrisch, K. *Biophys. J.* **2006**, *90*, 2051-2061.

(46) Davis, J. H.; Clair, J. J.; Juhasz, J. *Biophys. J.* **2009**, *96*, 521-539.

(47) Ipsen, J. H.; Karlstroem, G.; Mouritsen, O. G.; Wennerstroem, H.; Zuckermann, M. J. *Biochim. Biophys. Acta, Biomembr.* **1987**, *905*, 162-172.

(48) Vist, M. R.; Davis, J. H. *Biochemistry* **1990**, *29*, 451-464.

(49) Sankaram, M. B.; Thompson, T. E. *Proc. Natl. Acad. Sci. U. S. A.* **1991**, *88*, 8686-8690.

(50) Almeida, P. F. F.; Vaz, W. L. C.; Thompson, T. E. *Biochemistry* **1992**, *31*, 6739-6747.

(51) Huang, T. H.; Lee, C. W. B.; Das Gupta, S. K.; Blume, A.; Griffin, R. G. *Biochemistry* **1993**, *32*, 13277-13287.

(52) Marsh, D. *Biochim. Biophys. Acta, Biomembr.* **2010**, *1798*, 688-699.

(53) McConnell, H. M.; Radhakrishnan, A. *Biochim. Biophys. Acta, Biomembr.* **2003**, *1610*, 159-173.

(54) Veatch, S. L.; Keller, S. L. *Biophys. J.* **2003**, *85*, 3074-3083.

(55) Krivanek, R.; Okoro, L.; Winter, R. *Biophys. J.* **2008**, *94*, 3538-3548.

(56) Almeida, P. F. *Biophys. J.* **2011**, *100*, 420-429.

(57) Kim, K.; Kim, C.; Byun, Y. *Langmuir* **2001**, *17*, 5066-5070.

(58) Sabatini, K.; Mattila, J.-P.; Kinnunen, P. K. J. *Biophys. J.* **2008**, *95*, 2340-2355.

(59) Dynarowicz-Latka, P.; Hac-Wydro, K. *Colloids Surf., B* **2004**, *37*, 21-25.

(60) de Meyer, F.; Smit, B. *Proc. Natl. Acad. Sci. U. S. A.* **2009**, *106*, 3654-3658.

(61) Radhakrishnan, A.; McConnell, H. M. *J. Phys. Chem. B* **2002**, *106*, 4755-4762.

(62) Worcester, D. L.; Franks, N. P. *J. Mol. Biol.* **1976**, *100*, 359-378.

(63) Radhakrishnan, A.; McConnell, H. M. *Biophys. J.* **1999**, *77*, 1507-1517.

(64) Pan, J.; Mills, T. T.; Tristram-Nagle, S.; Nagle, J. F. *Phys. Rev. Lett.* **2008**, *100*, 198103/198101-198103/198104.

(65) Rog, T.; Pasenkiewicz-Gierula, M.; Vattulainen, I.; Karttunen, M. *Biophys. J.* **2007**, *92*, 3346-3357.

(66) Pasenkiewicz-Gierula, M.; Subczynski, W. K.; Kusumi, A. *Biochemistry* **1990**, *29*, 4059-4069.

(67) Kusumi, A.; Subczynski, W. K.; Pasenkiewicz-Gierula, M.; Hyde, J. S.; Merkle, H. *Biochim. Biophys. Acta, Biomembr.* **1986**, *854*, 307-317.

(68) Martinez-Seara, H.; Rog, T.; Pasenkiewicz-Gierula, M.; Vattulainen, I.; Karttunen, M.; Reigada, R. *Biophys. J.* **2008**, *95*, 3295-3305.

(69) Martinez-Seara, H.; Rog, T.; Karttunen, M.; Vattulainen, I.; Reigada, R. *J. Phys. Chem. B* **2009**, *113*, 8347-8356.

(70) Seelig, J.; Ganz, P. *Biochemistry* **1991**, *30*, 9354-9359.

(71) Ikonen, M.; Murtomaeki, L.; Kontturi, K. *Colloids Surf., B* **2010**, *78*, 275-282.

(72) Gragson, D. E.; Richmond, G. L. *J. Am. Chem. Soc.* **1998**, *120*, 366-375.

(73) Wenk, M. R.; Fahr, A.; Reszka, R.; Seeligx, J. *J. Pharm. Sci.* **1996**, *85*, 228-231.

(74) Matos, C.; Lima, J. L. C.; Reis, S.; Lopes, A.; Bastos, M. *Biophys. J.* **2004**, *86*, 946-954.

(75) Baeuerle, H. D.; Seelig, J. *Biochemistry* **1991**, *30*, 7203-7211.

(76) Rowe, E. S.; Zhang, F.; Leung, T. W.; Parr, J. S.; Guy, P. T. *Biochemistry* **1998**, *37*, 2430-2440.

(77) Zhang, J.; Hadlock, T.; Gent, A.; Strichartz, G. R. *Biophysical Journal* **2007**, *92*, 3988-4001.

(78) Seydel, J. K. W., M. *Drug-Membrane Interactions*; Wiley-VCH Verlag GmbH: Weinheim, 2002.

(79) Eftink, M. R.; Puri, R. K.; Ghahramani, M. D. *Biochim. Biophys. Acta, Biomembr.* **1985**, *813*, 137-140.

(80) Kaminoh, Y.; Kamaya, H.; Ueda, I. *Biochim. Biophys. Acta, Biomembr.* **1989**, *987*, 63-68.

CHAPTER 7

CONCLUSIONS

The applications of nonlinear optical spectroscopies, second harmonic generation (SHG) and ultraviolet-visible sum frequency generation (UV-Vis SFG) in studying protein-ligand and drug-lipid membrane interactions were described in this dissertation. The use of SHG and UV-Vis SFG allowed for the direct detection of these biomolecular interactions without the need for chemical modification. The general principles of SHG were presented in Chapter 2 with an emphasis on the counter-propagating geometry which allows for a better separation of the SHG beam from the fundamental beams. In Chapter 3, the counter-propagating SHG technique was employed to study the binding properties of avidin, streptavidin, neutrAvidin^{TM} and anti-biotin antibody to a biotinylated lipid. Protein binding assays were performed on a planar supported lipid bilayer of 1,2-dioleoyl-*sn*-glycero-3-phosphocholine (DOPC) containing 4 mol % biotinylated-cap-1,2-dioleoyl-*sn*-glycero-3-phosphoethanolamine (biotin-cap-DOPE). The equilibrium binding affinities of these biotin-protein interactions were determined and correlated with the values reported in the literature validating the ability of SHG to be used an alternative technique to directly detect protein-ligand binding at the lipid membrane surfaces. The relative energetic contributions for each protein to the biotinylated lipid ligand were also revealed. The results show that the binding affinities of avidin, streptavidin and neutrAvidin^{TM} for biotin were all strengthened by protein-protein interactions but that stronger protein-protein interactions occur with

streptavidin making its binding the most energetically favorable. It was also shown that neutrAvidin^{TM} has the highest degree of nonspecific adsorption to a pure DOPC bilayer as compared to avidin and streptavidin. Additionally, the biotin-binding affinity of anti-biotin antibody was found to be of the same order of magnitude as avidin, streptavidin and neutrAvidin^{TM}. These findings provide important new insights into these biotin bound protein complexes, which are commonly used in several bioanalytical applications.

The background of SFG and the development of UV-Vis SFG were presented in Chapter 4. The deep UV wavelength of the UV-Vis SFG offers the ability to probe $\pi \rightarrow \pi^*$ and $n \rightarrow \pi^*$ electronic transitions in a variety of biological species such as aromatic amino acids, peptides, proteins and aromatic/double bond containing drugs. In Chapter 5, UV-Vis SFG spectroscopy was used to measure the association of drugs to lipid membranes. Four different classes of drugs, exemplified by a nonsteroidal anti-inflammatory (ibuprofen), an antibiotic (azithromycin), a local anesthetic (tetracaine), and an antifungal (tolnafate), were examined. Drug association was measured on planar supported lipid bilayers (PSLBs) composed of DOPC. The equilibrium association constants of the drugs were obtained with the following order: ibuprofen < tetracaine < azithromycin< tolnafate. Additionally, the surface excess of the drugs in the lipid membrane was quantitatively determined using the combination of the bulk partition coefficient and the SFG measurements. The calculated limit of detection of the UV-Vis SFG technique was at the pg/cm^2 level for these drugs and is comparable to that of fluorescence. Possessing great sensitivity and high surface specificity, UV-Vis SFG allowed for the direct detection of low molecular weight drug association into a lipid bilayer without any chemical modification and interference from solution phase species.

The study suggested that UV-Vis SFG is a powerful technique in measuring biomolecular interactions at surfaces.

The use of counter-propagating SHG to image the interactions between the local anesthetic tetracaine and a multicomponent planar supported lipid bilayer array in a label-free manner was presented in Chapter 6. The lipid bilayer arrays, prepared using a 3D continuous flow microspotter, allowed the effects of lipid phase and cholesterol content on tetracaine binding to be examined simultaneously. SHG images show that tetracaine has a higher binding affinity to liquid-crystalline phase lipids than to solid-gel phase lipids. The presence of 28 mol % cholesterol decreased the binding affinity of tetracaine to bilayers composed of the mixed chain lipid, 1-stearoyl-2-oleoyl-*sn*-glycero-3-phosphocholine (SOPC) and the saturated lipids 1,2-dimyristoyl-*sn*-glycero-3-phosphocholine (DMPC) and 1,2-dipalmitoyl-*sn*-glycero-3-phosphocholine (DPPC) while having no effect on DOPC. The maximum surface excess of tetracaine increases with the degree of unsaturation of the phospholipids and decreases with cholesterol in the lipid bilayers. The binding of tetracaine into DOPC and SOPC bilayers is an enthalpic process while entropy dominates tetracaine binding to SOPC with cholesterol as well as DMPC with and without cholesterol. The interactions between zwitterionic lipid bilayers and different charge states of tetracaine and between charged lipid bilayers with positively charged tetracaine were also presented in this chapter. It was found that the neutral form of tetracaine (pH 9.5) binds to the lipid bilayers with and without cholesterol to a greater extent than the charged form (pH 5.5). The presence of the positively charged lipid, 1,2-dioleoyl-3-trimethylammonium-propane (DOTAP), in DOPC bilayer reduces the binding of tetracaine (pH 7.4) whereas binding to DOPC is enhanced by the presence of the negatively charged lipid, 1,2-dioleoyl-*sn*-glycero-3-phospho-(1'-*rac*-glycerol)

(DOPG). In addition to revealing the properties of tetracaine binding, this study also establishes SHG imaging as a sensitive technique to directly image and quantitatively measure the association of a drug to a multicomponent lipid bilayer array in a high-throughput manner.

This dissertation has shown that the nonlinear optical spectroscopy techniques, SHG and UV-Vis SFG, can be used to directly detect biomolecular interactions at the lipid bilayer surfaces without any chemical modification. Unlike mass based label-free techniques, the resonant enhancement in SHG and UV-Vis SFG, which is achieved by tuning the SHG or UV-Vis SFG frequency to approach to electronic transitions of the analytes at the surface, can be employed as an extremely sensitive spectroscopic probe to detect the binding of proteins and drugs to the lipid bilayers. Furthermore, the use of SHG imaging in combination with the lipid bilayer array created by the continuous flow microspotter allows for a rapid and systematic study of drug-lipid membrane interactions, illustrating the application of the technique as a high-throughput method. This dissertation has demonstrated the utility of SHG and UV-Vis SFG spectroscopy/imaging as valuable alternatives in sensing biomolecular interactions at lipid membrane surfaces and offering potential contributions as medical and pharmacological screening tools.